

MONASH UNIVERSITY

PHYSICS MASTERS THESIS

---

**Dissipation of Magnetic Fields  
in Neutron Stars**

---

*Author:*

Ashley BRANSGROVE

*Supervisors:*

Prof Yuri LEVIN

Assoc Prof Daniel PRICE

2017





# MONASH University

School of Physics and Astronomy

A thesis submitted in partial fulfillment of the requirements for the degree of  
Master of Science (Physics)

Ashley Bransgrove



## Copyright Notice

© Ashley Bransgrove (2017)

I certify that I have made all reasonable efforts to secure copyright permissions for third-party content included in this thesis and have not knowingly added copyright content to my work without the owner's permission.

## Acknowledgements

First and foremost I acknowledge my supervisors Yuri Levin, and Daniel Price. Yuri has proved to be the archetypal mentor. I thank him for the many hours he spent sharing his knowledge of neutron stars, and guiding me through the trials of life as a graduate student. Daniel has been a constant support, as well as a model numericist. The wisdom he provided throughout my own numerical studies was invaluable, and will benefit me well into my future.

Andrei Beloborodov has been a most valuable scientific collaborator. His comments during writing are much appreciated, and helped to improve my scientific writing immensely. I also thank Chris Matzner and Xinyu Li for enlightening discussions. I thank Kostas Gourgouliatos and Andrew Cumming, for sharing data from their own numerical experiments, so that I could test my code.

I acknowledge financial support from the Australian Government in the form an Australian Postgraduate Award. I also thank the School of Physics and Astronomy at Monash University, and all therein for their support and assistance in various forms throughout my degree. I especially thank the Monash high-energy astrophysics group, and the Monash gravitational-wave group for making me welcome, and giving me a place to share my research. I also thank my fellow students for making this journey an enjoyable one.

Lastly I thank my parents, my sisters, and my partner for unwavering moral support, and putting up with my many absences during the course of this degree.

## Publications during enrolment

*Magnetic Field Evolution of Neutron Stars I: Basic formalism, numerical techniques, and first results*, Ashley Bransgrove, Yuri Levin, and Andrei Beloborodov, 2017, MNRAS (submitted for publication).

## Monash University Declaration

I hereby declare that this thesis contains no material which has been accepted for the award of any other degree or diploma at any university or equivalent institution and that, to the best of my knowledge and belief, this thesis contains no material previously published or written by another person, except where due reference is made in the text of the thesis.

This thesis includes no original papers published in peer reviewed journals and one submitted publication ([Bransgrove et al., 2017](#)), entitled:

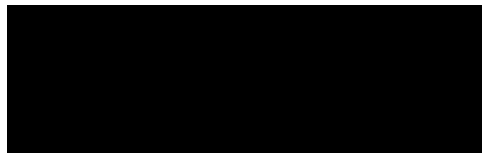
‘Magnetic Field Evolution of Neutron Stars I: Basic formalism, numerical techniques, and first results’

The core theme of the thesis is magnetic field evolution of neutron stars. The ideas, development and writing up of all the papers in the thesis were the principal responsibility of myself, the student, working within the School of Physics and Astronomy under the supervision of Yuri Levin and Daniel Price.

In the case of Chapter 2, Chapter 3, Chapter 4, Chapter 5, Chapter 6, Chapter 7, and Chapter 8 my contribution to the work involved the following:

Development of the models, development of the numerical methods, implementing the numerical method in the code, running the simulations, writing of the publication, and all other work therein (which is not referenced). I have renumbered sections of submitted or published papers in order to generate a consistent presentation within the thesis.

Candidate Signature:



Date:

June 29, 2017



## ABSTRACT

The behavior of neutron stars is governed by the dynamics of ultra-strong magnetic fields which thread their interiors. In this thesis we develop numerical techniques to model the evolution of axisymmetric magnetic fields in neutron stars.

Our code models the effects of Hall drift and Ohmic diffusion in the neutron star crust. We model the magnetically induced elastic deformation of the crust, and its feedback on the magnetic field evolution. For the first time, we correctly model the magnetic coupling between the solid crust and the liquid core on secular timescales. We find that axisymmetric core magnetic fields must satisfy an MHD equilibrium in the azimuthal direction. Implementing this equilibrium in our simulations, we find that the Hall Attractor of Gourgouliatos and Cumming also exists for core penetrating B-fields.

We model the drift of superconducting magnetic flux tubes in the core, using the prescription of Jones. We find that the combination of Jones flux tube drift in the core, and Ohmic diffusion in the crust, can deplete pulsar magnetic fields on a timescale of  $t \sim 150$  Myr if the crust is hot ( $T \sim 2 \times 10^8$  K), but acts on much slower timescales for cold neutron stars, such as recycled pulsars ( $\sim 1.8$  Gyr, depending on impurity levels).

We develop our own model for the macroscopic transport of flux tubes by superfluid neutron vortices. Our model includes the effects of vortex-flux tube pinning, the cut-through of superfluid vortices, the flux tube self-tension, and the sliding of flux tubes along superfluid neutron vortices.

Implementing our model of flux tube transport by superfluid vortices in our numerical code, we model the spin-down of new-born, rapidly rotating, highly magnetized neutron stars. Assuming an initial spin period of 1 ms, and that the core becomes superfluid and superconducting  $\sim 300$  years after birth (as suggested by the Cas A remnant) we find that the core magnetic field cannot be expelled when  $B \gtrsim 2 \times 10^{13}$  G. However, for  $B \lesssim 10^{13}$  G, the magnetic field is expelled into the the outer core and deep crust. This results in the growth of strong toroidal fields due to Hall drift, as well driving very strong currents in the deep crust, which are site to enhanced Ohmic dissipation.



# Contents

|          |   |           |
|----------|---|-----------|
| <b>1</b> | <b>Introduction</b>                                     | <b>1</b>  |
| <b>2</b> | <b>Neutron Stars</b>                                    | <b>9</b>  |
| 2.1      | Phenomenology . . . . .                                 | 10        |
| 2.2      | Crust . . . . .   | 12        |
| 2.3      | Core . . . . .  | 13        |
| 2.4      | Magnetic Field . . . . .                                | 15        |
| <b>3</b> | <b>Magnetic Field Evolution in Neutron Star Crusts</b>  | <b>21</b> |
| 3.1      | Hall Drift and Ohmic Diffusion . . . . .                | 22        |
| 3.2      | Characteristic Time Scales . . . . .                    | 23        |
| 3.3      | Axisymmetric Equations . . . . .                        | 24        |
| 3.4      | Hall Attractor . . . . .                                | 26        |
| 3.5      | Computational Methods . . . . .                         | 27        |
| 3.5.1    | Boundary Conditions . . . . .                           | 27        |
| 3.5.2    | Matching the Crust Field to the Magnetosphere . . . . . | 28        |
| 3.5.3    | Numerical Scheme . . . . .                              | 29        |
| 3.6      | Test Problems . . . . .                                 | 30        |
| <b>4</b> | <b>Magnetic Coupling of the Crust and the Core</b>      | <b>35</b> |
| 4.1      | Hydromagnetic Equilibrium . . . . .                     | 36        |
| 4.2      | Method I: Flux Coordinates . . . . .                    | 36        |
| 4.3      | Method II: Relaxation . . . . .                         | 37        |
| 4.4      | Numerical Details . . . . .                             | 40        |
| 4.5      | Test Problems . . . . .                                 | 41        |
| 4.6      | Results . . . . .                                       | 45        |
| <b>5</b> | <b>Flux Tube Drift in Type-II Superconducting Cores</b> | <b>49</b> |
| 5.1      | Jones Flux Tube Drift . . . . .                         | 50        |
| 5.1.1    | Superconducting Magnetic Stress Tensor . . . . .        | 50        |
| 5.1.2    | Forces on a Flux Tube . . . . .                         | 52        |

|          |   |            |
|----------|---|------------|
| 5.1.3    | Current Screening Condition . . . . .                       | 56         |
| 5.1.4    | Electric Field of a Moving Flux Tube . . . . .              | 59         |
| 5.1.5    | Large Scale Flux Tube Drift . . . . .                       | 61         |
| 5.2      | Axisymmetric Equations . . . . .                            | 62         |
| 5.3      | Numerical Details . . . . .                                 | 63         |
| 5.4      | Results . . . . .   | 64         |
| 5.4.1    | Flux tube drift and Hall drift (strong B) . . . . .         | 65         |
| 5.4.2    | Flux tube drift and no Hall drift (moderate B) . . . . .    | 68         |
| <b>6</b> | <b>Spin-down of Superfluid Cores</b>                        | <b>73</b>  |
| 6.1      | Rotating Neutron Superfluid . . . . .                       | 74         |
| 6.2      | Vortex - Flux Tube Interactions . . . . .                   | 75         |
| 6.3      | Flux Transport by Superfluid Neutron Vortices . . . . .     | 76         |
| 6.4      | Numerical Details . . . . .                                 | 79         |
| 6.5      | Results . . . . .   | 80         |
| <b>7</b> | <b>Magneto-Elastic Evolution of Neutron Star Crusts</b>     | <b>89</b>  |
| 7.1      | Magneto-Elastic Evolution . . . . .                         | 90         |
| 7.2      | A Relaxation Method for Magneto-Elastic Evolution . . . . . | 92         |
| 7.3      | Axisymmetric Equations . . . . .                            | 93         |
| 7.4      | Numerical Details . . . . .                                 | 93         |
| 7.5      | Results . . . . .   | 95         |
| <b>8</b> | <b>Discussion</b>   | <b>101</b> |
| <b>A</b> | <b>Twist Evolution of the Core.</b>                         | <b>107</b> |
| <b>B</b> | <b>The Code</b>   | <b>109</b> |

# List of Figures

|     |   |    |
|-----|---|----|
| 2.1 | $P - \dot{P}$ diagram of known neutron stars . . . . .  | 10 |
| 2.2 | Lattice structure of the crust as a function of density . . . . .   | 12 |
| 2.3 | Dipole field strength vs. characteristic age of known pulsars . . . . .   | 15 |
| 3.1 | Electron density and electrical conductivity as a function of $r$ . . . . .   | 23 |
| 3.2 | $\log_{10} L_2$ vs. $\log_{10} \delta r$ : Comparisson of our code with the analytic $n = 0$ $l = 1$ Ohmic eigenmode. . . . .             | 31 |
| 3.3 | $\log_{10} \epsilon_{\max}$ vs. $\log_{10} \delta r$ : Comparisson of our code with the analytic $n = 0$ $l = 1$ Ohmic eigenmode. . . . . | 32 |
| 3.4 | Comparisson of our code with the code of Gourgouliatos and Cumming . . . . .  | 33 |
| 4.1 | Hydromagnetic relaxation test 1 . . . . .   | 43 |
| 4.2 | $I$ vs. $\Psi$ for hydromagnetic relaxation test 1 . . . . .  | 43 |
| 4.3 | Hydromagnetic relaxation test 2 . . . . .   | 44 |
| 4.4 | $I$ vs. $\Psi$ for hydromagnetic relaxation test 2 . . . . .  | 44 |
| 4.5 | Magnetic field evolution (Model A) . . . . .  | 46 |
| 4.6 | Electron angular velocity evolution (Model A) . . . . .   | 47 |
| 5.1 | Cross section of a flux tube . . . . .  | 53 |
| 5.2 | Superconducting ring experiment . . . . .   | 59 |
| 5.3 | Magnetic field evolution (Model B) . . . . .  | 67 |
| 5.4 | 1D cartesian crust model . . . . .  | 68 |
| 5.5 | Magnetic field evolution (Model C) . . . . .  | 70 |
| 5.6 | Decay of dipole field (Model C) . . . . .   | 71 |
| 6.1 | Vortex - flux tube interaction . . . . .  | 75 |
| 6.2 | Ruderman's model of flux tube transport . . . . .   | 77 |
| 6.3 | Magnetic field evolution (Model D1) . . . . .   | 84 |
| 6.4 | Magnetic field evolution (Model D2) . . . . .   | 85 |
| 6.5 | Magnetic field evolution (Model D3) . . . . .   | 86 |

|     |  |    |
|-----|--|----|
| 7.1 | Magnetic field evolution (Model E) . . . . . | 98 |
| 7.2 | Crustal displacement (Model E) . . . . .     | 99 |

# Chapter 1

## Introduction

Neutron stars are site to the most extreme physics in the universe. The behavior of a neutron star at a given point in its life has a strong dependence on the dynamics of the magnetic field which threads its interior. With the wealth of observations over the last five decades of pulsar astronomy, it is possible to pose questions about the behavior of neutron stars over the course of their lives, by studying properties of the galactic population. Theoretical studies, combined with observations may provide insight to the magnetic evolution of neutron stars.

In 1931, Landau theorized the existence of dense stars which looked like a giant nucleus, a year before the discovery of the neutron in February of 1932 (Yakovlev et al., 2013). This conceptual prediction was published in his 1932 paper [see Landau (1965)]. The existence of neutron stars was first predicted explicitly by Baade & Zwicky (1934) at Caltech, who speculated that a core collapse supernova could result in a small dense neutron dominated remnant. The first radio pulsar (PSR B1919+21) was discovered in 1967 by Hewish et al. (1968), who detected periodic radio pulses 1.337 seconds apart with the newly constructed Mullard Radio Observatory at Cambridge, UK. In the following year the crab pulsar (PSR B0531+21) was discovered, at the precise location of a supernova witnessed by Chinese astronomers in 1054 A.D (Staelin & Reifenstein, 1968). This provided a firm link between pulsars and supernova remnants (Comella et al., 1969). In the same year Pacini (1968) and Gold (1968) asserted that pulsars were rapidly rotating, magnetized neutron stars. The rotation of pulsars can drive winds, which power electromagnetic emission in surrounding nebulae.

The first millisecond pulsar (a pulsar with spin period  $\lesssim 10$  ms) was discovered in 1982 by Backer et al. (1982). The existence of such fast spinning neutron stars with stable spin frequencies raised interesting questions about their origin. Millisecond pulsars are by far the oldest neutron stars in the galaxy, and possess the weakest magnetic fields. The field strength of

pulsars with spin periods  $\leq 10$  ms ranges from  $4.5 \times 10^7$  G to  $4.34 \times 10^9$  G (Manchester et al., 2005). It is commonly thought that some fraction of the millisecond pulsars had stronger magnetic fields, and longer spin periods earlier in their lives.

The work of Duncan & Thompson (1992) proposed a new class of neutron stars, which are powered by the dissipation of energy stored in ultra-strong magnetic fields ( $B_{\text{dipole}} \sim 10^{14} - 10^{15}$  G), as opposed to pulsars which are powered by rotational energy. Soft gamma repeaters (SGRs) typically emit in hard X-ray and soft gamma-ray bands in repeating bursts, first seen by Mazets et al. (1979a). The first giant flare of an SGR was detected by Mazets et al. (1979b), in hard X-rays. The 8 second pulsations in the decaying flux tail were indicative of the rotation of a neutron star, though with much longer spin period than previously known pulsars. The first measurement of the spin-down rate of an SGR was that of SGR 1806-20 by Kouveliotou et al. (1998), which inferred a dipole magnetic field strength of  $8 \times 10^{14}$  G, and a characteristic age of  $\sim 1500$  years. This was strong evidence that SGRs are in fact magnetars.

The first anomalous X-ray pulsar (AXP) was detected by Fahlman & Gregory (1981), who claimed to have discovered an isolated X-ray pulsar in the supernova remnant SNR G109.11.0, with spin period 3.5 s. Subsequently, more AXPs were discovered, which displayed X-ray bursting activity, with energetics which could not be explained by the accretion of a binary companion. The long spin periods of these objects was at odds with other isolated pulsars, and pulsars in low-mass X-ray binaries (LMXBs). An important suggestion was made by Thompson & Duncan (1996), who stated that if AXPs were magnetars, one would expect SGR like emission from them. This was confirmed with the detection of X-ray bursts from AXPs 1E 1048-5937 and 1E 2259+586 [Gavriil et al. (2002), Kaspi et al. (2003)], which until that time had only been observed from SGRs. It is now commonly accepted that both SGRs and AXPs are magnetars.

X-ray observations of magnetars show a range of interesting phenomena, which are currently not well-understood. It is generally accepted that magnetar emission is generated by the dissipation of free energy stored in these ultra-strong magnetic fields. Recently a number of neutron stars have been discovered which display transient periods of X-ray activity, normally associated with magnetars, though these stars have significantly weaker dipole fields [e.g. Tiengo et al. (2013), Rodríguez Castillo et al. (2016), Borghese et al. (2017)]. The field strength of these highly magnetized pulsars, as inferred from their spin-down rate is not sufficient to power magnetar emission in conventional models.

Modern neutron star models suggest a radius of  $\sim 11$  km, and a typical mass of  $\sim 1.4 M_{\odot}$  (Ozel & Freire, 2016). The outer 1 km is thought to be a solid crystalline crust, which surrounds a liquid core. In neutron star cores, it has long been theorized that neutrons form a superfluid [Migdal (1959) - before the discovery of the first pulsar!], while the protons condense to form a superconductor (Baym et al., 1969). In this interesting scenario there are two interacting, macroscopic quantum fluids. The magnetic field is quantized into a discrete array of microscopic ‘flux tubes’, and rotation of the star itself manifests itself as an array of vortices in the neutron superfluid.

The magnetic field which threads the interior of neutron stars can evolve through different mechanisms in different regions of the star. In the neutron star crust, the magnetic field can evolve through Hall drift and Ohmic diffusion [Jones (1987), Goldreich & Reisenegger (1992)]. In addition to this the crust deforms in response to magnetic stresses, and the motion of the crust induces a back-reaction on the evolution of the field [Cumming et al. (2004), Li et al. (2016a)]. Evolution of magnetic fields in the core is less well-understood. This lack of understanding is primarily due to uncertainties in the physics of condensed matter at densities exceeding nuclear density.

The thesis explores problems relating to the evolution of neutron star magnetic fields. Specifically, we will explore the following problems:

- All numerical studies of magnetic field evolution in neutron stars so far have failed to correctly model the magnetic coupling between the crust and the core [e.g. Hollerbach & Rüdiger (2002), Pons & Geppert (2007), Marchant et al. (2014), Gourgouliatos & Cumming (2014), Suvorov et al. (2016), Elfritz et al. (2016)]. This is because the liquid core cannot support solenoidal Lorentz forces, and adjusts to any such force on dynamical timescales (the Alfvén crossing time is of order  $t_A \sim 1$  s for  $B \sim 10^{14}$  G). In addition to this there are processes which allow the core magnetic field to evolve on secular timescales both in the crust and the core. Thus, it is a challenge to model the fast response of the liquid core to shear stresses, as well as long timescale magnetic field evolution.
- Highly magnetized pulsars (the so-called “low-B” magnetars and “high-B” pulsars) display transient episodes of magnetar-like X-ray emission (Rea et al., 2010). However, the dipole magnetic field of these objects is significantly weaker than that of classical magnetars. Importantly, these objects are possibly much older than the classical magnetar age of 10 kyr. Rather, they are mostly Myr’s old [see (Kaspi & Beloborodov, 2017) for a review]. There is little theoretical understanding of the origin and emission of these neutron stars.

- Millisecond pulsars have the weakest magnetic fields in the pulsar population (Kaspi & Kramer, 2016). It is thought that many millisecond pulsars were born with magnetic fields similar to young pulsars, which have typical strength  $10^{11} - 10^{12}$  G (Kaspi & Kramer, 2016). One possibility is that the magnetic field is buried by accretion from a binary companion [e.g. Romani (1990), Cumming et al. (2001), Choudhuri & Konar (2002), Payne & Melatos (2004)]. However the existence of isolated millisecond pulsars is problematic. Another possibility is that the magnetic field can decay on long timescales due to dissipative processes in the neutron star [e.g. Goldreich & Reisenegger (1992), Jones (2006), Ruderman et al. (1998)]. The field decay of isolated neutron stars has been controversial. Bhattacharya et al. (1992) conducted statistical studies and argued that pulsar magnetic fields do not decay. Conversely, Mukherjee & Kembhavi (1997) stated that the magnetic fields of isolated pulsars could decay with a minimum timescale of  $\sim 160$  Myr. Similarly, more recent studies of the pulsar population have failed reach reach any strong consensus [e.g. Faucher-Giguere & Kaspi (2006), Popov et al. (2010), Gullón et al. (2014), Gullón et al. (2015)]. It is possible that theoretical input, combined with observations could uncover the origin of millisecond pulsars, and the evolution of their magnetic fields.
- The coupled dynamics of the solid crust and the magnetic field in highly magnetized neutron stars has been explored using numerical arguments Cumming et al. (2004), and detailed numerical experiments Li et al. (2016a), Thompson et al. (2017). However, 2D axisymmetric models of magnetic field evolution in neutron star crusts so far have not included the deformation of the solid crust on the magnetic field evolution [e.g. Hollerbach & Rüdiger (2002), Pons & Geppert (2007), Marchant et al. (2014), Gourgouliatos & Cumming (2014), Suvorov et al. (2016), Elfritz et al. (2016)].

Developments in numerical techniques have made it possible to study the global magnetic field evolution of neutron stars due to a variety of proposed mechanisms. In this thesis we address the issue of modeling the magnetically coupled crust and core. We find that the liquid core satisfies a hydromagnetic equilibrium in the azimuthal direction. Implementing this in our numerical experiments allows us to self-consistently study the coupled crust-core evolution of neutron star magnetic fields on secular timescales, while ensuring the stability of the field configuration, and taking into account the magnetic twist exchange between the crust and the core. Previous studies have neglected the injection and extraction of magnetic twist into/out of the core [Suvorov et al. (2016), Elfritz et al. (2016)].

Implementing the hydromagnetic equilibrium in our simulations, we model the drift of superconducting magnetic flux tubes in the neutron star core, coupled to a crust evolving through

Hall drift and Ohmic diffusion. We explore the long timescale evolution of pulsar strength magnetic fields with the combination of flux tube drift in the core, and Ohmic diffusion in the crust. Using this 2D model we calculate the decay timescale for the dipole magnetic field, and compare with the galactic population of pulsars. We also develop a method for studying the coupled magneto-elastic evolution in the crust of highly magnetized neutron stars in axisymmetry.

An outline of this thesis is as follows. In Chapter 1 we introduce neutron star phenomenology, and more theoretical background on the crust, the core, and evolution of magnetic fields in neutron stars. In Chapter 3 we discuss magnetic field evolution in neutron star crusts. We describe our formalism for representing axisymmetric magnetic fields, and outline our numerical scheme for evolving magnetic fields through Hall drift and Ohmic diffusion.

In Chapter 4 we formulate the hydromagnetic equilibrium in the core using two different approaches. We then show the results of implementing this equilibrium in our numerical code. In Chapter 5 we outline the drift of superconducting flux tubes according to the treatment of [Jones \(2006\)](#). Here we also point out some of the controversies in the literature surrounding this topic, though we do not resolve these issues – this is left for future work. We also cover some other aspects of building a theory of magnetic field evolution in superconducting neutron stars. Specifically, we discuss the balance of forces acting on a flux tube, the charge current screening condition, and the magnetic field evolution equation. We then model the Jones drift of flux tubes in the core for the case of strong B (Hall + Ohmic diffusion in the crust), and for the case of moderate B (Ohmic diffusion only in the crust).

In Chapter 6 we outline our model of flux transport by superfluid vortices. We then present simulations for the spin-down of a new-born, rapidly rotating, highly magnetized pulsar for several different field strengths, and initial spin periods. In Chapter 7 we outline our method for including the elastic displacement of the crust in axisymmetry, and the feedback of this on the magnetic field evolution. We present a simulation showing the elastic deformation of the crust, and the magnetic field evolution when a burst of Hall waves is launched from the crust-core interface in a highly magnetized neutron star. In Chapter 8 we discuss our results, and some preliminary implications of these in relation to the galactic population of neutron stars. Below we provide a table which summarizes our Models of magnetic field evolution, for ease of navigation in this thesis.

Table 1.1: Summary of the models we present in this thesis. Here HME (relaxation) implies hydromagnetic equilibrium enforced by the relaxation method in Section 4. HME (trivial) is for symmetric configurations where the toroidal field remains zero in the core according to hydromagnetic equilibrium.

| Model | Crust Evolution        | Core Poloidal Evolution | Core Toroidal Evolution | $ \mathbf{B} _{\max}$ (initial) | Section   |
|-------|------------------------|-------------------------|-------------------------|---------------------------------|-----------|
| A     | Hall + Ohmic           | Fixed                   | HME (Relaxation)        | $2.2 \times 10^{14}$ G          | Chapter 4 |
| B     | Hall + Ohmic           | Jones drift only        | HME (Trivial)           | $2.2 \times 10^{14}$ G          | Chapter 5 |
| C     | Ohmic                  | Jones drift only        | HME (Trivial)           | $2 \times 10^{12}$ G            | Chapter 5 |
| D1    | Hall + Ohmic           | Spin-down only          | HME (Trivial)           | $6.9 \times 10^{12}$ G          | Chapter 6 |
| D2    | Hall + Ohmic           | Spin-down only          | HME (Trivial)           | $1.4 \times 10^{13}$ G          | Chapter 6 |
| D3    | Hall + Ohmic           | Spin-down only          | HME (Trivial)           | $2.7 \times 10^{13}$ G          | Chapter 6 |
| E     | Hall + Ohmic + Elastic | Fixed                   | HME (Trivial)           | $2 \times 10^{14}$ G            | Chapter 7 |

# Monash University Declaration Chapter 2

## Declaration by candidate:

I declare that my contribution to the work in Chapter 2 that is submitted to the Monthly Notices of the Royal Astronomical Society as [Bransgrove et al. \(2017\)](#), involved the following:

The writing of the publication, and all other work contained therein (that is not referenced otherwise).

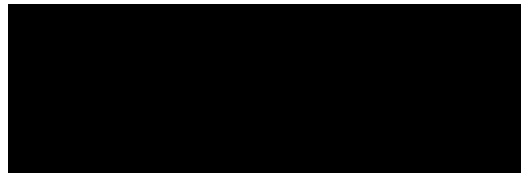
Extent of contribution by candidate: 85%

Co-author names: Yuri Levin, Andrei Beloborodov

Nature of co-author's contribution: Feedback during writing of the paper.

I have renumbered sections, equations and figures of the published paper in order to generate a consistent presentation within the thesis. The undersigned hereby certify that the above declaration correctly reflects the nature and extent of the student's and co-authors' contributions to this work.

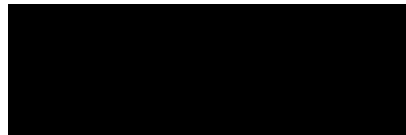
Candidate Signature:



Date:

June 29, 2017

Main Supervisor signature:



Date:

June 29, 2017



# Chapter 2

## Neutron Stars

Partially adapted from:

*Magnetic Field Evolution of Neutron Stars I: Basic formalism, numerical techniques, and first results*, Ashley Bransgrove, Yuri Levin, and Andrei Beloborodov, 2017, submitted for publication in MNRAS.

## 2.1 Phenomenology

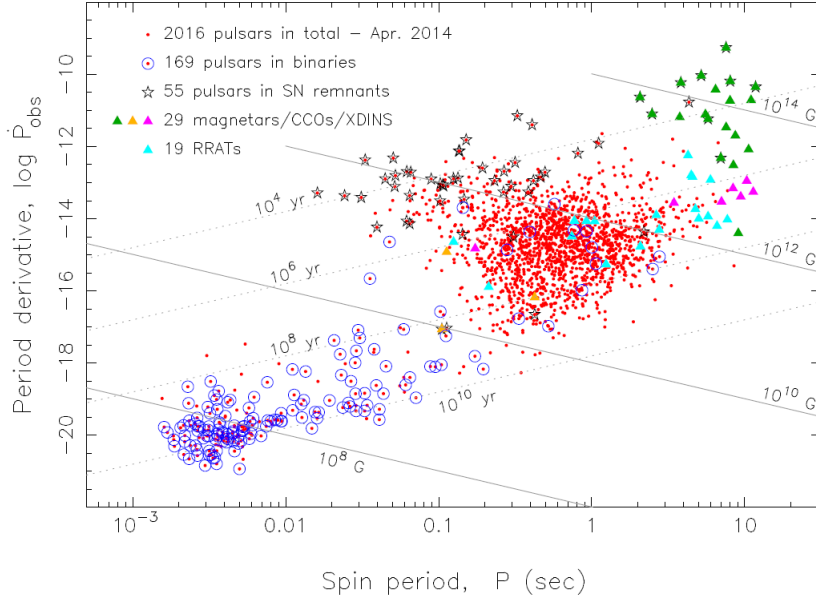


Figure 2.1:  $P - \dot{P}$  diagram. Red dots represent known radio pulsars as of April 2014, blue circles represent binaries, red dots represent pulsars, and stars represent supernova remnants. Magnetars are represented by green triangles. Solid grey lines are of constant magnetic field strength, and dotted grey lines are of constant characteristic age (Tauris et al., 2014).

There is a rich variety of neutron stars with magnetic field strengths which differ by several orders of magnitude, and vastly different behaviors. The evolution of neutron star magnetic fields can provide insight into the origin, behavior, and populations of neutron stars [eg. Tauris et al. (2014)].

Pulsars are rapidly rotating, magnetized neutron stars, and are characterized by intense beams of radio-waves, emitted by the plasma on the open magnetic field lines connecting the star to its light cylinder. Young pulsars have spin periods of tens of milliseconds to seconds. The spin-down inferred field strength of pulsars younger than 100 Myr ranges from  $1.57 \times 10^9 - 9.4 \times 10^{13}$  G (Manchester et al., 2005), with the mode field strength  $B \approx 10^{12}$  G (Kaspi & Kramer, 2016). Millisecond pulsars, an extreme subclass of radio pulsars exhibit spin periods ranging from 1.4 ms to  $\sim 10$  ms, and far weaker magnetic fields ranging from  $10^8 - 10^{10}$  G. The current fastest spinning millisecond pulsar has spin frequency of 716 Hz (Hessels et al., 2006). Approximately 60% of the 294 observed pulsars with spin periods less than 10 ms (Manchester et al., 2005) exist in binary systems. This leads to the conclusion that much of the millisecond pulsar population may have been born regular pulsars, which spin-down below the radio death-line

by magnetic braking, and then spin-up by the accretion of a companion star. These are the so-called recycled pulsars. The depletion of the pulsar magnetic field during this process is not well understood. One proposed mechanism is the burial of the surface field by the accretion flow [see eg. Romani (1990), Cumming et al. (2001), Choudhuri & Konar (2002), Payne & Melatos (2004)]. Another is expulsion of flux from the core, [Ruderman et al. (1998) Jones (2006)]. It is possible that the origin, birth rate, and spin history of millisecond pulsars can be better understood by studying the evolution of pulsar magnetic fields.

The most extreme class of neutron stars are magnetars. Canonical magnetars are radio-quiet persistent X-ray sources, powered by dissipation of free energy stored in ultra-strong magnetic fields ( $10^{14} - 10^{15}$  G) [Duncan & Thompson (1992), Kaspi & Beloborodov (2017)]. These young neutron stars have typical spin-down inferred ages of  $\tau_c \lesssim 10$  kyr. But the discovery of a wide variety of magnetars over the years has led to a broader class of objects, with a range of ages and field strengths. Particularly interesting are the so-called transient magnetars, which exhibit extended periods of low luminosity, followed by outbursts, during which the X-ray flux can increase by three orders of magnitude, before returning to quiescence over periods of months to years (Turolla et al., 2015). The mechanism which causes these bursts of activity is not well understood, but is believed to be due to the evolution of super-critical magnetic fields which shear the crust, and generate magnetospheric activity [Perna & Pons (2011), Beloborodov & Levin (2014), Li et al. (2016a), Thompson et al. (2017)]. Many transient magnetars are young, seemingly displaying these bursts of activity in the thousands of years following their birth [see eg. Ibrahim et al. (2004)]. The discovery of SGR 0418+5729 in 2009 with spin-down inferred age greater than 24 Myr and dipole field strength  $B = 7.5 \times 10^{12}$  G was the beginning of a new class of transients, possibly older than the commonly accepted magnetar lifetime of 10 kyr (Rea et al., 2010). The so-called “weak-field” magnetars challenge some aspects of the classical magnetar model, which posits that magnetar activity is generated by energy stored in an ultra-strong magnetic field.

The fact that there are several well defined classes of neutron stars, with a number of transient objects displaying behavior somewhere between these classifications, suggests that the galactic population of neutron stars may be explained by differing ages and birth field strengths. The discovery of radio emission from magnetars (Camilo et al., 2006), and magnetar emission from so-called “high-B pulsars” (Archibald et al., 2016) adds evidence to this argument. While observations point to a unification of neutron star classes (Kaspi & Kramer, 2016), further theoretical work is required to complete this picture. Recent discussion of a unification was based on the models of magnetic field and thermal evolution (Viganò et al., 2013). It is likely

that any such unification would see a given neutron star traverse a variety of classes over the course of its life, with its classification at any time having a strong dependence on magnetic field strength, and configuration. Indeed studying the evolution of neutron star magnetic fields is key to understanding how a neutron star may transition from one class of object to another.

## 2.2 Crust

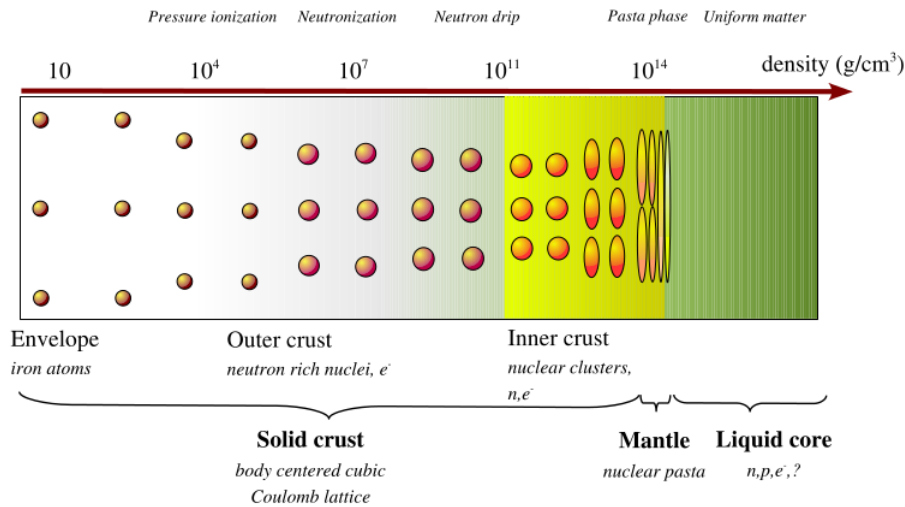


Figure 2.2: Diagram of lattice structure as a function of density. Image: (Chamel & Haensel, 2008).

The crust of a neutron star is primarily an ionic lattice of ionized nuclei, immersed in a sea of degenerate electrons. Above the solid crust is an ocean, formed by a heavy ion plasma. The density at the crust-ocean interface is fixed by the value of the Coulomb parameter [ $\Gamma = 175$  (Potekhin & Chabrier, 2000)]. This gives the density at the crust-ocean interface  $\rho_{\text{surface}} \approx 8 \times 10^7 \text{ g cm}^{-3}$  at  $10^8 \text{ K}$  (Cumming et al., 2004). Nuclei possess an increasing number of neutrons with depth, due to electron captures (Chamel & Haensel, 2008). The so-called ‘neutron drip’ begins at  $\rho \approx 4 \times 10^{11} \text{ g cm}^{-3}$ . This is the location in the crust where the nuclei become too bloated to contain their neutrons, and it becomes energetically favorable for neutrons to ‘drip’ out of their corresponding nucleus. Thus, beyond this density the ionic lattice is immersed in neutrons, as well as degenerate electrons. In the upper crust the pressure is dominated by degenerate electrons, while in the lower crust, the pressure is dominated by degenerate neutrons. In the deep crust the density approaches nuclear density  $\rho \approx 10^{14} \text{ g cm}^{-3}$ . Around this density it becomes energetically favorable for nuclei to acquire various exotic morphologies, corresponding to the so-called pasta phases (Chamel & Haensel, 2008). The base of the crust (or the crust-core

interface) corresponds to the depth beyond which nuclear density is exceeded, and the solid lattices becomes a nuclear liquid (Chamel & Haensel, 2008).

In our studies of magnetic field evolution, we will be particularly interested in the variation of the electron density and electrical conductivity throughout the crust, since this determines the evolutionary time scale. The rate at which magnetic fields are diffused in the neutron star crust is determined by the electrical conductivity,  $\sigma$ . The crust has some finite electrical conductivity due to electron-phonon and electron-impurity scattering. The conductivity due to phonon scattering is given as

$$\sigma_{\text{phonon}} = 1.8 \times 10^{25} (\rho_{14}^{7/6} / T_8^2) (Y_e / 0.05)^{5/3} \text{ s}^{-1}, \quad (2.1)$$

with  $\rho_{14}$  the mass density in units of  $10^{14} \text{ g cm}^{-3}$ , and  $T_8$  the temperature in units of  $10^8 \text{ K}$  [Baiko & Yakovlev (1995), Baiko & Yakovlev (1996), Cumming et al. (2004)]. Phonon scattering is exponentially suppressed when  $T < T_U = 8.7 \times 10^7 \text{ K}$   $\rho_{14} (Y_e / 0.05) (Z/30)^{1/3}$  [Gnedin et al. (2001), (Cumming et al., 2004)], and the Umklapp processes freeze out. Impurity scattering is dominant at low temperatures ( $T < T_U$ ), or high impurity levels. Estimates of the impurity levels in the deep crust range from  $Q_{\text{imp}} \approx 10^{-3}$  (Flowers & Ruderman, 1977), to  $Q_{\text{imp}} \approx 10$  (Jones, 2001). When  $T < T_U$ , and impurity scattering is dominant, the electrical conductivity in the deep crust is

$$\sigma_Q = 4.4 \times 10^{25} \text{ s}^{-1} (\rho_{14}^{1/3} / Q_{\text{imp}}) (Y_e / 0.05)^{1/3} (Z/30) \text{ s}^{-1}, \quad (2.2)$$

[Itoh & Kohyama (1993), Cumming et al. (2004)]. The ionic lattice can support elastic stresses up to some critical stress, beyond which the crust deforms in the plastic regime. We will model the deformation of the crust due to magnetic stresses, in the elastic regime.

## 2.3 Core

Neutron star cores are a dense liquid comprised of neutrons, and a proton electron plasma. The degeneracy pressure of neutrons, and nuclear forces between baryons supports the core against the force of gravity. Goldreich & Reisenegger (1992) emphasized that the composition of matter in neutron star cores is stably stratified. Specifically, the ratio of charged particle number density to neutron number density increases with depth. In the absence of external forces, the stratification satisfies chemical equilibrium, mediated by diffusion of neutrons, and weak interactions which drive the ratio of charged particles to neutrons to the equilibrium value at a given depth.

Magnetic fields in the core can evolve due to a number of mechanisms on timescales which vary by many orders of magnitude. Dynamical evolution of the magnetic field occurs through ideal magnetohydrodynamics (ideal MHD). The Alfvén crossing time in neutron star cores is of order  $t_A \sim 1$  s for  $B \sim 10^{14}$  G. Additionally there are secular processes which occur over much longer timescales, which we discuss below.

In normal (non-superconducting) neutron star cores, the magnetic field is coupled to the charged particle plasma, which can be forced through the background neutrons by Lorentz forces. The transport of the magnetic field with this flow of charged particles is known as Ambipolar diffusion. [Goldreich & Reisenegger \(1992\)](#) show that compressive Lorentz forces perturb the chemical equilibrium, and lead to the development of chemical potential gradients. These pressure gradients choke the flow of charged particles, and inhibit the drift of the magnetic field due to Ambipolar diffusion. As pointed out by [Beloborodov & Li \(2016\)](#), if the core is hot  $T \gtrsim 10^9$  K, and the magnetic field is very strong  $B \sim 10^{16}$  G, the weak interactions proceed so quickly that the core matter is never far from chemical equilibrium. In this regime the ambipolar drift of charged particles is only limited by the frictional drag on the background neutrons, and the magnetic field may be rearranged very quickly.

The core magnetic field likely has a strong toroidal component, since purely poloidal configurations are susceptible to the Flowers-Ruderman instability, in the first  $\sim 100$  s after birth, before the crust freezes in [[Flowers & Ruderman \(1977\)](#), [Braithwaite & Spruit \(2006\)](#)]. An interesting consequence of stable stratification in neutron star cores is that hydromagnetic instabilities are forced to occur at the ambipolar drift velocity, rather than on the Alfvén crossing time, as pointed out by [Thompson et al. \(2017\)](#). This is because the magnetic field is coupled to the charged fluid, which can only proceed at the rate set by weak nuclear interactions and friction between the charged plasma and the background neutrons. Additionally field lines which are anchored in the solid crust may be stabilized.

Conventional theory indicates that the neutrons in the cores form a  ${}^3P_2$  superfluid below the critical temperature  $T \sim \text{few} \times 10^8$  K depending on the model ([Potekhin et al., 2015](#)). The protons are believed to condense and form a  ${}^1S_0$  superconductor when  $T \lesssim \text{few} \times 10^9$  K depending on the model ([Potekhin et al., 2015](#)). In this scenario the magnetic field is quantized into a discrete array of microscopic magnetic flux tubes, each of which possess the quantum of flux  $\phi_0 = hc/2e$ . Rotation of the neutron superfluid manifests itself in an array of microscopic superfluid vortices, each of which possess the quantum of circulation  $\kappa = h/2m_n$ . Since neutron stars are born very hot, and cool as they age, the phase transition to proton superconductivity

will likely occur before the phase transition to neutron superfluidity.

The most significant evidence for superfluidity in neutron star cores comes from observations of the Cas A remnant, which is site to a 330 yr old neutron star (Ho & Heinke, 2009). The cooling curves of the Cas A remnant are consistent with the phase transition to neutron superfluidity through the formation of cooper pairs [Shternin et al. (2011) and Page et al. (2011)]. Importantly, in most models the protons would already be superconducting, so that after the phase transition to neutron superfluidity there are two coexisting, interacting quantum liquids in the core. This will be of importance in Chapter 6, where we discuss the consequences of these interactions for the evolution of the magnetic field.

## 2.4 Magnetic Field

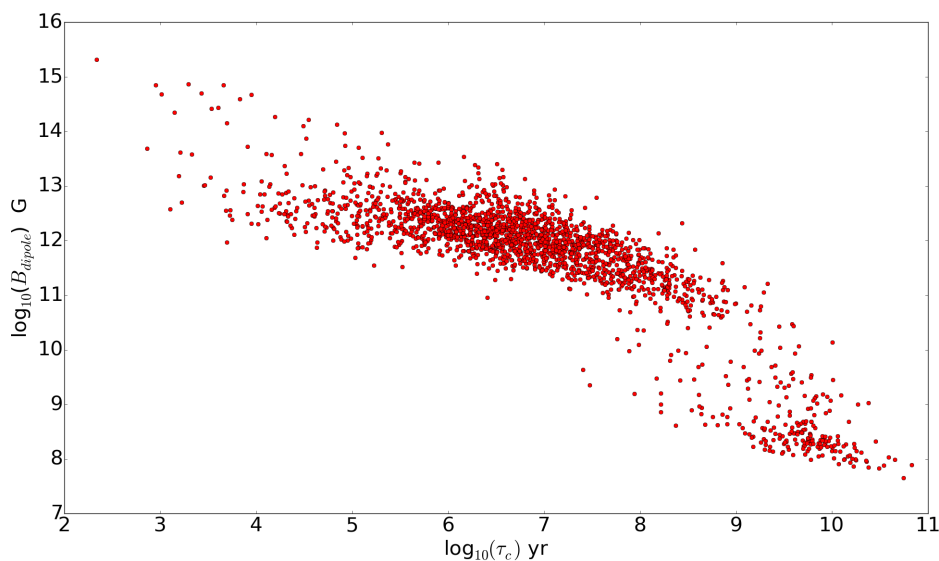


Figure 2.3: Surface dipole field strength ( $B_{\text{dipole}}$ ) and spin-down inferred age ( $\tau_c$ ) of all known neutron stars in the galaxy. Data from the ATNF Pulsar Catalogue (Manchester et al., 2005).

The presence of neutron star magnetic fields was first realized in the explanation of the spin-down of the crab pulsar. If the loss of rotational energy of a neutron star is attributed entirely to a misaligned magnetic dipole, the strength of the dipole component of the magnetic field may be estimated with

$$B = \left( \frac{3}{8\pi^2} \frac{IP\dot{P}c^3}{R_*^6 \sin^2 \theta} \right)^{1/2} = 3.2 \times 10^{19} \sqrt{P\dot{P}} \text{ G}, \quad (2.3)$$

[Kaspi & Kramer (2016)], with  $P$  the spin period,  $\dot{P}$  the period derivative,  $I \sim 10^{46}$  gcm<sup>2</sup> the neutron star moment of inertia, and  $\theta$  the inclination angle of the dipole relative to the spin axis. In reality this formula is too naive. An updated form is given by Spitkovsky (2006) who relaxes the condition of a vacuum magnetosphere. He allows currents to flow through a force free magnetosphere in detailed numerical simulations, and finds the modified field strength

$$B = 3.2 \times 10^{19} \sqrt{P\dot{P}}(1 + \sin^2 \theta)^{-1/2} \text{ G}, \quad (2.4)$$

which can be up to 1.7 times smaller than the vacuum formula.

More recently X-ray spectra of neutron stars have shown signs of cyclotron emission lines, providing a way of independently determining the field strength. Interestingly, a number of measurements have determined field strengths from cyclotron lines which are significantly stronger than the dipole field inferred from spin down measurements [eg. Tiengo et al. (2013), Rodríguez Castillo et al. (2016), Borghese et al. (2017)]. This suggests the presence of higher order multipoles, ie. magnetic loops with a high density of field lines in the presence of a weaker background dipole field.

There is significant evidence to suggest that neutron star magnetic fields evolve with time, on a number of different timescales. Figure 2.3 shows the dipole field strength of known neutron stars in the galaxy, plotted against their respective spin-down inferred ages [Data from ATNF pulsar catalog (Manchester et al., 2005)]. There is a clear trend of older neutron stars having weaker magnetic fields. This has led theorists to speculate that neutron star magnetic fields weaken with time. The activity of magnetars also suggests evolution of strong magnetic fields, powering the observed X-ray outbursts (Kaspi & Beloborodov, 2017). Most recently it has been suggested that repeating FRB's could be powered by the rapid drift of ultra strong magnetic fields inside a newly born magnetar (Beloborodov, 2017).

The evolution of magnetic fields in neutron star crusts is due to Hall drift and Ohmic diffusion. It was studied by Jones (1988), and more definitively by Goldreich & Reisenegger (1992). Hall drift is the non-linear advection of magnetic fields, by the electron currents supporting  $\nabla \times \mathbf{B} = 4\pi/c\mathbf{j}$ . The Hall effect can generate large magnetic shear stresses, countered by the solid stress of the crust. In reality the crust yields elastically to Hall-induced stresses up to a point, beyond which it deforms in the plastic regime [see eg. Levin & Lyutikov (2012), Beloborodov & Levin (2014), Thompson et al. (2017)]. Ohmic diffusion is caused by the finite resistivity of the crustal material due to electron scattering by the ion lattice. This process converts magnetic energy to heat, in contrast to Hall drift which conserves magnetic energy. In neutron stars with magnetic fields  $B \gtrsim 10^{13}$  G, the Hall timescale is shorter than the Ohmic

timescale, making Hall drift the dominant channel of evolution for the crustal magnetic field.

Advances in numerical techniques have allowed Hall drift and Ohmic diffusion of 2D axisymmetric magnetic fields to be studied in numerical simulations, with a variety of pseudo-spectral and grid based methods [Hollerbach & Rüdiger (2002), Pons & Geppert (2007)]. The basic finding was that Hall drift could enhance the transfer of magnetic energy to smaller scales, where Ohmic diffusion proceeds more efficiently. Gourgouliatos & Cumming (2014) found that Hall drift drives itself toward a configuration with uniform electron angular velocity along poloidal field lines. This “Hall attractor” is analogous to Ferraro’s Law in ideal MHD, in which twisted field lines in a cylindrical configuration will evolve to a state with constant angular velocity along field lines (Ferraro, 1937). The Hall attractor has interesting implications for the active periods of magnetars and other transients. Most recently Hall drift has been simulated numerically in 3D (Wood & Hollerbach, 2015). Gourgouliatos et al. (2016) found that Hall drift can generate localized patches of high magnetic field strength in a magnetar crust, where significant heat can be generated through Ohmic diffusion.

There are a number of proposed channels of evolution for the core magnetic field. Most well known is ambipolar diffusion (Goldreich & Reisenegger, 1992), which is the evolution induced by the drift of the charged component through the neutral one, ie. the drift of the proton-electron plasma through the neutrons. Ambipolar diffusion is limited by two factors. Firstly, there is friction between protons and the background neutron fluid. Secondly, departures from chemical equilibrium create pressure gradients which choke the flow of charge currents. Gradients in chemical potential can be erased by weak nuclear interactions. Recently ambipolar diffusion was modeled in 2D by Castillo et al. (2017).

Neutron stars cool as they age and their cores are expected to become superconducting and superfluid (unless the magnetic field is ultra-strong,  $B > 10^{16}$  G, and quenches superconductivity). This results in the quantization of vorticity into vortex lines and magnetic flux – into flux tubes. An important magnetic flux transport mechanism is the drift of superconducting flux tubes. Jones (2006) shows that flux tubes in a superconducting core can move with viscous dissipation through the core fluid, under their own self tension. The drift of flux tubes has a typical velocity  $v \approx 4 \times 10^{-7}$  cm s<sup>-1</sup> for typical pulsars [see section 3 of (Jones, 2006)], making this effect relevant to the depletion of pulsar magnetic fields. We note straight out that this result is controversial, and there is no consensus about it in the theoretical literature; we discuss it below. Furthermore, Ruderman & Sutherland (1974) pointed out that the spin-down of superfluid neutron stars must be associated with the outward motion of superfluid neutron

vortices. [Srinivasan et al. \(1990\)](#), and [Ruderman et al. \(1998\)](#) showed that due to entrainment of superfluid protons the neutron vortices are magnetized and that as consequence, there is a strong interaction between superfluid vortices and superconducting flux tubes. In this picture, the flux tubes may be pulled along with neutron vortices during spin-down.

Axisymmetric magnetic configurations satisfy an MHD equilibrium condition in the azimuthal direction in the core, which we formulate and implement in our simulations. We find that with this equilibrium, the magnetic field in the crust and the core asymptotically settles into the Hall Attractor of [Gourgouliatos & Cumming \(2014\)](#), which was established for crust-confined fields. We explore the evolution of the core magnetic field under Jones' flux tube drift. Our simulations suggest that a combination of Jones' flux tube drift in the core, and Ohmic diffusion in the crust can deplete pulsar magnetic fields on a timescale of 150 Myr, if the crust is hot ( $T \sim 2 \times 10^8$  K). We also consider the hypothesis that the weak-field magnetar can be produced by a neutron star with initially rapid spin and dipole field smaller than the conventional magnetar field. In this scenario, the field is pushed out of the core by the neutron vortices into the crust and thus some of the rotational energy is transformed into magnetic energy. We find that the core magnetic field cannot be expelled when  $B \gtrsim 2 \times 10^{13}$  G. However, for  $B \lesssim 10^{13}$  G, the magnetic field is expelled into the the outer core and deep crust. This drives very strong currents in the deep crust, which are site to enhanced Ohmic dissipation. The strong currents also generate toroidal field through the Hall effect.

# Monash University Declaration Chapter 3

## Declaration by candidate:

I declare that my contribution to the work in Chapter 3 that is submitted to the Monthly Notices of the Royal Astronomical Society as [Bransgrove et al. \(2017\)](#), involved the following:

The writing of the publication, development of the numerical code, running simulations, and all other work contained therein (that is not referenced otherwise).

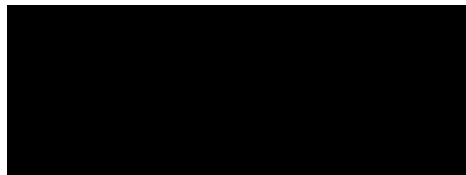
Extent of contribution by candidate: 85%

Co-author names: Yuri Levin, Andrei Beloborodov

Nature of co-author's contribution: Assistance with developing the numerical scheme, formulating boundary conditions, and feedback during writing of the paper.

I have renumbered sections, equations and figures of the published paper in order to generate a consistent presentation within the thesis. The undersigned hereby certify that the above declaration correctly reflects the nature and extent of the student's and co-authors' contributions to this work.

Candidate Signature:



Date:

June 29, 2017

Main Supervisor signature:



Date:

June 29, 2017



## Chapter 3

# Magnetic Field Evolution in Neutron Star Crusts

Partially adapted from:

*Magnetic Field Evolution of Neutron Stars I: Basic formalism, numerical techniques, and first results*, Ashley Bransgrove, Yuri Levin, and Andrei Beloborodov, 2017, submitted for publication in MNRAS.

### 3.1 Hall Drift and Ohmic Diffusion

The evolution of the magnetic field in a neutron star crust satisfies Faraday's Law,

$$\frac{\partial \mathbf{B}}{\partial t} = -c \nabla \times \mathbf{E}, \quad (3.1)$$

with  $\mathbf{E}$  an induction field. An expression for the induction field can be found by considering the force balance for the electrons in the crust. In the non-inertial limit, the sum of forces acting on the electrons must equal zero,

$$0 = -e \left( \mathbf{E} + \frac{\mathbf{v}_e}{c} \times \mathbf{B} \right) - n_e m_e^* \nu_{ei} (\mathbf{v}_e - \mathbf{v}_i). \quad (3.2)$$

Here  $\mathbf{v}_e$  is the electron velocity,  $\mathbf{v}_i$  is the velocity of the positively charged ion lattice,  $n_e$  is the electron number density,  $m_e^*$  the electron effective mass, and  $\nu_{ei}$  the electron collision frequency. The first term in brackets is the Lorentz force, while the second represents the collective drag on electrons due to collisions in the rest frame of the ion lattice. Physically electrons can scatter off impurities in the lattice, and phonons. Solving this expression for the electric field, gives

$$\mathbf{E} = -\frac{\mathbf{v}_e}{c} \times \mathbf{B} + \frac{\mathbf{j}}{\sigma}, \quad (3.3)$$

where we have identified the current density

$$\mathbf{j} = -en_e(\mathbf{v}_e - \mathbf{v}_i), \quad (3.4)$$

and the electrical conductivity

$$\sigma = \frac{n_e e^2}{m_e^* \nu_{ei}}. \quad (3.5)$$

Substituting (5.48) into (3.1) yields the following evolution equation for the magnetic field,

$$\frac{\partial \mathbf{B}}{\partial t} = \nabla \times (\mathbf{v}_e \times \mathbf{B}) - c \nabla \times \left( \frac{\mathbf{j}}{\sigma} \right) \quad (3.6)$$

We can write the electron velocity in terms of the Hall drift velocity,  $\mathbf{v}_{\text{hall}}$ , and  $\dot{\xi} = \mathbf{v}_i$  the displacement velocity of the ion lattice,

$$\mathbf{v}_e = \mathbf{v}_{\text{hall}} + \dot{\xi}. \quad (3.7)$$

The Hall drift velocity describes the velocity of electrons relative to ions, and is given by

$$\mathbf{v}_{\text{hall}} = -\frac{\mathbf{j}}{n_e e} = -\frac{c}{4\pi n_e e} \nabla \times \mathbf{B}. \quad (3.8)$$

We may now write the evolution equation for the magnetic field in terms of the field itself, and the crustal displacement velocity,

$$\frac{\partial \mathbf{B}}{\partial t} = -\frac{c}{4\pi e} \nabla \times \left( \frac{\nabla \times \mathbf{B}}{n_e} \times \mathbf{B} \right) + \nabla \times (\dot{\xi} \times \mathbf{B}) - \frac{c^2}{4\pi} \nabla \times \left( \frac{\nabla \times \mathbf{B}}{\sigma} \right). \quad (3.9)$$

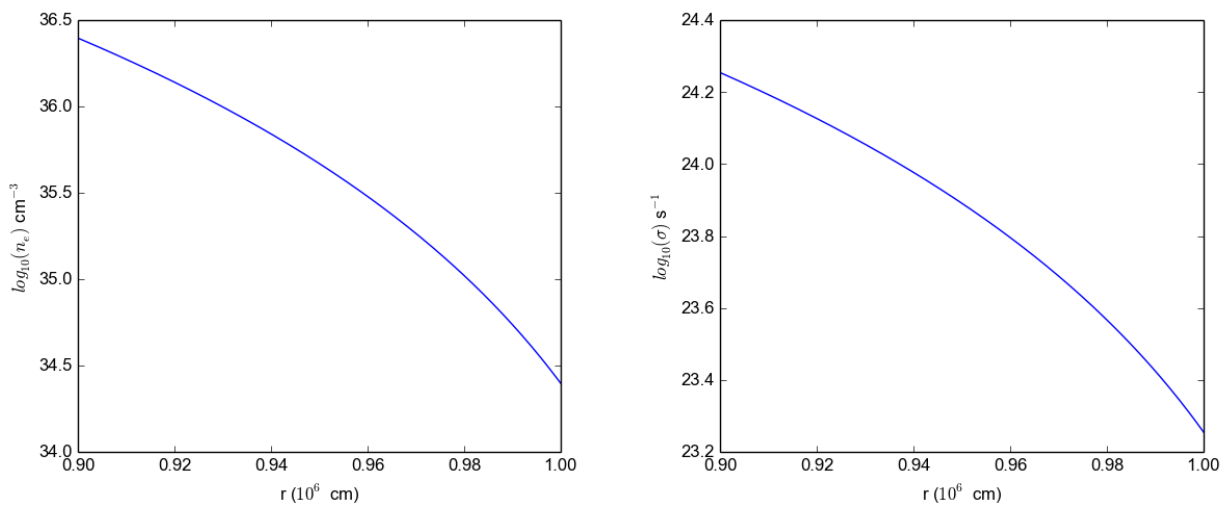


Figure 3.1: Electron density ( $n_e$ ) and electrical conductivity ( $\sigma$ ) profiles we use in our numerical models, following [Gourgouliatos & Cumming \(2014\)](#).

The dynamics of the crust and the way we calculate  $\dot{\xi}$  is outlined in Chapter 7.

The electron density can be written as  $n_e = Y_e n_b$ , with  $Y_e$  the electron fraction, and  $n_b$  the baryon density. [Chamel & Haensel \(2008\)](#) give the baryon density at the base of the crust as  $n_b \approx 0.08 \text{ fm}^{-3}$ , and the corresponding electron fraction  $Y_e \sim 0.03$ . The electron density at the base of the crust is then calculated as  $n_e = 2.5 \times 10^{36} \text{ cm}^{-3}$ . In our numerical experiments we follow [Gourgouliatos & Cumming \(2014\)](#) and take  $n_e \propto z^4$ . Specifically we use

$$n_e \propto \left( \frac{1.0463r_* - r}{0.0463r_*} \right)^4, \quad (3.10)$$

with  $r_*$  the radius of the star. Following [Gourgouliatos & Cumming \(2014\)](#) we take  $\sigma \propto n_e^{2/3}$ , which is somewhere between the density scalings expected for phonon scattering and impurity scattering. We set the electrical conductivity to vary from  $\sigma = 3.6 \times 10^{24} \text{ s}^{-1}$  at the base of the crust, to  $\sigma = 1.8 \times 10^{23} \text{ s}^{-1}$  at the surface, which is appropriate for phonon scattering at  $T \approx 2 \times 10^8 \text{ K}$ , or impurity scattering with  $Q_{\text{imp}} \approx 3$  ([Gourgouliatos & Cumming, 2014](#)). These are within an order of magnitude of the values used by [Viganò et al. \(2013\)](#).

## 3.2 Characteristic Time Scales

The complete magnetic field evolution equation in the crust is given as

$$\frac{\partial \mathbf{B}}{\partial t} = -\frac{c}{4\pi e} \nabla \times \left( \frac{\nabla \times \mathbf{B}}{n_e} \times \mathbf{B} \right) + \nabla \times (\dot{\xi} \times \mathbf{B}) - \frac{c^2}{4\pi} \nabla \times \left( \frac{\nabla \times \mathbf{B}}{\sigma} \right). \quad (3.11)$$

The terms on the right hand side describe, in order, the effects of Hall drift, crustal deformation, and Ohmic diffusion. The Hall term corresponds to the nonlinear advection of the magnetic fields by the currents which support  $\nabla \times \mathbf{B} = 4\pi/c\mathbf{j}$ . The Hall term conserves magnetic energy. The second term corresponds to crustal deformation, in a way that minimizes magnetic stress, and partially cancels the Hall term. If the crustal displacement is due to elastic deformations only, then the second term will conserve magnetic energy. The third term represents diffusion of magnetic field lines due to the Ohmic scattering of currents. The Ohmic term converts magnetic energy into heat. We can define the ‘Hall Magnetic Reynolds number’

$$\mathcal{R}_B = \frac{\sigma B}{n_e e c}, \quad (3.12)$$

as the ratio between the coefficients of the Hall and Ohmic terms in the induction equation. If  $\mathcal{R}_B$  is large then the Hall effect dominates the evolution timescale. Likewise if  $\mathcal{R}_B$  is small, Ohmic diffusion dominates the evolution timescale.

We can determine the characteristic timescales of evolution of the Hall and Ohmic terms, with  $L$  a characteristic length scale, taken to be the thickness of the crust (1 km) and  $n_e$  and  $\sigma$  evaluated at the base of the crust,

$$t_{\text{ohm}} \sim \frac{4\pi\sigma L^2}{c^2} = 13.5 \left( \frac{L}{1\text{km}} \right)^2 \left( \frac{\sigma}{3.6 \times 10^{24} \text{ s}^{-1}} \right) \text{Myr}, \quad (3.13)$$

$$t_{\text{hall}} \sim \frac{4\pi e L^2 n_e}{cB} = \frac{1.6}{B_{14}} \left( \frac{L}{1\text{km}} \right)^2 \left( \frac{n_e}{2.5 \times 10^{36} \text{ cm}^{-3}} \right) \text{Myr} \quad (3.14)$$

where  $B_{14}$  is the magnetic field strength in units of  $10^{14}$  G.

### 3.3 Axisymmetric Equations

We now follow closely the formalism of [Gourgouliatos & Cumming \(2014\)](#). In axisymmetry the magnetic field can be decomposed into poloidal and toroidal components, and expressed in terms of the scalar functions  $\Psi$  and  $I$ . The magnetic field is written as a sum of poloidal ( $\mathbf{B}_p$ ) and

toroidal ( $\mathbf{B}_T$ ) components

$$\mathbf{B} = \mathbf{B}_p + \mathbf{B}_T = \nabla\Psi \times \nabla\phi + I\nabla\phi, \quad (3.15)$$

where we work in spherical coordinates  $(r, \theta, \phi)$ , and define  $\nabla\phi \equiv \hat{e}_\phi/r\sin\theta$ . The function  $\Psi$  is known as the flux function (identical in form to the Stokes stream function), since  $2\pi\Psi(r, \theta)$  is the poloidal magnetic flux passing through the polar cap with radius  $r$  and opening angle  $\theta$ . The function  $I$  has the interpretation that  $cI(r, \theta)/2$  is the poloidal current passing through the same polar cap, and hence is often called the poloidal current function.

We now express the evolution equation (3.9) in terms of the scalar functions  $\Psi$  and  $I$  as defined in (3.32). Evolving fields in this formalism has the advantage of automatically preserving  $\nabla \cdot \mathbf{B} = 0$  at all times, provided the scalar functions  $\Psi$  and  $I$  are differentiable. We begin by defining the quantity

$$\chi = \frac{c}{4\pi en_e r^2 \sin^2\theta}, \quad (3.16)$$

as in [Gourgouliatos & Cumming \(2014\)](#). We also write the toroidal current as

$$\mathbf{j}_T = \frac{c}{4\pi} \nabla \times \mathbf{B}_p = -\frac{c}{4\pi} \Delta^* \Psi \nabla\phi, \quad (3.17)$$

and the electron angular velocity as

$$\Omega_e = \Omega_{\text{hall}} + \Omega_{\text{el}} = -\frac{j_T}{n_e e r \sin\theta} + \frac{v_{\text{el}}^\phi}{r_\perp} = \chi \Delta^* \Psi + \frac{v_{\text{el}}^\phi}{r_\perp}, \quad (3.18)$$

where we have used the Grad-Shafranov operator,

$$\Delta^* = \frac{\partial^2}{\partial r^2} + \frac{\sin\theta}{r^2} \frac{\partial}{\partial \theta} \left( \frac{1}{\sin\theta} \frac{\partial}{\partial \theta} \right). \quad (3.19)$$

Using the above definitions, the Hall evolution equation reduces to the following two scalar equations, in terms of the poloidal and toroidal scalar functions

$$\frac{\partial \Psi}{\partial t} - r^2 \sin^2\theta \chi (\nabla I \times \nabla\phi) \cdot \nabla\Psi = \frac{c^2}{4\pi\sigma} \Delta^* \Psi, \quad (3.20)$$

$$\frac{\partial I}{\partial t} + r^2 \sin^2 \theta [(\nabla \Omega_{\text{hall}} \times \nabla \phi) \cdot \nabla \Psi + (\nabla \Omega_{\text{el}} \times \nabla \phi) \cdot \nabla \Psi + I(\nabla \chi \times \nabla \phi) \cdot \nabla I] = \frac{c^2}{4\pi\sigma} \left( \Delta^* I - \frac{1}{\sigma} \nabla I \cdot \nabla \sigma \right). \quad (3.21)$$

These evolution equations are the same as those in [Gourgouliatos & Cumming \(2014\)](#), except for the addition of the elastic back-reaction velocity of the crust. It is clear that for our profiles of  $n_e$  and  $\sigma$ , the magnetic Reynolds number is largest at the surface. We do not include the upper layers of the crust where  $\mathcal{R}_B > 100$  [Equation (3.12)], in order to avoid time stepping issues where the Hall evolution is very fast. This corresponds to a minimum electron density cutoff of  $2.5 \times 10^{34} \text{ cm}^{-3}$  for our choice of conductivity, and a magnetic field of strength  $\sim 2 \times 10^{14} \text{ G}$ . The layers we exclude will have mass density  $\rho \lesssim 10^{11} \text{ g cm}^{-3}$ .

### 3.4 Hall Attractor

[Cumming et al. \(2004\)](#) first showed that rigid rotation of electrons along poloidal field lines was a steady state of the Hall evolution equations. The Hall Attractor was later found to exist for axisymmetric, crust-confined, magnetic fields in numerical simulations [[Gourgouliatos & Cumming \(2014\)](#)]. Here we give a brief overview of Ferraro's law of isorotation in ideal MHD [[Ferraro \(1937\)](#)], which is analogous to the Hall Attractor in Hall evolution. We then discuss the Hall Attractor for axisymmetric magnetic fields.

We begin by considering an axisymmetric magnetic field in cylindrical coordinates. The fluid flow is constrained to be purely azimuthal,

$$\mathbf{v} = r_{\perp} \Omega \hat{\mathbf{e}}_{r_{\perp}}, \quad (3.22)$$

with  $r_{\perp} = r \sin \theta$ , and  $\Omega$  the angular velocity of the fluid. For this configuration it can be shown that

$$\frac{\partial \mathbf{B}_p}{\partial t} = 0. \quad (3.23)$$

Here the poloidal field is  $\mathbf{B}_p = B_{r_{\perp}} \hat{\mathbf{e}}_{r_{\perp}} + B_z \hat{\mathbf{e}}_z$ . The evolution of the toroidal field can be written as

$$\frac{\partial B_{\phi}}{\partial t} = r_{\perp} (\mathbf{B}_p \cdot \nabla) \Omega. \quad (3.24)$$

It is easy to see that when  $\Omega$  is constant along poloidal field lines, there is no evolution of the magnetic field, i.e. it is a steady state. This is Ferraro's Law in ideal MHD. For Hall drift in axisymmetry, the attractor state corresponds to

$$\Omega_e \longrightarrow \Omega_e(\Psi), \quad (3.25)$$

that is, rigid rotation of electrons along poloidal field lines. We will discuss this result further in Chapter 4. We find that the Hall Attractor of Gourgouliatos and Cumming also exists for B-fields which penetrate the neutron star core.

## 3.5 Computational Methods

### 3.5.1 Boundary Conditions

We give an overview of the boundary conditions which are common between all simulations. Depending on the simulation, certain boundary conditions may change significantly, but this will be noted as necessary. Since we are working in axisymmetry, we must enforce continuity of the magnetic field at the poles of the star. This ensures that the field is purely radial, and has no polar or azimuthal component at  $\theta = 0$  and  $\theta = \pi$ . We set

$$B_\phi(r, \theta = 0) = B_\phi(r, \theta = \pi) = 0, \quad (3.26)$$

to enforce zero azimuthal component. But since  $I$  is defined as

$$B_\phi = \frac{I}{r \sin \theta} \hat{e}_\phi, \quad (3.27)$$

we see that  $I$  must tend to zero at least as fast as  $\sin \theta = \theta + \mathcal{O}(\theta^3)$ , in order to prevent a coordinate singularity. Ensuring that

$$I(r, \theta = 0) = I(r, \theta = \pi) = 0 \quad \text{and} \quad \left. \frac{\partial I}{\partial \theta} \right|_{\theta=0,\pi} = 0 \quad (3.28)$$

means that the singularity will be properly regularized. To enforce the condition on the flux function, we use (3.32), to see that

$$B_\theta(r, \theta = 0) = B_\theta(r, \theta = \pi) = \frac{1}{r^2 \sin \theta} \left. \frac{\partial \Psi}{\partial r} \right|_{\theta=0,\pi} = 0, \quad (3.29)$$

where we again note that there is a coordinate singularity in  $\theta$ . We may regularize this by ensuring that

$$\left. \frac{\partial \Psi}{\partial r} \right|_{\theta=0,\pi} = 0 \quad \text{and} \quad \left. \frac{\partial}{\partial \theta} \left( \frac{\partial \Psi}{\partial r} \right) \right|_{\theta=0,\pi} = 0 \quad (3.30)$$

The first condition is satisfied when

$$\Psi(r, \theta = 0) = \Psi(r, \theta = \pi) = 0. \quad (3.31)$$

### 3.5.2 Matching the Crust Field to the Magnetosphere

In order to solve the evolution Equations (3.20) and (3.21) we need two boundary conditions, for  $I$  and  $\Psi$  at  $r_*$ , which may also be formulated as conditions on  $\mathbf{B}(r_*, \theta)$ . In this work we are considering a slow evolution of magnetic fields on timescales over which any episodic magnetospheric twists (magnetar activity) must be erased (Beloborodov, 2009). It is therefore reasonable to assume a vacuum magnetic field as the boundary condition at the surface. Demanding zero current means that  $\nabla \times \mathbf{B} = 0$  outside the star. So we can write the vacuum field as

$$\mathbf{B} = \nabla V, \quad (3.32)$$

where  $V$  is a scalar function. We also assume that there is no surface current at  $r_*$  due to the finite electrical conductivity of the outer crust. Thus, the two boundary conditions express the continuity of the tangential components of the magnetic field  $B_\phi$ ,  $B_\theta$ , at the surface, so that they match a vacuum solution outside the star:

1. The continuity of  $B_\phi$  implies for the crustal field  $B_\phi(r_*, \theta) = 0$ , since in any axisymmetric vacuum magnetosphere  $B_\phi = (r \sin \theta)^{-1} \partial V / \partial \phi = 0$ . This gives  $I(r_*, \theta) = 0$ .
2. The continuity of  $B_\theta$  gives a condition on  $\partial \Psi / \partial r = -r \sin \theta B_\theta$  (no boundary condition is imposed on the values of  $\Psi(r_*, \theta)$  – its evolution is calculated from Equation (3.20) in the crust).

The constraint  $\nabla \cdot \mathbf{B} = 0$ , gives the Laplace equation for  $V$ ,

$$\nabla^2 V = 0. \quad (3.33)$$

$B_\theta$  is determined by this Laplace equation outside the star for given surface values of  $B_r$ . Because  $V \rightarrow 0$  as  $r \rightarrow \infty$ , we can write the solution as a multipolar expansion. For axisymmetric magnetic fields  $V$  is given by

$$V(r, \theta) = \sum_{l=1}^{\infty} \frac{a_l}{r^{l+1}} P_l(\cos \theta), \quad (3.34)$$

where  $P_l(\cos \theta)$  are the associated Legendre polynomials. The first sum starts at  $l = 1$  because there are no magnetic monopoles, and  $a_l$  are expansion coefficients to be determined. Now using the definition of the magnetic field in Equation (3.32), we can write

$$B_r(r, \theta) = \frac{\partial V}{\partial r} = - \sum_{l=1}^{\infty} (l+1) \frac{a_l}{r^{l+2}} P_l(\cos \theta). \quad (3.35)$$

We can invert this expression to solve for the expansion coefficients, and evaluate it at  $r_*$  which gives

$$a_l = -r_*^{l+2} \frac{2l+1}{2l+2} \int_0^\pi P_l(\cos\theta) B_r(r_*, \theta) \sin\theta d\theta. \quad (3.36)$$

Using these expansion coefficients, we can calculate  $B_\theta$  using Equation (3.32),

$$B_\theta(r, \theta) = \frac{1}{r} \frac{\partial V}{\partial \theta} = \sum_{l=1}^{\infty} \frac{a_l}{r^{l+2}} \frac{\partial P_l(\cos\theta)}{\partial \theta} = -\frac{1}{r \sin\theta} \frac{\partial \Psi}{\partial r}. \quad (3.37)$$

This gives the boundary condition for  $\Psi$  on the surface of the star as

$$\left. \frac{\partial \Psi}{\partial r} \right|_{r_*} = -\sin\theta \sum_{l=1}^{\infty} \frac{a_l}{r_*^{l+1}} \frac{\partial P_l(\cos\theta)}{\partial \theta}. \quad (3.38)$$

### 3.5.3 Numerical Scheme

We evolve the poloidal and toroidal scalar functions on a discrete grid, which is linear in  $r$  and  $u \equiv \cos\theta$ , in the crust and the core. The variable  $u$  varies from -1 at the south pole, to 1 at the north pole, and the radius of the star is  $r_* = 1$  in units of  $10^6$  cm. The crust core interface is at  $r_c = 0.9r_*$ . We use the indices  $i$  and  $j$  to specify grid points in the  $r$  and  $u$  directions respectively. The index  $j$  varies from  $j_1 = -50$  which corresponds to the south pole, to  $j_2 = 50$  which corresponds to the north pole, with  $j = 0$  defining the equator. We choose the difference in  $u$  such that  $\delta u = 2/(j_2 - j_1)$ . The index  $i$  varies from  $i_0 = 0$  at the center ( $r = 0$ ), to typical values of  $i_c = 350$  at the crust core interface ( $r = r_c$ ) depending on the simulation. For most simulations  $i$  extends to  $i_s = i_c + 100$  at the surface (ie. a crustal grid of  $101 \times 101$ ), though for some simulations higher resolution is required in the radial direction in the crust. Throughout the crust and the last few rows of the core (ghost points for the crust) the radial grid spacing is  $\delta r_{\text{crust}} = 1/i_s$ . The radial grid spacing in the outer few rows of the core grid matches the radial grid spacing of the crust, for ease of implementing boundary conditions on the crustal field. In order to avoid numerical instabilities near the poles in some simulations, we added adjustable patches of increased resolution in the  $u$  direction. The angular resolution was sometimes set to between 6 and 10 times the original resolution near the poles in order to obtain convergence. This resolved the issue of numerical instabilities, and added little expense to the computations.

We evaluate spatial derivatives in the crustal evolution equations [Equations (3.20), (3.21), (7.20)] with the following finite difference formulae. To evaluate the radial derivatives at each time step in the crust we use

$$\Psi_r = \frac{\Psi_{j,i+1} - \Psi_{j,i-1}}{2\delta r}, \quad (3.39)$$

$$\Psi_{rr} = \frac{\Psi_{j,i-1} - 2\Psi_{j,i} + \Psi_{j,i+1}}{\delta r^2}, \quad (3.40)$$

with the subscript a short hand for partial derivative. For the derivatives with respect to  $u$  however, a different approach was needed, since central differences do not preserve second order accuracy on a non-uniform grid. We use the following finite differences which are generalized to maintain second order accuracy [Equations A3b, and A4c in [Bowen & Smith \(2005\)](#)]. These are found by using Lagrange interpolation to fit a polynomial to the points, and then taking a derivative of that polynomial. We first define the displacements  $\alpha_j = u_j - u$ , where  $u$  is the point at which we evaluate the derivative, and  $u_j$  is a grid point. The point  $u$  may be any point contained by the grid points  $(j-1, j, j+1)$ , not necessarily a grid point. The first and second derivatives with respect to  $u$  are then

$$\Psi_u = -\frac{(\alpha_2 + \alpha_3)\Psi_{j-1,i}}{(\alpha_1 - \alpha_2)(\alpha_1 - \alpha_3)} - \frac{(\alpha_1 + \alpha_3)\Psi_{j,i}}{(\alpha_2 - \alpha_1)(\alpha_2 - \alpha_3)} - \frac{(\alpha_1 + \alpha_2)\Psi_{j+1,i}}{(\alpha_3 - \alpha_1)(\alpha_3 - \alpha_2)}, \quad (3.41)$$

$$\begin{aligned} \Psi_{uu} = & -\frac{2(\alpha_2 + \alpha_3 + \alpha_4)\Psi_{j-2,i}}{(\alpha_1 - \alpha_2)(\alpha_1 - \alpha_3)(\alpha_1 - \alpha_4)} - \frac{2(\alpha_1 + \alpha_3 + \alpha_4)\Psi_{j-1,i}}{(\alpha_2 - \alpha_1)(\alpha_2 - \alpha_3)(\alpha_2 - \alpha_4)} \\ & - \frac{2(\alpha_1 + \alpha_2 + \alpha_4)\Psi_{j,i}}{(\alpha_3 - \alpha_1)(\alpha_3 - \alpha_2)(\alpha_3 - \alpha_4)} - \frac{2(\alpha_1 + \alpha_2 + \alpha_3)\Psi_{j+1,i}}{(\alpha_4 - \alpha_1)(\alpha_4 - \alpha_2)(\alpha_4 - \alpha_3)}. \end{aligned} \quad (3.42)$$

We use the same derivative formula for the toroidal scalar function  $I$ . In the code we normalize the Hall Evolution equation in the same way as [Gourgouliatos & Cumming \(2014\)](#),

$$1.6 \times 10^6 \frac{\partial \mathbf{B}_{14}}{\partial t_{\text{yr}}} = -\tilde{\nabla} \times \left( \frac{\tilde{\nabla} \times \mathbf{B}_{14}}{n_{e,0}} \times \mathbf{B}_{14} \right) - 0.02 \tilde{\nabla} \times \left( \frac{\tilde{\nabla} \times \mathbf{B}_{14}}{\sigma_0} \right), \quad (3.43)$$

where  $\mathbf{B}_{14} = \mathbf{B}/10^{14}$  G,  $t_{\text{yr}} = t/3.15 \times 10^7$  s,  $\tilde{\nabla}$  is the del operator with lengths normalized to  $10^6$  cm,  $n_{e,0} = n_e/2.5 \times 10^{34}$  cm $^{-3}$ , and  $\sigma_0 = \sigma/1.8 \times 10^{23}$  s $^{-1}$ . For more details of the numerical method we refer the reader to Appendix B.

## 3.6 Test Problems

In this section we show tests of our numerical scheme for Hall drift and Ohmic diffusion. Firstly, we test the Ohmic terms in Equations (3.20) and (3.21) by comparing with the analytic Ohmic eigenmodes. We show that our code demonstrates second order spatial convergence. Since there are no known analytic solutions to the non-linear Hall terms, we instead compare our results with the code of [Gourgouliatos & Cumming \(2014\)](#). We observe excellent agreement.

Purely toroidal fields evolving through Ohmic diffusion, with a uniform conductivity, satisfies the following evolution equation,

$$\frac{\partial \mathbf{B}}{\partial t} = -\frac{c^2}{4\pi\sigma} \nabla \times (\nabla \times \mathbf{B}). \quad (3.44)$$

This equation has analytic solutions [first shown by Chandrasekhar (1961)], given in terms of the scalar function  $I$  by

$$I(r, \theta, t) = r^2[Aj_n(kr) + By_n(kr)] \sin \theta P_l^1(\cos \theta) e^{-t/\tau}, \quad (3.45)$$

with  $A$  and  $B$  constants, the ratio of which depends on the boundary conditions, and  $k = 1/\sqrt{\eta\tau}$ . The decay timescale  $\tau$  depends on the boundary conditions chosen. For the lowest order radial mode ( $n = 0$ ), with  $B_\phi(r = r_c) = B_\phi(r = r_*) = 0$ , it is easy to show that the characteristic decay time is

$$\tau = \left( \frac{r_* - r_c}{\pi} \right)^2 \frac{1}{\eta}. \quad (3.46)$$

The characteristic decay times for higher order radial modes are non-trivial to find. We run our code using the  $n = 0$   $l = 1$  Ohmic eigenmode as an initial condition. We eliminate error from the time stepping by scaling the time step. That is, when we double the grid spacing, we divide the time step by 4, so that we are effectively using the same time step size for all grid resolutions.

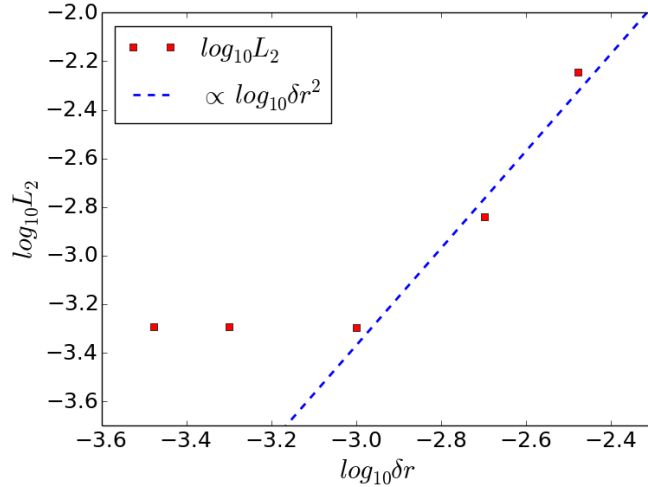


Figure 3.2:  $\log_{10} L_2$  vs.  $\log_{10} \delta r$ : Comparison of our code with the analytic  $n = 0$   $l = 1$  Ohmic eigenmode.

In order to compare the analytic and numerical solutions we use the  $L_2$  norm, defined

$$L_2 = \sqrt{\frac{1}{N} \sum_{i,j} |x_{i,j} - y_{i,j}|^2}, \quad (3.47)$$

where the sum is performed over the whole grid, with  $x_{i,j}$  and  $y_{i,j}$  the analytic and numeric solutions at a grid point. We normalize by  $N$  the number of grid points. Since the slope in

Figure 3.2 is  $\approx 2$ , our scheme is converging to second order spatial accuracy. The error levels off in the left region of the plot, because the scheme has converged for these high resolution trials.

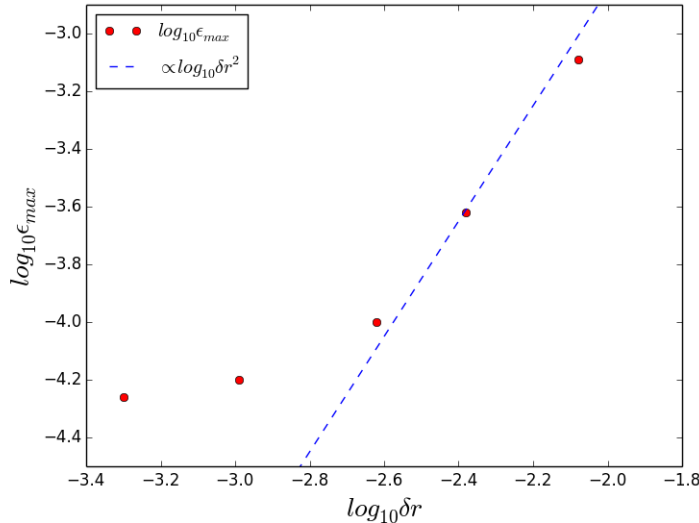


Figure 3.3:  $\log_{10} \epsilon_{max}$  vs.  $\log_{10} \delta r$ : Comparisson of our code with the analytic  $n = 0$   $l = 1$  Ohmic eigenmode.

In addition to testing the convergence of our numerical scheme with the  $L_2$  norm, we perform a check on the absolute error of individual grid cells. We define

$$\epsilon_{max} = \max |x_{i,j} - y_{i,j}|, \quad (3.48)$$

with  $x_{i,j}$  and  $y_{i,j}$  the analytic and numeric solutions at a grid point. The maximum is taken over the whole grid. This check ensures that there are no local errors growing large, while the global error we studied with  $L_2$  grows smaller. In Figure 3.3 the slope has gradient  $\approx 2$ , which implies the convergence is second order accuracy. The data points level off in the left region of the plot because the scheme has converged.

We test the Hall terms in the evolution Equations (3.20) and (3.21) by comparing our code with that of [Gourgouliatos & Cumming \(2014\)](#). Using the so-called ‘‘Hall equilibrium’’ initial magnetic field, we simulate for 2 Myr using the same electrical conductivity and electron density profile as [Gourgouliatos & Cumming \(2014\)](#). The results of our code are shown alongside theirs in Figure 3.4. We observe excellent agreement.

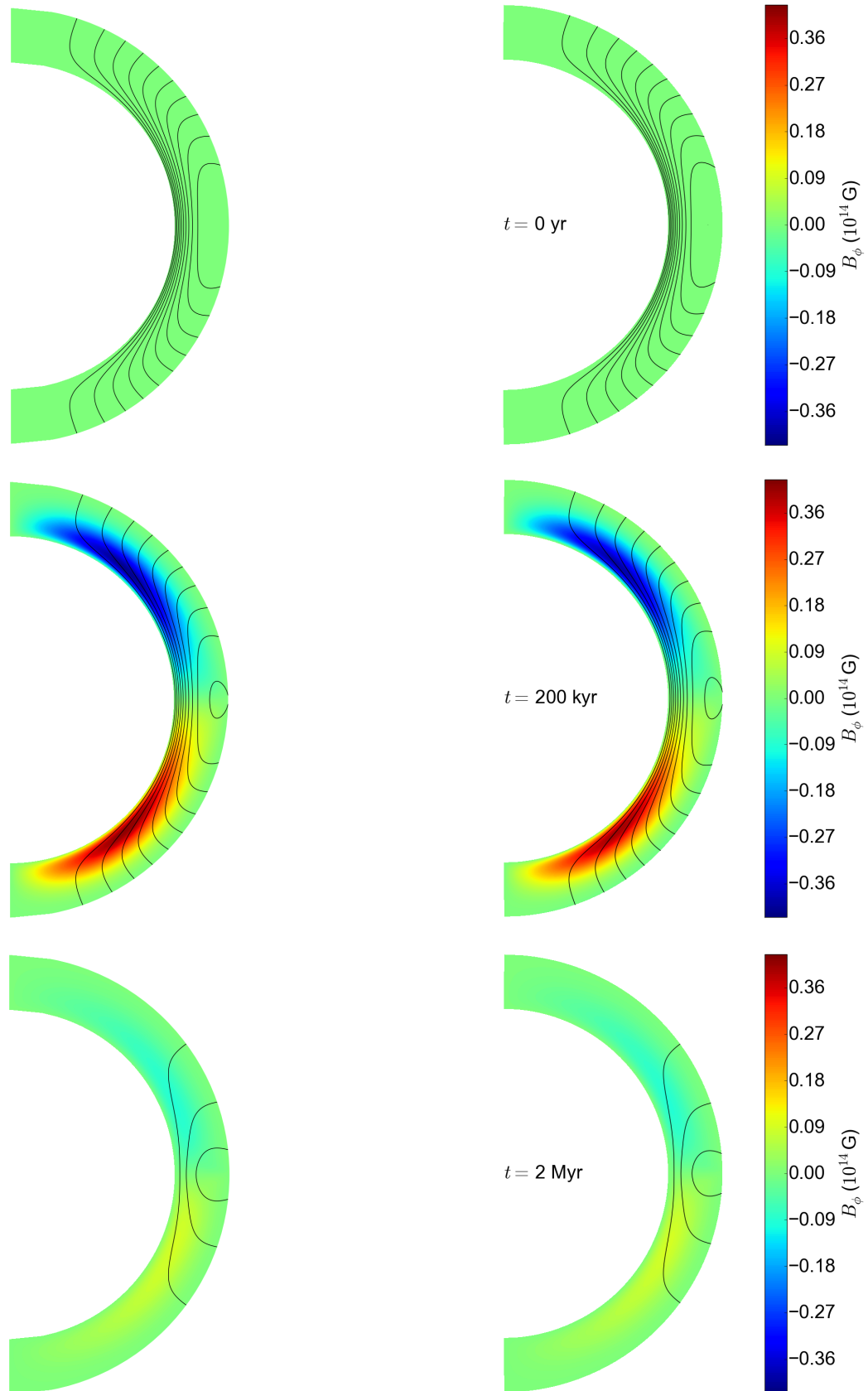


Figure 3.4: Evolution of the so-called “Hall equilibrium” with Hall Drift and Ohmic Diffusion. The images on the left are plotted from data files provided by [Gourgouliatos & Cumming \(2014\)](#), and the images on the right are the results of our own code. In this figure the thickness of the crust has been scaled by a factor of 2.5 for clarity.

# Monash University Declaration Chapter 4

## Declaration by candidate:

I declare that my contribution to the work in Chapter 4 that is submitted to the Monthly Notices of the Royal Astronomical Society as [Bransgrove et al. \(2017\)](#), involved the following:

The writing of the publication, formulating the hydromagnetic equilibrium, development of numerical methods including boundary conditions, development of the numerical code, running simulations, and all other work contained therein (that is not referenced otherwise).

Extent of contribution by candidate: 85%

Co-author names: Yuri Levin, Andrei Beloborodov

Nature of co-author's contribution: Formulating the hydromagnetic equilibrium, development of numerical methods including boundary conditions, and feedback during writing of the paper.

I have renumbered sections, equations and figures of the published paper in order to generate a consistent presentation within the thesis. The undersigned hereby certify that the above declaration correctly reflects the nature and extent of the student's and co-authors' contributions to this work.

Candidate Signature:

Date: June 29, 2017

Main Supervisor signature:



Date: June 29, 2017

# Chapter 4

## Magnetic Coupling of the Crust and the Core

Partially adapted from:

*Magnetic Field Evolution of Neutron Stars I: Basic formalism, numerical techniques, and first results*, Ashley Bransgrove, Yuri Levin, and Andrei Beloborodov, 2017, submitted for publication in MNRAS.

## 4.1 Hydromagnetic Equilibrium

In this section we outline two methods for studying the evolution of neutron star core magnetic fields on long (Hall) timescales, while maintaining stability on dynamical (MHD) timescales, and taking into account fluid degrees of freedom. The core has a very high conductivity and we treat it as an ideal conductor, so that the field is perfectly coupled to the fluid. It is then instructive to consider displacements of the fluid, since these correspond directly to degrees of freedom of the field. Firstly we assume there is no bulk fluid displacement in the radial direction  $\xi_r = 0$  on an Alfvén timescale because of the stable stratification (there may be a slow drift due to secular effects which we discuss later on). We also assume that the core is incompressible, which in axisymmetry implies  $\xi_\theta = 0$ . In this axisymmetric model, the core fluid can only be displaced in the azimuthal direction, which corresponds to the motion of fluid elements on spherical shells, at fixed cylindrical radius. Such displacements in the  $\phi$  direction do not perturb the local chemical equilibrium, and are only limited by the viscosity of the fluid which is negligible. Thus, it is a good approximation to assume that any toroidal flux injected into the core, readily distributes itself according to a tension equilibrium along poloidal field lines. This is equivalent to the force  $f_\phi = \mathbf{j}_p \times \mathbf{B}_p / c = 0$  in axisymmetry, but in general it is the vanishing of the solenoidal part of the Lorentz force. In terms of the scalar functions  $I$  and  $\Psi$ , this condition is equivalent to

$$I = I(\Psi), \quad (4.1)$$

which means that  $I$  is constant along poloidal field lines in the core. We present two methods enforcing this condition. We briefly outline the first method here, but leave the details for the appendix.

## 4.2 Method I: Flux Coordinates

Firstly, it is possible to determine the value of  $I$  along a given poloidal field line in the core by calculating the advection flux of  $B_\phi$  into the core by Hall drift. The advection flux of  $B_\phi$  is defined by writing the Hall evolution equation for  $B_\phi$  in the crust in conservative form, and identifying the advection flux. In this method it is convenient to work in the so-called flux-coordinates  $(\Psi, \lambda, \phi)$ , where  $\Psi$  labels surfaces of constant poloidal flux, and  $\lambda$  is the length along a given poloidal field line in the  $\phi = \text{const}$  plane (Goedbloed et al., 2010). It can be shown (Appendix A), that the twist angle  $\zeta$  of a given poloidal field line in the core evolves according to the equation

$$\frac{\partial \zeta(\Psi)}{\partial t} = -[J(\Psi, \lambda_2, t) - J(\Psi, \lambda_1, t)], \quad (4.2)$$

where we have identified the twist angle

$$\zeta(\Psi) = \int_{\lambda_1}^{\lambda_2} d\lambda \left( \frac{B_\phi}{r_\perp B_\lambda} \right), \quad (4.3)$$

where the integral is taken along the magnetic field line ( $\Psi = \text{const}$ ), and  $J$  is related to the “flux of twist” into the core through

$$F = r_\perp B_\lambda J = v_\lambda B_\phi - v_\phi B_\lambda. \quad (4.4)$$

The rhs of (4.2) represents the difference between flux of twist at each footpoint of a field line threading the core at its boundary. There are two contributions to the flux of twist  $J$ . The first term can be attributed to Hall drift advecting  $B_\phi$  into the core with poloidal drift currents, and the second term is the azimuthal winding of poloidal field lines by Hall drift. Equation (4.2) may be rearranged to obtain the following equation for the evolution of  $I(\Psi)$ ,

$$\frac{\partial I(\Psi, t)}{\partial t} = -\varpi(\Psi)[J(\Psi, \lambda_2, t) - J(\Psi, \lambda_1, t)], \quad (4.5)$$

with

$$\varpi(\Psi) = \left( \int_{\lambda_1}^{\lambda_2} \frac{d\lambda}{r_\perp^2 B_\lambda} \right)^{-1}. \quad (4.6)$$

If the toroidal field displays equatorial plane reflection symmetry, and the poloidal field displays equatorial symmetry,  $J(\Psi, \lambda_1, t) = J(\Psi, \lambda_2, t)$ , and there will be no magnetic twist injected into the core.

The procedure outlined above is efficient in tracing the crust-core evolution of the field, so long as the flux surfaces in the core are fixed in time. However, in our studies we would like to have the freedom to evolve the core poloidal field. In such situations, we found it more practical to use the second method outlined below.

### 4.3 Method II: Relaxation

The second method of enforcing hydromagnetic equilibrium, is to treat it as a relaxation problem. This method has the advantage of not requiring the integral in Equation (4.6) to be evaluated. Suppose there is a poloidal field threading the core. Hall drift in the crust will slowly displace the magnetic field lines in the azimuthal direction, and in response to this, the core field will adjust, quickly returning to hydromagnetic equilibrium. The evolution of the core field can be written

$$\frac{\partial \mathbf{B}_T}{\partial t} = \nabla \times (\mathbf{v}_T \times \mathbf{B}_p + \mathbf{v}_p \times \mathbf{B}_T), \quad (4.7)$$

with  $\mathbf{v}_T$  the toroidal (azimuthal) velocity which returns the core field to hydromagnetic equilibrium. The second term on the rhs is the advection of the toroidal field with the poloidal drift velocity  $\mathbf{v}_p$ , of flux surfaces. This term ensures that each poloidal field line maintains its own twist angle when the flux surfaces are evolving. For a given (fixed) poloidal field configuration, equilibrium is satisfied when

$$\frac{\partial \mathbf{B}_T}{\partial t} = 0 \quad (\text{equilibrium}). \quad (4.8)$$

Thus all that is required, is to choose a convenient form of  $\mathbf{v}_T$  which drives the field towards equilibrium faster than the other channels of evolution, such as Hall drift. First though, we write Equation (4.7) in a more convenient form. It can be shown that Equation (4.7) may be written as

$$\frac{\partial B_\phi}{\partial t} + \nabla_p \cdot (\mathbf{v}_p B_\phi) = \nabla_p \cdot (v_\phi \mathbf{B}_p), \quad (4.9)$$

where we have defined the poloidal differential operator

$$\nabla_p \equiv \left( \frac{\partial}{\partial r_\perp}, \frac{\partial}{\partial z} \right), \quad (4.10)$$

which acts in the 2D plane. Equation (4.9) is easily interpreted as a continuity equation, with the second term on the lhs representing the divergence of a transport flux of  $B_\phi$  due to drift of the poloidal field. The term on the rhs is a source term, which represents the injection or extraction of  $B_\phi$  (and magnetic twist) from the magnetic field lines which enter the crust. When using this method  $\mathbf{v}_p$  must be the same as the poloidal drift velocity of flux surfaces in the core. In this paper we only use this method for the case of fixed poloidal field lines in the core ( $\mathbf{v}_p = 0$ ), so that second term on the lhs of Equation (4.9) vanishes. All that remains is to choose a convenient form of  $v_\phi$  which will drive the field toward equilibrium. An obvious choice is to set

$$v_\phi \propto f_\phi = \frac{(\nabla \times \mathbf{B}_T) \times \mathbf{B}_p}{4\pi}, \quad (4.11)$$

so that when the field reaches hydromagnetic equilibrium, the velocity tends to zero. Note that this technique was also used by [Yang et al. \(1986\)](#). In our axisymmetric formalism, this is

$$v_\phi \propto (\nabla I \cdot \mathbf{B}_p) \nabla \phi. \quad (4.12)$$

We find however, that it is convenient to divide by poloidal field strength, so that the relaxation timescale is independent of this quantity. This gives the relaxation velocity

$$v_\phi = \frac{k}{|\mathbf{B}_p|} (\nabla I \cdot \hat{\mathbf{e}}_\lambda), \quad (4.13)$$

which obviously tends to zero as the field is driven toward equilibrium. For the case of static poloidal fields in the core ( $\mathbf{v}_p = 0$ ), Equation (4.9) becomes

$$\frac{\partial I}{\partial t} = r_\perp \nabla_p \cdot [k (\nabla I \cdot \hat{\mathbf{e}}_\lambda) \hat{\mathbf{e}}_\lambda], \quad (4.14)$$

which has the form of a modified diffusion equation. Solving the equations directly in the original form [Equation (4.7)] lead to short-wavelength numerical instabilities. Solving in the flux-conserving form [Equation (4.14)] removed the instabilities. Equation (4.14) with a large  $k$  ensures that the magnetic field in the core evolves through a sequence of MHD equilibria, and that these equilibria are stable.

In the more general case, poloidal magnetic field lines are not fixed in the core, but can drift with Ambipolar diffusion, or Jones drift. In this case one must ensure that  $\mathbf{v}_p$  matches the drift velocity of field lines in the crust at the crust-core interface. In the crust, the velocity of poloidal field lines is due to the Hall drift velocity  $\mathbf{v}_{\text{hall}}$ , and the Ohmic diffusion velocity  $\mathbf{v}_{\text{ohm}}$ ,

$$\mathbf{v}_p(r_c) = \mathbf{v}_{\text{hall}}(r_c) + \mathbf{v}_{\text{ohm}}(r_c), \quad (4.15)$$

where  $\mathbf{v}_{\text{hall}}$  is determined by Equation (3.8). We determine the Ohmic drift velocity of poloidal field lines by noting that the electric field determines  $\partial\mathbf{B}/\partial t = -c\nabla \times \mathbf{E}$ . If we assume that  $\mathbf{v}_p$  is perpendicular to  $\mathbf{B}$ , one may rewrite the evolution equation as  $\partial\mathbf{B}/\partial t = \nabla \times (\mathbf{v} \times \mathbf{B})$  with  $\mathbf{v}$  defined by  $\mathbf{E} = -\mathbf{v} \times \mathbf{B}/c$ . Using Ohm's law, for the case of poloidal fields this becomes

$$\frac{\mathbf{J}_T}{\sigma} = \frac{c}{4\pi\sigma} \nabla \times \mathbf{B}_p = -\frac{1}{c} \mathbf{v}_p \times \mathbf{B}_p, \quad (4.16)$$

with  $\mathbf{v}_p$  the poloidal velocity. Taking the cross product of both sides with  $\mathbf{B}_p$  allows us to solve for  $\mathbf{v}_p$ . This is the velocity at which poloidal magnetic field lines drift due to Ohmic diffusion, and we call it  $\mathbf{v}_{\text{ohm}}$ ,

$$\mathbf{v}_{\text{ohm}} = \frac{c^2}{4\pi\sigma} \frac{[(\nabla \times \mathbf{B}_p) \times \mathbf{B}_p]}{(\mathbf{B}_p \cdot \mathbf{B}_p)}. \quad (4.17)$$

When this velocity is inserted into an induction equation it is exactly equivalent to the Ohmic diffusion equation, so this is the correct Ohmic diffusion velocity. It is worth noting that we do not evolve the crustal field in our code with the velocity given by Equation (4.17). The crustal field is evolved with Ohmic diffusion in our code using Equation (3.21). The Equation (4.17) simply provides a boundary condition for the evolution of poloidal magnetic fields in the core.

We note here that a number of previous works fail to include the correct hydromagnetic equilibrium in the core, rendering their boundary condition on the crust-core interface unphysical. [Suvorov et al. \(2016\)](#) violate equatorial plane reflection symmetry, and therefore effectively must be injecting magnetic twist into the core within the timescale of their simulation. The simulations of [Elfritz et al. \(2016\)](#) include strong toroidal fields in the core, which in general do not satisfy  $f_\phi = 0$ . These stresses cannot be supported by the fluid, and therefore these simulations violate hydromagnetic equilibrium. This error in [Elfritz et al. \(2016\)](#) is due to their

lack of the terms which advect magnetic field by an azimuthal fluid motion; in other words, the background in which their flux tubes move is assumed to be static.

## 4.4 Numerical Details

Here we outline our numerical method used to implement hydromagnetic equilibrium through relaxation. While the method we developed in the previous section is applicable to scenarios with drifting poloidal magnetic field lines, so far we have only used it for the case when they are fixed. We begin with Equation (4.9) with  $\mathbf{v}_p = 0$ ,

$$\frac{\partial B_\phi}{\partial t} = \nabla_p \cdot (v_\phi \mathbf{B}_p) = \nabla_p \cdot [k(\nabla I \cdot \hat{\mathbf{e}}_\lambda) \hat{\mathbf{e}}_\lambda]. \quad (4.18)$$

We find it useful to rewrite this in a conservative form as

$$\frac{\partial}{\partial t} \left( \frac{I}{r \sin \theta} \right) = \frac{1}{r} \frac{\partial F_r}{\partial r} + \frac{1}{r} \frac{\partial F_\theta}{\partial \theta}, \quad (4.19)$$

where we have identified the fluxes

$$F_r = r \frac{k}{|\mathbf{B}_p|} (\nabla I \cdot \hat{\mathbf{e}}_\lambda) B_r, \quad (4.20)$$

$$F_\theta = \frac{k}{|\mathbf{B}_p|} (\nabla I \cdot \hat{\mathbf{e}}_\lambda) B_\theta. \quad (4.21)$$

In our numerical code we evaluate the functions  $F_r$  and  $F_\theta$  using the finite difference formula [Equation (3.41)]. The appropriate boundary condition at the crust-core interface is to enforce  $v_\phi(r_c) = 0$ , so that there are no hydromagnetic flows at the base of the crust, ie. the field lines are anchored at the base of the crust. This is a no-slip boundary condition. Since we chose the relaxation velocity

$$v_\phi = \frac{k}{|\mathbf{B}_p|} (\nabla I \cdot \hat{\mathbf{e}}_\lambda), \quad (4.22)$$

this is equivalent to enforcing

$$F_r(r_c) = 0, \quad (4.23)$$

and

$$F_\theta(r_c) = 0. \quad (4.24)$$

We can also see that since  $I(r, 0) = I(r, \pi) = 0$ ,  $\nabla I \cdot \hat{\mathbf{e}}_\lambda = 0$  along the poles. So we also set

$$F_r(r, 0) = 0, \quad (4.25)$$

$$F_\theta(r, \pi) = 0. \quad (4.26)$$

We can see due to axisymmetry that the function  $F_\theta$  is even about the poles, so we set ghost points according to

$$F_\theta^{j1-1} = F_\theta^{j1+1}, \quad (4.27)$$

$$F_\theta^{j2+1} = F_\theta^{j2-1}. \quad (4.28)$$

Ghost points are set for  $F_r$  at the crust-core interface such that

$$F_r^{ic+1} = F_r^{ic-1}. \quad (4.29)$$

We then use finite difference formula to evaluate the derivatives of  $F_r$  and  $F_\theta$  throughout the core [Equation (4.19)] using finite difference formulae [Equation (3.41)]. The crust and the core are time stepped in sequence so that the evolution is self consistent, ie. the crust is stepped in time which determines the value  $I_{\text{crust}}(r_c)$ . Then we set  $I_{\text{core}}(r_c) = I_{\text{crust}}(r_c)$ , and step the core. This process is repeated. We normalize the evolution equation in the code in the same way we normalize the Hall drift and Ohmic equations,

$$\frac{\partial B_\phi^{14}}{\partial t_{\text{yr}}} = 6.3 \times 10^{-7} \tilde{\nabla}_p \cdot [k_0 (\tilde{\nabla} (B_\phi^{14} r_6 \sin \theta) \cdot \hat{\mathbf{e}}_\lambda) \hat{\mathbf{e}}_\lambda]. \quad (4.30)$$

where  $B_\phi^{14} = B_\phi / 10^{14}$  G,  $t_{\text{yr}} = t / 3.15 \times 10^7$  s,  $\tilde{\nabla}$  is the del operator with lengths normalized to  $10^6$  cm,  $r_6 = r / 10^6$  cm and  $k_0 = k / 2 \times 10^{-8}$  cms $^{-1}$ . For more details of the numerical method we refer the reader to Appendix B.

## 4.5 Test Problems

In this section we present two test problems, to ensure that our relaxation scheme converges to hydromagnetic equilibrium, and that the correct symmetries are preserved.

Changing the twist angle of a field line in the core requires differential rotation of its two ends where it is attached to the crust. Equatorial symmetry of the magnetic field implies no differential rotation – the two ends must move with the same speed. The same fact is seen formally from the equations. For the case of equatorial symmetry, the net flux of twist into the core vanishes for each field line, as

$$J(\Psi, \lambda_2, t) - J(\Psi, \lambda_1, t) = 0, \quad (4.31)$$

(see Section 4). If the initial field has plane reflection symmetry about the equator, it will maintain this symmetry throughout the evolution. Then, by Equation (4.5), we see that

$$\partial_t I_{\text{core}}(\Psi, t) = 0 \quad (\text{if symmetric}), \quad (4.32)$$

for all time. In reality it is likely that young neutron stars will have some toroidal field in order to stabilize the poloidal field. However in some of our simulations we consider a number of initial fields which display equatorial reflection symmetry, and have purely poloidal fields in the core. In this special case the evolution of the core toroidal field is trivial - it remains zero according to hydromagnetic equilibrium.

First we consider a stationary core penetrating poloidal field, with some patches of toroidal field in the core which do not satisfy hydromagnetic equilibrium. That is

$$I \neq I(\Psi). \quad (4.33)$$

We use the same poloidal field as [Lasky & Melatos \(2013\)](#). In this simple test problem the crust field is fixed, and the only evolution is the hydromagnetic relaxation of the toroidal field in the core. For this particular choice of initial conditions, the toroidal field is symmetric about the equator, so we would expect the toroidal field to redistribute itself along the poloidal field lines and result in a positive, non-zero  $I$  along each poloidal field line.

We see in Figure 4.1 that after  $\sim 15$  kyr the toroidal field has been redistributed along the poloidal field lines [diffused by Equation (4.14)] to satisfy hydromagnetic equilibrium. That is,

$$I \longrightarrow I(\Psi), \quad (4.34)$$

which is also reflected in Figure 4.2. In Figure 4.3 we show the same setup, but for a toroidal field with equatorial reflection symmetry. That is, the toroidal field changes sign in opposite magnetic hemispheres. For this test we would expect the toroidal field to relax to  $I = 0$  along each poloidal field line, due to the symmetry shown in Equation (4.32). In Figures 4.3 and 4.4 we see that

$$I \longrightarrow I(\Psi) = 0, \quad (4.35)$$

as expected.

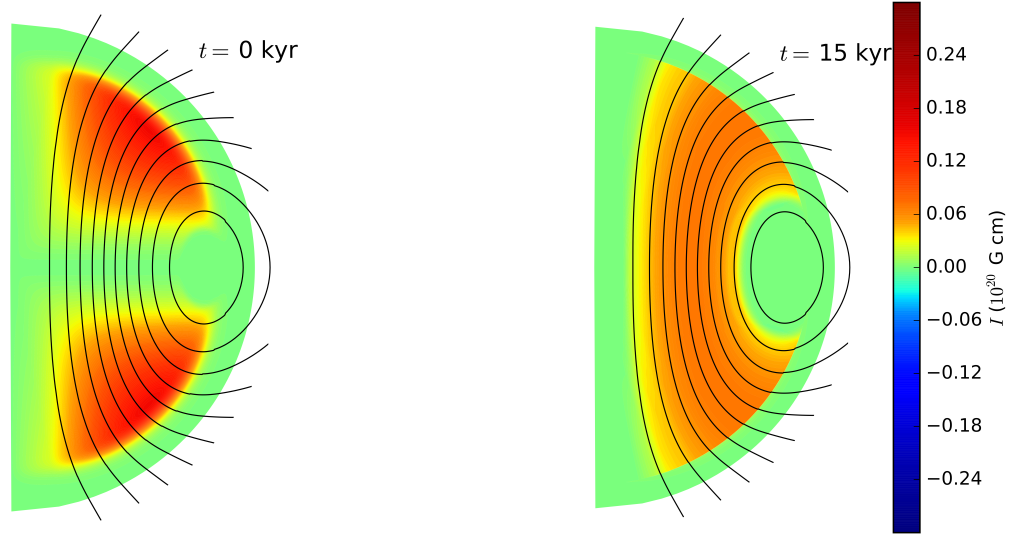


Figure 4.1: Snapshots of hydromagnetic relaxation of an initial field which is not in equilibrium, shown at  $t = 0$ , and 15 kyr. The black curves are 10 contour lines of the poloidal flux function  $\Psi$  (i.e. the poloidal magnetic field lines), equally spaced between  $\Psi = 0$  and the maximum value  $\Psi_{\max}$ , at  $t = 0$ . The toroidal field scalar function  $I$  is represented by the color scale, which varies logarithmically, with a linear region around zero.

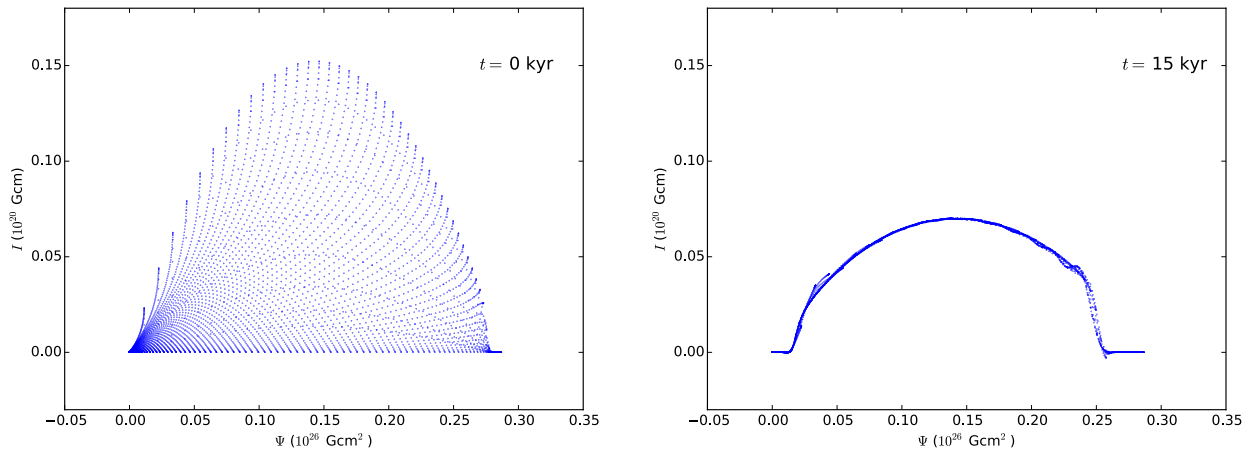


Figure 4.2: The values of  $I$ , and corresponding values of  $\Psi$  are plotted for the grid points in the core at  $t = 0$  kyr, and 15 kyr.

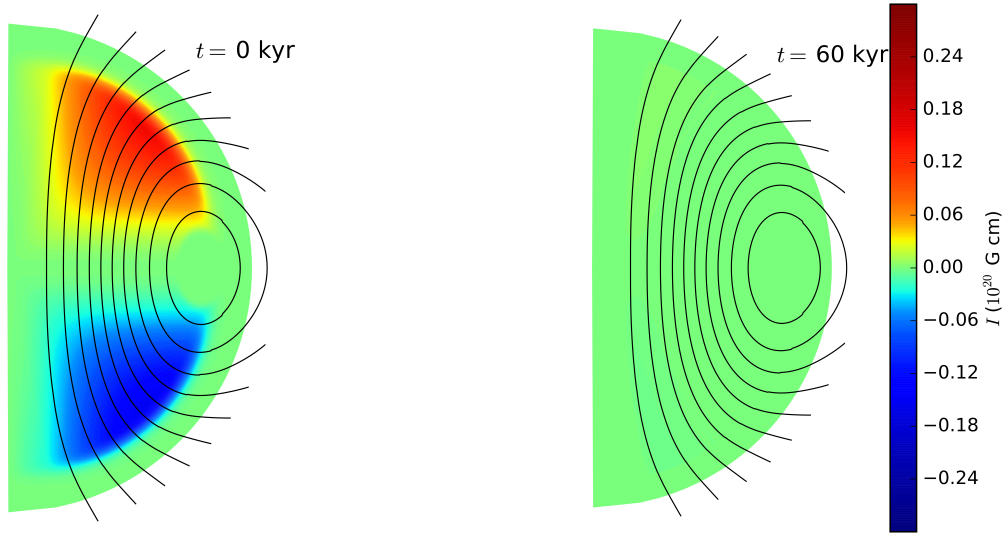


Figure 4.3: Snapshots of hydromagnetic relaxation of an initial field which is not in equilibrium, shown at  $t = 0$ , and 60 kyr. The black curves are 10 contour lines of the poloidal flux function  $\Psi$  (i.e. the poloidal magnetic field lines), equally spaced between  $\Psi = 0$  and the maximum value  $\Psi_{\max}$ , at  $t = 0$ . The toroidal field scalar function  $I$  is represented by the color scale, which varies logarithmically, with a linear region around zero.

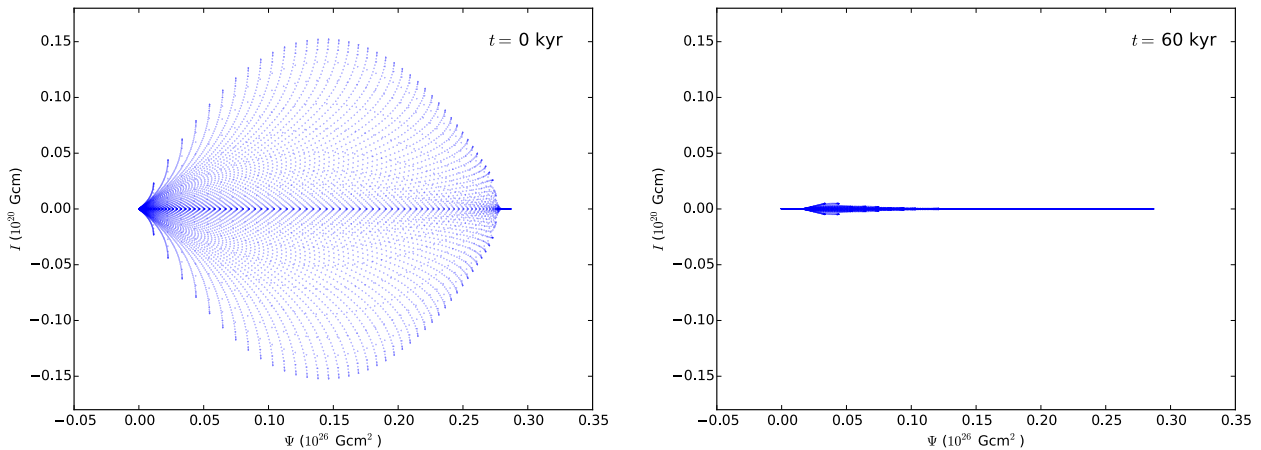


Figure 4.4: The values of  $I$ , and corresponding values of  $\Psi$  are plotted for the grid points in the core at  $t = 0$  kyr, and 60 kyr.

## 4.6 Results

First we consider Model A in which the effects of stellar spin-down, and Jones flux tube drift, and ambipolar diffusion are neglected (ie. the poloidal field is static in the core). The purpose of this section is to demonstrate clearly the hydromagnetic equilibrium described in Section 4. The drift of poloidal field lines in the core will be studied in Chapters 5 and 6.

Poloidal fields which violate equatorial plane reflection symmetry are chosen so that there is a non-zero flux of twist into the core,

$$J(\Psi, \lambda_2, t) \neq J(\Psi, \lambda_1, t), \quad (4.36)$$

and we may see evolution of the toroidal field in the core. With this in mind we choose the initial poloidal field in Figure 4.5 to violate equatorial reflection symmetry. In particular, we choose the initial field  $\Psi$  to be the same as [Lasky & Melatos \(2013\)](#), except we multiply by  $\sin\theta$  in the northern hemisphere to break equatorial symmetry. We enforce hydromagnetic equilibrium in Model A with the relaxation method outlined in Section 4.

The simulation shown in Figure 4.5 starts with a current sheet on the surface of the star in the northern hemisphere (see Figure 4.6). The current sheet shears poloidal field lines near the surface, and generates toroidal field with positive polarity in the northern hemisphere, and negative in the south. Hall drift in the crust slowly winds the core magnetic field in the azimuthal direction. At  $t = 200$  kyr there is a weak toroidal field in the core, and several patches of toroidal field in the crust with alternating polarity. After  $t \sim 600$  kyr the toroidal field reaches a steady state, with two patches near the equator in opposite hemispheres, which are damped by Ohmic diffusion from this point on. By this time the poloidal field has settled into the Hall attractor state, corresponding to constant electron angular drift velocity along poloidal field lines in the crust ( $\Omega_e = \Omega_e(\Psi)$ ). Hall drift in the crust continues to wind the core field in the azimuthal direction, though more slowly as Ohmic diffusion dissipates the crustal currents. At  $t = 2$  Myr the core supports a toroidal field of strength  $B \sim 10^{12}$  G, and similar in the crust. This confirms the Hall attractor of [Gourgouliatos & Cumming \(2014\)](#) for core penetrating B-fields, with the correct hydromagnetic equilibrium enforced.

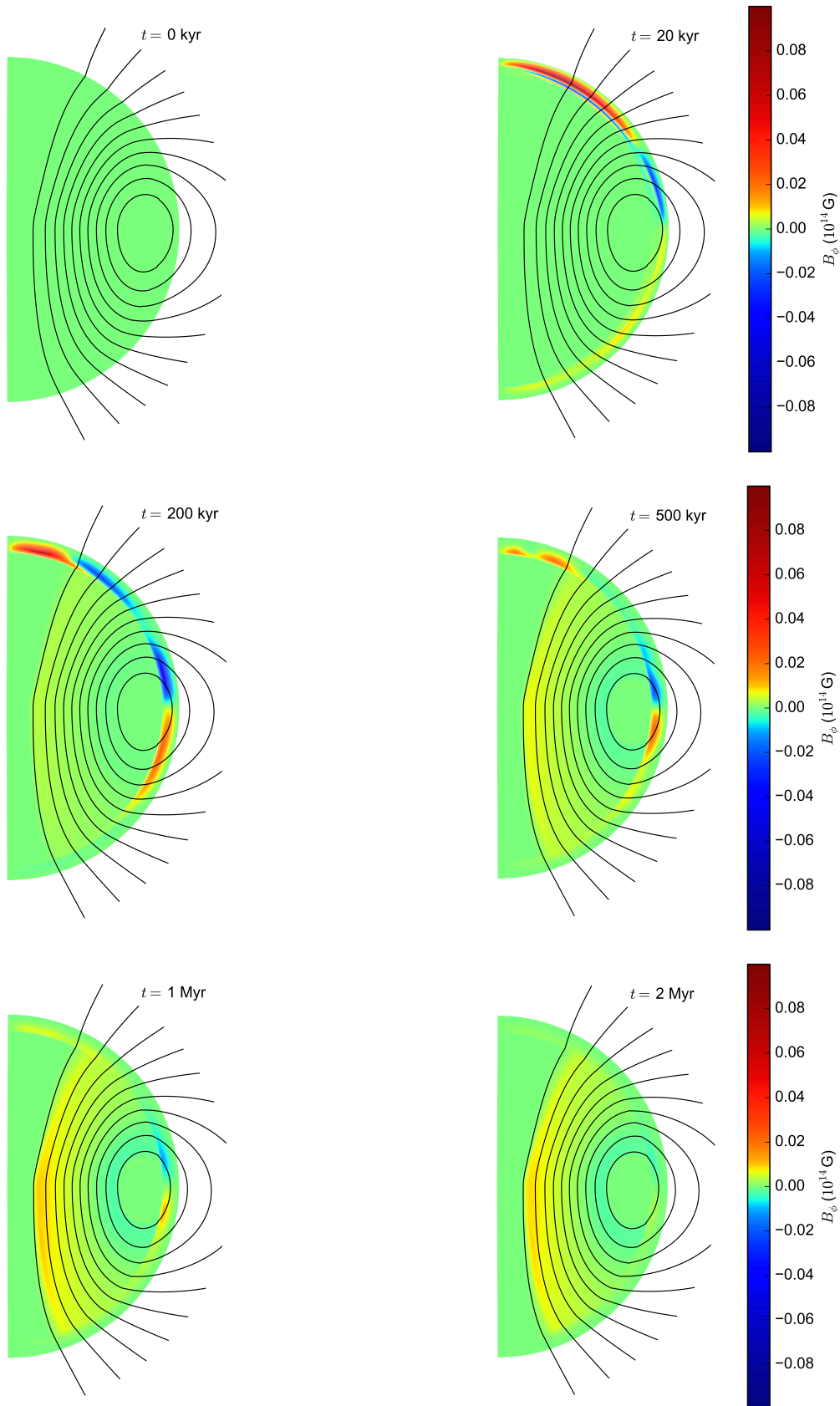


Figure 4.5: Snapshots of the magnetic field evolution for Model A (Table 1.1), shown at  $t = 0$ , 20 kyr, 200 kyr, 500 kyr, 1 Myr, and 2 Myr. The black curves are 10 contour lines of the poloidal flux function  $\Psi$  (i.e. the poloidal magnetic field lines), equally spaced between  $\Psi = 0$  and the maximum value  $\Psi_{\max}$ , at  $t = 0$ . The toroidal field is represented by the color scale, which varies logarithmically, with a linear region around zero.

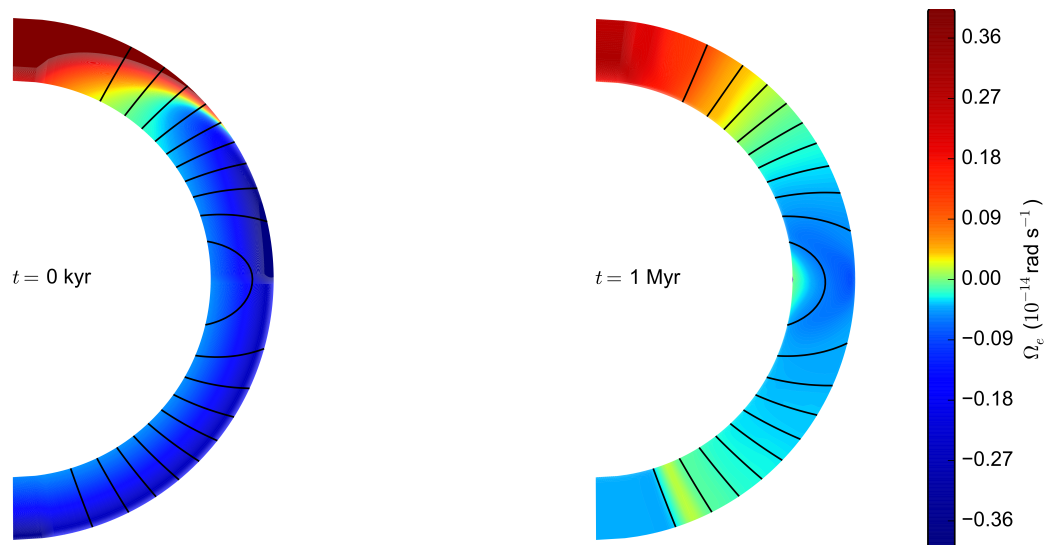


Figure 4.6: Snapshots of the evolution for Model A (Table 1.1), shown at  $t = 0$  kyr, and 1 Myr. The plotting scheme is the same as Figure 4.5 but here color shows  $\Omega_e$  (the angular velocity of the electron fluid), the result of Hall drift in the crust. The thickness of the crust has been magnified by a factor of 2.5.

## Monash University Declaration Chapter 5

### Declaration by candidate:

I declare that my contribution to the work in Chapter 5 that is submitted to the Monthly Notices of the Royal Astronomical Society as [Bransgrove et al. \(2017\)](#), involved the following:

The writing of the publication, developing the evolution equations, development of numerical methods including boundary conditions, development of the numerical code, running simulations, and all other work contained therein (that is not referenced otherwise).

Extent of contribution by candidate: 85%

Co-author names: Yuri Levin, Andrei Beloborodov

Nature of co-author's contribution: Developing the equations of motion, development of numerical methods including boundary conditions, and feedback during writing of the paper.

I have renumbered sections, equations and figures of the published paper in order to generate a consistent presentation within the thesis. The undersigned hereby certify that the above declaration correctly reflects the nature and extent of the student's and co-authors' contributions to this work.

Candidate Signature:

Date: June 29, 2017

Main Supervisor signature:



Date: June 29, 2017

## Chapter 5

# Flux Tube Drift in Type-II Superconducting Cores

Partially adapted from:

*Magnetic Field Evolution of Neutron Stars I: Basic formalism, numerical techniques, and first results*, Ashley Bransgrove, Yuri Levin, and Andrei Beloborodov, 2017, submitted for publication in MNRAS.

## 5.1 Jones Flux Tube Drift

### 5.1.1 Superconducting Magnetic Stress Tensor

When matter undergoes a phase transition to a type-II superconductor, the magnetic field is confined to an array of microscopic flux tubes, each surrounded by a super-current vortex. The tension and pressure of the spatially averaged magnetic field which threads the superconductor is no longer accurately described by the Maxwell stress tensor, and a special treatment is required. Here we show a derivation of the stress tensor for spatially averaged fields in a type-II superconductor. We follow closely the work of [Easson & Pethick \(1977\)](#), filling in the gaps in their calculation. We begin by considering the stresses of a magnetic field in some normal matter, which are given by the Maxwell stress tensor, with components

$$\sigma_{ij} = -\frac{B^2}{8\pi}\delta_{ij} + \frac{1}{4\pi}B_iB_j. \quad (5.1)$$

Each component of the stress tensor may be interpreted as a pressure which acts in the  $j$  direction, on a surface element with unit normal in the  $i$  direction. The first term is the isotropic part, which contributes to the pressure (diagonal components). The second term is the anisotropic contribution to the stress, which contributes to both the pressure, and the tension of the field (off diagonal components). For the case of a type-II superconductor, when the flux density is low ( $B \ll H_{c1}$ , the flux tubes are separated by distances much greater than the penetration depth of the magnetic field, ie.  $\lambda \ll d$ ) the magnetic field of a given flux tube cannot interact with the magnetic field of another such tube. Thus, intuitively we expect that the pressure term of the stress tensor will become negligible in this limit. Not so intuitively, the tension components of the stress can increase by factors which may be much greater than unity. This will become clear in the form of the superconducting magnetic stress tensor, which we now derive.

We follow the thermodynamic derivation of [Easson & Pethick \(1977\)](#). We consider a rectangular box, with side lengths  $L_x$ ,  $L_y$ , and  $L_z$ , filled with a highly conductive fluid, and permeated by flux tubes. We first assume that the system is in a thermodynamic equilibrium ( $dT = 0$ ), which is a good approximation so long as processes occurring there have timescales long compared to the time to reach thermal equilibrium. We work in cartesian coordinates, and consider the box to be sufficiently small that any variation of the matter density or density of flux tubes are negligible within it. So in this sense the box is homogeneous. In assuming that the fluid has high electrical conductivity, we are able to neglect any dissipative drift of the flux tubes relative to the fluid (i.e. the flux tubes are perfectly coupled to the fluid). The volume of the

box is  $V = L_x L_y L_z$ , and the free energy of the system is  $FV$ , where  $F$  is the Helmholtz free energy density which has natural thermodynamical variables temperature  $T$ , matter density  $\rho$ , and spatially averaged magnetic field  $B$ . The spatially averaged field may be written simply as  $B = n_\phi \phi_0$ , with  $n_\phi$  the average number of flux tubes per unit area in the  $x$ - $y$  plane. The free energy does not depend on our choice of the direction of  $B$ . Now consider the response of the free energy to small variations in the volume of the box. First we consider a small deformation of  $L_z$ . The variation in the Helmholtz free energy for such a process which retains thermal equilibrium is

$$d(FV) = \sigma_{zz} L_x L_y dL_z. \quad (5.2)$$

Squeezing the box in the  $z$  direction changes the density, but not the magnetic field, so we may write the variation of the free energy as

$$\sigma_{zz} = \frac{1}{L_x L_y} \frac{d(FV)}{dL_z} = F(\rho, B) - \rho \frac{dF}{d\rho}(\rho, B). \quad (5.3)$$

Now if we consider deforming the box in the  $x$  or  $y$  direction, the density will change as before. As the fluid is squeezed, the flux tubes move with the fluid. Since the total number of flux tubes remains constant, the number of flux tubes per unit area changes, and so too does  $B$ . So the  $xx$  and  $yy$  components may be written as

$$\sigma_{xx} = \sigma_{yy} = \sigma_{zz} - B \left( \frac{\partial F}{\partial B} \right)_{\rho, T} = \sigma_{zz} - \frac{BH}{4\pi}, \quad (5.4)$$

where we have identified

$$H = 4\pi \left( \frac{\partial F}{\partial B} \right)_{\rho, T}. \quad (5.5)$$

The components can be written in tensor notation as

$$\sigma_{ij} = \left( F - \rho \frac{\partial F}{\partial \rho} - \frac{\mathbf{H} \cdot \mathbf{B}}{4\pi} \right) \delta_{ij} + \frac{H_i B_j}{4\pi}. \quad (5.6)$$

There are contributions to the stress tensor (5.6) from both matter, and the magnetic field. To make clear the contribution from the field only, we write the Helmholtz free energy density as

$$F = F^{\text{matter}}(\rho) + F^{\text{mag}}(\rho, B). \quad (5.7)$$

Note that while the matter contribution depends only on the matter density, the magnetic part depends on both the field and the matter density. The magnetic part depends on matter because the density of the fluid can affect the pressure on the flux tubes, and hence, the magnetic energy contained in them. We can now write the magnetic part of the stress tensor as

$$\sigma_{ij}^{\text{mag}} = \left( F^{\text{mag}} - \rho \frac{\partial F^{\text{mag}}}{\partial \rho} - \frac{\mathbf{H} \cdot \mathbf{B}}{4\pi} \right) \delta_{ij} + \frac{H_i B_j}{4\pi}. \quad (5.8)$$

This tensor was derived in the most general case, where the magnetic flux density may be very high. For this reason the stress clearly has non-zero pressure components. But the pressure should become negligible in the limit  $\lambda \ll d$  ie.  $B \ll H_{c1}$ . We can write an expression for the Helmholtz free energy density by considering its Taylor expansion for small  $B$  (here small  $B$  means  $B \ll H_{c1}$ ),

$$F^{\text{mag}}(B) = F^{\text{mag}}(0) + B \left( \frac{\partial F^{\text{mag}}}{\partial B} \right)_{\rho, T} + \frac{1}{2!} B^2 \left( \frac{\partial^2 F^{\text{mag}}}{\partial B^2} \right)_{\rho, T} + \dots \simeq \frac{\mathbf{H} \cdot \mathbf{B}}{4\pi}. \quad (5.9)$$

We recognize second term in the isotropic part of (5.8) as a buoyancy contribution to the stress tensor, which we choose to neglect for the time being. This gives the final stress tensor as

$$\sigma_{ij}^{\text{mag}} = \frac{H_i B_j}{4\pi}, \quad (5.10)$$

which is pure tension. So our intuition was correct that for low flux density, the flux tubes do not feel mutual repulsion (pressure). It is sufficient to include only the tension part of the stress tensor for the spatially averaged field. Taking the divergence of this stress tensor gives the volume force of an array of flux tubes on the fluid in which they are immersed,

$$f_{B_i} = \frac{\partial \sigma_{ij}^{\text{mag}}}{\partial x_j} = \frac{B_j}{4\pi} \frac{\partial H_i}{\partial x_j}, \quad (5.11)$$

where we have used the fact that the divergence of  $\mathbf{B}$  is zero. In vector form this is

$$\mathbf{f}_B = \frac{1}{4\pi} (\mathbf{B} \cdot \nabla) \mathbf{H}_{c1}, \quad (5.12)$$

where we have approximated  $\mathbf{H} \approx \mathbf{H}_{c1}$ .

### 5.1.2 Forces on a Flux Tube

Cooling of neutron star cores below  $T_{\text{crit}} \approx 10^8 - 10^9$  K is accompanied by Cooper pairing of protons to form a  ${}^1S_0$  superfluid (Baym et al., 1969). The phase transition to superconductivity is associated with the quantization of magnetic flux on microscopic scales, with the quantum of flux  $\phi_0 = hc/2e$ . The flux is localised within proton supercurrent vortices, and drops off exponentially within  $\lambda \lesssim 10^{-11}$  cm. The mean intervortex spacing is  $d = 5 \times 10^{-10} B_{12}^{-1/2}$  cm, greater than the penetration depth, so that the flux tubes are very weakly interacting. ? realized that the anisotropic component of the magnetic stress tensor in type-II superconductors can be significantly larger than  $B^2/4\pi$ , which was later confirmed by Easson & Pethick (1977). Additionally, the transition to proton superconductivity dramatically alters the transport of magnetic flux. In this section we consider the forces acting on the fluid surrounding a moving isolated flux tube. In this section we neglect the coupling of proton and neutron mass currents,

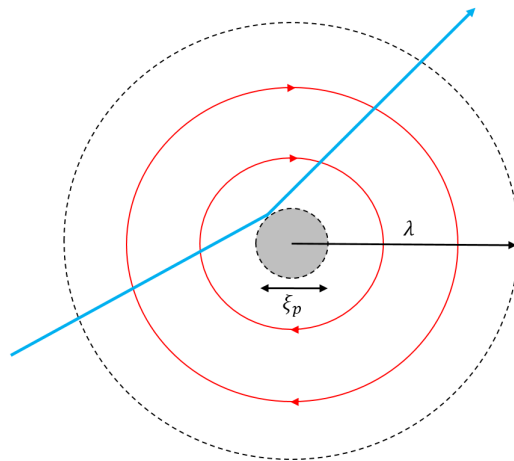


Figure 5.1: Cross section of a flux tube: Red lines show streamlines of superconducting protons, with the inner and outer dotted black lines representing the penetration coherence length  $\xi_p$ , and the penetration depth  $\lambda$  respectively. The path of a typical electron in the vicinity of a flux tube is shown in blue.

and focus only on the force experienced by the protons and electrons in the immediate vicinity ( $\lesssim \lambda$ ) of a flux tube.

There has been much controversy in the literature on the topic of flux tube drift in neutron stars [eg. Jones (2006), Glampedakis et al. (2011), Graber et al. (2015), Elfritz et al. (2016), Dommès & Gusakov (2017), Passamonti et al. (2017)]. Further work is required to clarify the controversy, which is outside the scope of this thesis. In this section we present the prescription of Jones (2006) (J2006 from now on) as clearly as possible, so that the reader may understand this particular model of flux tube drift.

We consider the forces a microscopic flux tube moving at velocity  $\mathbf{v}_L$  exerts on the proton-electron liquid in the neutron star core. First we study the force on the proton liquid in the immediate vicinity of a single flux tube ( $\lesssim \lambda$ , see Figure 5.1). Then we consider the force a flux tube exerts on the electrons in the immediate vicinity of a flux tube ( $\lesssim \lambda$ ). We then average over these microscopic forces, to obtain the macroscopic force density exerted on the proton-electron liquid by a lattice of flux tubes.

The total force acting on the proton liquid in the immediate vicinity of a single flux tube (the force on the flux tube) is calculated as a sum of electromagnetic forces and fluid pressures. We refer the reader to Nozières & Vinen (1966) for a detailed calculation. Jones (1991) states that

the superfluid proton velocity in the rest frame of the vortex lattice is given by  $\mathbf{v}_p = \tilde{\mathbf{v}}_p + \mathbf{v}_{p0} - \mathbf{v}_L$ . Here  $\tilde{\mathbf{v}}_p$  is the microscopic circulation around the flux tube, and  $\mathbf{v}_{p0}$  is a large scale drift (spatially uniform on microscopic scales). Jones (1991) gives the force per unit length on the proton liquid as

$$\mathbf{F}^p = \frac{e}{m_p c} \rho_p (\mathbf{v}_{p0} - \mathbf{v}_L) \times \boldsymbol{\phi}_0, \quad (5.13)$$

which is the Magnus force. Here  $\rho_p$  is the mass density of superfluid protons, and  $\boldsymbol{\phi}_0 = \phi_0 \hat{\mathbf{e}}_\lambda$ , with  $\hat{\mathbf{e}}_\lambda$  a unit vector directed along the flux tube. This is a well known result which has been shown by many authors including Nozières & Vinen (1966), Parks (1969), Jones (1987), Jones (1991), Glampedakis et al. (2011), Graber et al. (2015). There appears to be agreement on this force in the literature. The corresponding spatially averaged force density is given by J2006 as

$$\mathbf{f}^p = \frac{n_p e}{c} (\mathbf{v}_{p0} - \mathbf{v}_L) \times \mathbf{B}, \quad (5.14)$$

with  $\mathbf{B} = n_\phi \boldsymbol{\phi}_0$  the spatially averaged magnetic field. Here  $n_\phi$  is the number of flux tubes per unit area.

In the core, electron orbits are irregular polyhedra, with vertices coinciding with the microscopic magnetic flux density  $\tilde{\mathbf{B}}$  (see Figure 5.1) J2006. The intervortex spacing  $d$  is much greater than the penetration depth  $\lambda$ , so that the electron paths are straight in between scatterings. Jones (1987) states that the scattering angle of electrons at each vertex is small, so that the electron orbits are effectively circular with orbit size given by the average flux density,  $r = ck_F/eB$ . The Lorentz force deflects electrons from the microscopic flux density  $\tilde{\mathbf{B}}$ . Jones (1991) gives this force per unit length as

$$\mathbf{F}_L^e = -\frac{n_e e}{c} \int d^2r (\mathbf{v}_e - \mathbf{v}_L) \times \tilde{\mathbf{B}}, \quad (5.15)$$

with the integral over the cross section of a single flux tube. The corresponding spatially averaged Lorentz force density on the electrons is given by J2006 as

$$\mathbf{f}_L^e = -\frac{n_e e}{c} (\mathbf{v}_e - \mathbf{v}_L) \times \mathbf{B}. \quad (5.16)$$

Jones (1987) shows that there is a drag force exerted on electrons in the immediate vicinity of a flux tube by quasi-particles and normal protons localized within the flux tube core, and that this force is proportional to the relative velocity between the flux tube and the electron liquid. J2006 provides a microphysical derivation of the drag coefficient using the electron Boltzmann equation. J2006 gives the spatially averaged drag force density on the electrons as

$$\mathbf{f}_D^e = \frac{(n_e e)^2}{\tilde{\sigma}} (\mathbf{v}_L - \mathbf{v}_e), \quad (5.17)$$

with  $(n_e e)^2 / \tilde{\sigma}$  a drag coefficient, and  $\tilde{\sigma}$  an effective conductivity. To summarize, the total force density an array of flux tubes exerts on the electrons is the sum of the Lorentz and drag forces,

$$\mathbf{f}^e = \mathbf{f}_L^e + \mathbf{f}_D^e = -\frac{n_e e}{c}(\mathbf{v}_e - \mathbf{v}_L) \times \mathbf{B} + \frac{(n_e e)^2}{\tilde{\sigma}}(\mathbf{v}_L - \mathbf{v}_e), \quad (5.18)$$

while the total force density exerted on the proton liquid is the Magnus force

$$\mathbf{f}^p = \frac{n_p e}{c}(\mathbf{v}_{p0} - \mathbf{v}_L) \times \mathbf{B}. \quad (5.19)$$

The total force an array of flux tubes drifting with velocity  $\mathbf{v}_L$  exerts on the combined proton-electron fluid is

$$\mathbf{f}^{pe} = \mathbf{f}^p + \mathbf{f}^e = -\frac{n_e e}{c}(\mathbf{v}_e - \mathbf{v}_L) \times \mathbf{B} + \frac{(n_e e)^2}{\tilde{\sigma}}(\mathbf{v}_L - \mathbf{v}_e) + \frac{n_p e}{c}(\mathbf{v}_{p0} - \mathbf{v}_L) \times \mathbf{B}. \quad (5.20)$$

But the force flux tubes exert on the fluid is also given by the divergence of the superconducting stress tensor by [Easson & Pethick \(1977\)](#). Therefore, we can equate  $\mathbf{f}_B = \mathbf{f}^{pe}$ . This is similar to equating the Lorentz force, to the force on the proton-electron liquid, as is done with ambipolar diffusion ([Goldreich & Reisenegger, 1992](#)). This yields the force balance

$$\mathbf{f}_B = -\frac{n_e e}{c}(\mathbf{v}_e - \mathbf{v}_L) \times \mathbf{B} + \frac{(n_e e)^2}{\tilde{\sigma}}(\mathbf{v}_L - \mathbf{v}_e) + \frac{n_p e}{c}(\mathbf{v}_{p0} - \mathbf{v}_L) \times \mathbf{B}. \quad (5.21)$$

This force balance has some differences to that of [Glampedakis et al. \(2011\)](#), [Graber et al. \(2015\)](#), and [Elfritz et al. \(2016\)](#) which we list below.

1. J2006 has equated the force  $\mathbf{f}_B$  to the sum of forces acting on the proton-electron liquid in the vicinity of the flux tube  $\mathbf{f}^{pe}$ . Conversely, [Glampedakis et al. \(2011\)](#) and [Graber et al. \(2015\)](#) have summed all of the forces and set the sum equal to zero. This leads to a difference in sign in the magnus force.
2. J2006, [Glampedakis et al. \(2011\)](#), and [Graber et al. \(2015\)](#) all agree on the form of the drag force

$$\mathbf{f}_D \propto (\mathbf{v}_L - \mathbf{v}_e)$$

J2006 attributes this force to electron scattering off quasi particles and normal protons localised in the flux tube cores. Conversely [Glampedakis et al. \(2011\)](#) and [Graber et al. \(2015\)](#) attribute this force to electrons scattering off the microscopic flux density  $\tilde{\mathbf{B}}$  localised in the flux tube. J2006 has accounted for magnetic scattering with the Lorentz force  $\mathbf{f}_L^e$ .

3. [Glampedakis et al. \(2011\)](#) and [Graber et al. \(2015\)](#) have an additional term  $\mathbf{f}_{\text{em}}$ , which is attributed to the force of flux tubes on macroscopic electromagnetic currents. Its form is

$$\mathbf{f}_{\text{em}} \propto (\mathbf{v}_e - \mathbf{v}_p) \times \tilde{\mathbf{B}}. \quad (5.22)$$

4. In its most basic form, the drag force of J2006 and [Alpar et al. \(1984\)](#) reduces to

$$\mathbf{f}_D = \frac{\rho_e}{\tau_e} (\mathbf{v}_e - \mathbf{v}_L), \quad (5.23)$$

with  $\rho_e$  the mass density of electrons, and  $\tau_e$  the electron-flux tube relaxation timescale. However the drag force of [Glampedakis et al. \(2011\)](#), [Graber et al. \(2015\)](#), and [Elfriz et al. \(2016\)](#) reduces to

$$\mathbf{f}_D = \frac{\rho_p}{\tau_e} (\mathbf{v}_e - \mathbf{v}_L), \quad (5.24)$$

with  $\rho_p$  the proton density, which is almost four orders of magnitude larger than the electron mass density.

5. [Elfriz et al. \(2016\)](#) identify the magnus force per unit length as depending on the relative velocity between the flux tubes and the electrons, rather than the flux tubes and the protons, but still use the proton mass density.

It is important that these differences are resolved, since this force balance determines the equation of motion for the magnetic field. However, clarifying each of the above issues will require careful consideration, which is outside the scope of this thesis. Despite the lack of theoretical consensus on the dynamics of flux tubes, we take the prescription of J2006, and proceed, since the time scales produce interesting effects which are well modeled by our numerical code.

### 5.1.3 Current Screening Condition

There is a peculiarity in the system described above, in that magnetic fields (and therefore the currents which generate them) are forbidden from existing inside a superconductor. However, in this case, relative motion between superfluid protons and normal electrons can cause macroscopic currents to flow, and hence generate magnetic fields. Evidently if the superconducting phase is to be preserved, these currents must somehow be screened. A screening condition has been proposed by [Jones \(1991\)](#). We present here our own argument, which leads to the same screening condition. Following the convention set by [Alpar et al. \(1984\)](#), we label any magnetic field which may exist in the bulk of the fluid (in between flux tubes)  $\mathbf{b}_L$ , the London field. The

universality of Maxwell's equations means that they must hold true inside a superconductor. Therefore the London field satisfies Amperes law for the total current,

$$\mathbf{J}^e + \mathbf{J}^p = \frac{c}{4\pi} \nabla \times \mathbf{b}_L. \quad (5.25)$$

However there is an additional constraint equation. This can be realized by first considering the velocity of superfluid protons, which is given by the expression

$$\mathbf{v}_p = \frac{\hbar}{2m_p} \nabla \chi - \frac{e}{m_p c} \mathbf{A} \quad (5.26)$$

[see eg. Lifshitz & Pitaevskii (1980)], where  $\chi$  is a complex phase parameter, and  $\mathbf{A}$  is the vector potential with  $\mathbf{b}_L = \nabla \times \mathbf{A}$ . It is then easy to see that the proton supercurrent must satisfy the constraint

$$\nabla \times (\lambda^2 \mathbf{J}^p) = -\frac{c}{4\pi} \mathbf{b}_L, \quad (5.27)$$

which is known as the London equation, with

$$\lambda^2 = \frac{m^2 c^2}{4\pi e^2 \rho_p} \quad (5.28)$$

the penetration depth. The constraint Equation (5.27) must be obeyed along with all of Maxwell's equations in the superconductor. Now we solve (5.27) for  $\mathbf{b}_L$ , and insert it in Equation (5.25), to obtain

$$\mathbf{J}^e + \mathbf{J}^p = -\nabla \times \nabla \times (\lambda^2 \mathbf{J}^p). \quad (5.29)$$

In order to proceed we resolve  $\mathbf{J}^e$  and  $\mathbf{J}^p$  into solenoidal (divergence-free), and irrotational (curl-free) parts,  $\mathbf{J}_{\text{sol}}^e$  and  $\mathbf{J}_{\text{sol}}^p$ , and  $\mathbf{J}_{\text{ir}}^e$  and  $\mathbf{J}_{\text{ir}}^p$ . Note that the rhs of (5.29) is always solenoidal. The solenoidal and irrotational components of (5.29) can then be written as

$$\mathbf{J}_{\text{ir}}^e + \mathbf{J}_{\text{ir}}^p = 0, \quad (5.30)$$

$$\mathbf{J}_{\text{sol}}^e + \mathbf{J}_{\text{sol}}^p = -\nabla \times \nabla \times (\lambda^2 \mathbf{J}_{\text{ir}}^p + \lambda^2 \mathbf{J}_{\text{sol}}^p). \quad (5.31)$$

The irrotational part of the current is perfectly screened, however the behavior of the solenoidal equation is not yet apparent. To proceed we must assume that the penetration depth has negligible spatial dependence, so that it can be taken outside the differential operator. Then equation (5.31) becomes

$$\mathbf{J}_{\text{sol}}^e + \mathbf{J}_{\text{sol}}^p = -\lambda^2 \nabla \times \nabla \times \mathbf{J}_{\text{sol}}^p, \quad (5.32)$$

which reduces to the following equation after the use of a vector identity,

$$\mathbf{J}_{\text{sol}}^p - \lambda^2 \nabla^2 \mathbf{J}_{\text{sol}}^p = -\mathbf{J}_{\text{sol}}^e. \quad (5.33)$$

This is the inhomogeneous vector Helmholtz equation, with the electron current density acting as a source term. To understand this equation, we consider (5.33) in cartesian coordinates, with a current density which only depends on the x coordinate. The solenoidal component must satisfy

$$\nabla \cdot \mathbf{J}_{\text{sol}}^{\text{p}} = 0, \quad (5.34)$$

which implies that  $J_x^{\text{p}} = \text{const}$ . Here  $J_x^{\text{p}}$ ,  $J_y^{\text{p}}$ , and  $J_z^{\text{p}}$  refer to the x, y, and z components of  $\mathbf{J}_{\text{sol}}^{\text{p}}$ . It is instructive to consider how the Equation (5.33) responds to a given Fourier mode of proton current density. We write the spatial dependence of the y and z components as,

$$J_y^{\text{p}} = J_n^y e^{ik_n x}, \quad (5.35)$$

$$J_z^{\text{p}} = J_n^z e^{ik_n x}. \quad (5.36)$$

Inserting  $J_x^{\text{p}} = \text{const}$  into Equation (5.33) results in

$$J_x^{\text{e}} + J_x^{\text{p}} = 0. \quad (5.37)$$

The y-component of  $\mathbf{J}_{\text{sol}}^{\text{p}}$  satisfies

$$J_y^{\text{p}} = -\frac{J_y^{\text{e}}}{1 + \lambda^2 k_n^2}. \quad (5.38)$$

The penetration depth is estimated as  $\lambda \sim 10^{-11}$  cm (Jones, 1991), and we envisage a large scale (within a few orders of magnitude of  $k_n^{-1} \sim r_* \sim 10^6$  cm) proton supercurrent induced as a result of global flux tube drift. Therefore the quantity  $\lambda k_n$  is always many orders of magnitude smaller than unity, and the following equality

$$J_y^{\text{p}} + J_y^{\text{e}} = 0, \quad (5.39)$$

can be regarded as exact. The same is true of the z component. Thus, we can see that

$$\mathbf{J}_{\text{sol}}^{\text{e}} + \mathbf{J}_{\text{sol}}^{\text{p}} = 0, \quad (5.40)$$

provided  $\lambda k_n \ll 1$ . Combining with (5.30), we see that

$$\mathbf{J}^{\text{e}} + \mathbf{J}^{\text{p}} = 0, \quad (5.41)$$

so that all large scale charged currents are screened inside the superconductor. In the case of charge neutrality ( $n_e = n_p$ ), this implies co-motion of electrons and protons on large scales

$$\mathbf{v}_e = \mathbf{v}_p. \quad (5.42)$$

This is an amazing fact which is a simple consequence of the London constraint on Maxwell's equations, and is analogous to the Meissner screening condition in simpler single fluid superconductors. Jones (1991) arrives at the same result, by assuming that the proton supercurrent

varies on large scales. The derivation of Jones (1991) also requires an assumption about the spatial dependence of the phase parameter  $\chi$ . We make no assumptions about  $\chi$ , and also show that irrotational currents are perfectly screened at all scales. In our opinion the physical mechanism behind this screening condition is not well understood. It is not yet clear to us which field enforces the co-motion of protons and electrons, and how it is generated. This requires further investigation which is outside the scope of this work. A consequence of this screening condition, is that the London field is negligibly weak in studies of large scale electrodynamics in neutron star cores. Note that Glampedakis et al. (2011) and Graber et al. (2015) identify the lhs of Equation (5.27) with the rigid rotation of the star itself, and then incorrectly estimate the strength of the London field based on typical neutron star spin frequencies. They also reach the result that the London field is weak, however the screening condition as we have shown above, and as Jones (1991) has shown is a more general statement which is valid for arbitrary large scale currents. Passamonti et al. (2017) states that the london field is weak, and this implies protons and electrons are co-moving. The correct statement is that protons and electrons are co-moving due to the London constraint on electrodynamics, and this implies the london field is weak.

#### 5.1.4 Electric Field of a Moving Flux Tube

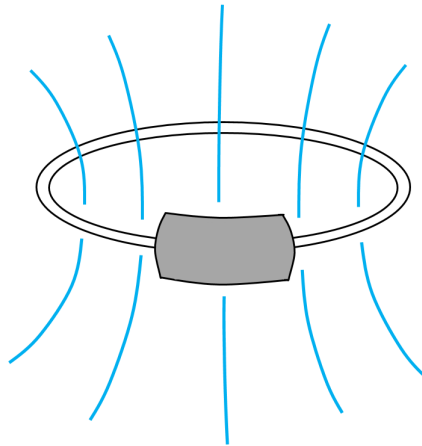


Figure 5.2: A type-I superconducting ring (white), with a type-II superconducting region (grey). The ring carries a current which supports the magnetic field threading it (blue).

The evolution of the spatially averaged magnetic field ( $\mathbf{B} = \langle \tilde{\mathbf{B}} \rangle$  with  $\tilde{\mathbf{B}}$  the microscopic magnetic flux density) in a type-II superconductor is determined by Faraday's law,

$$\frac{\partial \mathbf{B}}{\partial t} = -c \nabla \times \mathbf{E}, \quad (5.43)$$

with  $\mathbf{E} = \langle \tilde{\mathbf{E}} \rangle$  the spatially averaged electric field. The form of the electric field  $\mathbf{E}$  associated with the drift of flux tubes has been discussed by several authors, including [Nozières & Vinen \(1966\)](#), [Parks \(1969\)](#), and [J2006](#). Here we outline the thought experiment used by [Parks \(1969\)](#). It is useful to consider a superconducting ring as in Figure 5.2. The ring is a type-I superconductor, except for a part of the ring which has been replaced by a type-II superconductor. A magnetic field is supported by a supercurrent which flows in the ring. In this thought experiment, the magnetic field can leak out of the ring, but only through the type-II region — it is forbidden from passing through the type-I part of the loop. As the magnetic field leaks through the type-II region, the magnetic flux contained in the loop decreases at the rate

$$\frac{\partial \Phi}{\partial t} = \oint_{\gamma} \frac{\partial \mathbf{A}}{\partial t} \cdot d\mathbf{l} = \oint_{\gamma} \mathbf{v}_L \times \mathbf{B} \cdot d\mathbf{l}, \quad (5.44)$$

with  $\Phi$  the magnetic flux,  $\mathbf{A}$  the magnetic vector potential,  $\mathbf{v}_L$  the velocity of flux tubes passing through the type-II superconductor, and  $\gamma$  the contour of integration which passes through the interior of the loop shown in Figure 5.2. In the type-I part of the loop  $\mathbf{E} = 0$ , but in the type-II region the electric field satisfies Faraday's law,

$$\mathbf{E} = -\nabla V - \frac{1}{c} \frac{\partial \mathbf{A}}{\partial t}, \quad (5.45)$$

with  $V$  a scalar potential. Rearranging this for  $\partial \mathbf{A} / \partial t$ , and inserting into Equation (5.44) gives

$$\oint_{\gamma} (\nabla V + \mathbf{E}) \cdot d\mathbf{l} = -\frac{1}{c} \oint_{\gamma} \mathbf{v}_L \times \mathbf{B} \cdot d\mathbf{l}. \quad (5.46)$$

Assuming  $V$  is continuous throughout the loop, the line integral of  $\nabla V$  vanishes according to the fundamental theorem of line integrals. It is clear that the only contribution to the remaining line integrals is from the type-II region,

$$\int_{\gamma_2} \mathbf{E} \cdot d\mathbf{l} = -\frac{1}{c} \int_{\gamma_2} \mathbf{v}_L \times \mathbf{B} \cdot d\mathbf{l}, \quad (5.47)$$

where  $\gamma_2$  is the part of the contour which passes through the type-II superconductor. From this expression we can write the electric field in differential form as

$$\mathbf{E} = -\frac{1}{c} \mathbf{v}_L \times \mathbf{B}. \quad (5.48)$$

This is the electric field associated with the motion of flux tubes at velocity  $\mathbf{v}_L$ . The evolution of the magnetic field is then

$$\frac{\partial \mathbf{B}}{\partial t} = \nabla \times (\mathbf{v}_L \times \mathbf{B}). \quad (5.49)$$

Other authors have preferred to use Euler equations for the spatially averaged flux tube array and multi-fluid system to determine the electric field which governs the evolution of the magnetic

field in Equation (5.43). We however, prefer a simpler approach, which is based on the fact that the magnetic field must be advected at the velocity of the flux tubes  $\mathbf{v}_L$ . We hope that in using this approach we have avoided the presence of unphysical terms in our evolution equation, which advect the magnetic field at a velocity different to  $\mathbf{v}_L$ . The form of Equation (5.49) is supported by [Konenkov & Geppert \(2001\)](#), and [Dommes & Gusakov \(2017\)](#). In order to close the system, we use a force balance on the liquid [provided by J2006] to determine the velocity  $\mathbf{v}_L$ .

### 5.1.5 Large Scale Flux Tube Drift

We now return to the force balance of J2006, in order to determine the velocity of flux tubes  $\mathbf{v}_L$ . Here we equate the force  $\mathbf{f}_B$  to the force of the flux tubes on the proton-electron liquid,

$$\mathbf{f}_B - \frac{(n_e e)^2}{\tilde{\sigma}} (\mathbf{v}_L - \mathbf{v}_e) - \frac{n_e e}{c} (\mathbf{v}_L - \mathbf{v}_e) \times \mathbf{B} - \frac{n_p e}{c} (\mathbf{v}_{p0} - \mathbf{v}_L) \times \mathbf{B} = 0. \quad (5.50)$$

The screening condition described in Section 5.41 is

$$\mathbf{J}^e + \mathbf{J}^p = 0, \quad (5.51)$$

which implies  $\mathbf{v}_{p0} = \mathbf{v}_e$  in the case of charge neutrality ( $n_e = n_p$ ). Enforcing this screening condition on the force balance Equation (5.50) leads to the perfect cancellation of the Magnus force on the proton fluid, and the Lorentz force on the electron fluid. The remaining force balance can then be solved for the velocity of the flux tube lattice,

$$\mathbf{v}_L = \mathbf{v}_e + \frac{\tilde{\sigma}}{n_e^2 e^2} \mathbf{f}_B, \quad (5.52)$$

which is the velocity of the normal electron liquid, plus the viscous slippage of the flux tube lattice through the normal liquid, driven by the tension force  $\mathbf{f}_B$ . Intuitively this velocity makes sense — if the flux tubes are to drift any faster than the bulk fluid velocity, it must be accompanied by dissipation at the rate

$$\dot{u} = \mathbf{f}_B \cdot \mathbf{v}_J \quad (5.53)$$

Inserting this expression for the flux tube velocity into the electric field Equation (5.48) yields the following spatially averaged electric field

$$\mathbf{E} = -\frac{1}{c} \mathbf{v}_e \times \mathbf{B} - \frac{1}{c} \frac{\tilde{\sigma}}{n_e^2 e^2} \mathbf{f}_B \times \mathbf{B} \quad (5.54)$$

Inserting this into Equation (5.43), which yields the following equation for the evolution of the magnetic field

$$\frac{\partial \mathbf{B}}{\partial t} = \nabla \times (\mathbf{v}_e \times \mathbf{B}) + \nabla \times \left[ \frac{\tilde{\sigma}}{n_e^2 e^2} \frac{(\mathbf{B} \cdot \nabla) \mathbf{H}_{c1}}{4\pi} \times \mathbf{B} \right]. \quad (5.55)$$

The second term is of particular interest. It describes the dissipative drift of flux tubes through the core, and is analogous (mathematically) to the ambipolar diffusion of [Goldreich & Reisenegger \(1992\)](#). Here though, the classical Lorentz force has been replaced by the superconducting analogue, and the drag on the field is due to a fundamentally different physical mechanism.

There has been particular interest in the literature in the presence of a Hall-like term in the evolution equation for magnetic fields in a type-II superconductor [eg. [Graber et al. \(2015\)](#), [Elfritz et al. \(2016\)](#), [Dommes & Gusakov \(2017\)](#), [Passamonti et al. \(2017\)](#)]. The term we refer to is present in the evolution equation of the magnetic field as

$$\frac{\partial \mathbf{B}}{\partial t} = \nabla \times \left( \frac{k}{n_c e} \mathbf{f}_B \right), \quad (5.56)$$

with  $n_c$  the density of charge carriers,  $k$  a coefficient which has been the subject of recent debate, and  $\mathbf{f}_B$  the superconducting analogue of the Lorentz force  $\mathbf{j} \times \mathbf{B}/c$  [see [Passamonti et al. \(2017\)](#) for a detailed discussion of this term and the coefficient we call  $k$ ]. It is our view that this Hall like term leads to unphysical evolution of the core magnetic field. Our reasoning is as follows. Consider a purely poloidal, axisymmetric initial magnetic field, which satisfies hydromagnetic equilibrium ( $f_\phi = 0$ ). The Hall-like term in Equation (5.56) will slowly shear the poloidal field lines in the azimuthal direction, generating non-zero  $f_\phi$ . The fluid cannot support non-zero  $f_\phi$ , so a hydromagnetic flow ensues, quickly returning the field to a state of  $f_\phi = 0$ , and in this case  $B_\phi = 0$ . That is, any stress which is generated by Equation (5.56), is removed even faster by hydromagnetic flows, to return the field to  $f_\phi = 0$ . There is no net effect. Therefore this term is not relevant for magnetic field evolution in a liquid which is hydromagnetically stable, and the term should be discarded from the evolution equation. It is for the same reason that a non-superconducting core cannot evolve with classical Hall drift of the magnetic field — the fluid cannot support stresses generated by this effect. Hall drift can occur in the crust only because the solid has restoring forces which can support magnetic stresses the Hall effect generates.

## 5.2 Axisymmetric Equations

In axisymmetry the evolution of the toroidal magnetic field is governed by hydromagnetic equilibrium (see Chapter 4). Therefore, in our studies of flux tube drift, we need only specify the evolution of the poloidal field due to this effect, which we write as

$$\frac{\partial \mathbf{B}_p}{\partial t} = \nabla \times (\mathbf{v}_L \times \mathbf{B}_p). \quad (5.57)$$

This is very different from the evolution equation used by [Elfritz et al. \(2016\)](#) (see their equation 16). Firstly, as pointed out by [Dommes & Gusakov \(2017\)](#), the magnetic field is locked into flux tubes, and therefore, the evolution of the magnetic field must be governed by an advection equation of the form Equation (5.57), where the field is advected at the same velocity as the flux tubes,  $\mathbf{v}_L$ . However the evolution equation of [Elfritz et al. \(2016\)](#) does not advect the magnetic field at the velocity  $\mathbf{v}_L$ . This appears to be one of the reasons why their timescales are several orders of magnitude longer than the evolution governed by Equation (5.57).

It is important to note that the transport velocity of flux can be significantly larger than the electron drift velocity, which tends to be slowed by the formation of sharp pressure gradients in most typical cases. For this reason we neglect the electron velocity in these calculations, and define the Jones drift velocity

$$\mathbf{v}_J = \frac{\alpha}{4\pi}(\mathbf{B} \cdot \nabla)\mathbf{H}_{c1}, \quad \alpha = \tilde{\sigma}/n_e^2 e^2, \quad (5.58)$$

with  $\alpha$  an effective drag coefficient, and consider transport of flux due to this effect in isolation ( $\mathbf{v}_L = \mathbf{v}_J$ ). As in Section 3 we write the evolution equation in terms of the scalar functions  $\Psi$  and  $I$ ,

$$\frac{\partial \Psi}{\partial t} + \mathbf{v}_J \cdot \nabla \Psi = 0, \quad (5.59)$$

while  $I$  satisfies Equation (4.5). J2006 estimates  $\tilde{\sigma} \approx 10^{29} - 10^{32} B_{12}^{-1} \text{ s}^{-1}$ , depending on the composition of the core. We use in our simulations  $\tilde{\sigma} = 10^{29} B_{12}^{-1} \text{ s}^{-1}$ . For a  $1.4M_\odot$  neutron star, a typical baryon density at the center of the core is  $n_B \approx 3.5 \times 10^{38} \text{ cm}^{-3}$  ([Li et al., 2016b](#)). We take a central electron fraction  $Y_e = 0.1$ , which gives  $n_e = Y_e n_B = 3.5 \times 10^{37} \text{ cm}^{-3}$ . Rather than adopt a particular equation of state we use these conservative values to calculate  $\alpha$  throughout the core, which will cause the field evolution to be slower in the outer core in our simulations. But for our purposes we want to understand the dynamics of flux tubes on long timescales, and this will not effect the end state of our simulations.

### 5.3 Numerical Details

In our code we evaluate the components of the vector  $\mathbf{H}_{c1}$  as

$$\mathbf{H}_{c1} = \frac{H_{c1}}{B}\mathbf{B}, \quad (5.60)$$

using the derivative formula in Equation (3.41). We set ghost points on the poles for  $\mathbf{H}_{c1}$  according to axisymmetry,

$$H_r^{j1-1} = H_r^{j1+1}, \quad (5.61)$$

$$H_r^{j2+1} = H_r^{j2-1} \quad (5.62)$$

$$H_{\theta}^{j1-1} = -H_{\theta}^{j1+1} \quad (5.63)$$

$$H_{\theta}^{j2+1} = -H_{\theta}^{j2-1} \quad (5.64)$$

We are now able to evaluate the components of the Jones drift velocity, Equation (5.58), using our computed components of  $\mathbf{H}_{c1}$ . We evaluate the Jones drift velocity using the derivative formula in Equation (3.41) as

$$\mathbf{v}_J = \frac{2.9 \times 10^{-8}}{B_{14}} (\mathbf{B}_{14} \cdot \tilde{\nabla}) \mathbf{H}_{c1}^{15}, \quad (5.65)$$

where we have normalized  $\alpha = 3.54 \times 10^{-30}/B_{14}$ ,  $\mathbf{B}_{14} = \mathbf{B}/10^{14}$  G,  $\mathbf{H}_{c1}^{15} = \mathbf{H}_{c1}/10^{15}$ , and  $\tilde{\nabla}$  is the del operator with lengths normalized to  $10^6$  cm. Note that the factor  $1/4\pi$  has been included in the numerical prefactor. Similarly, normalization of the magnetic field evolution equation is then,

$$\frac{\partial \mathbf{B}_{14}}{\partial t_{\text{yr}}} = 31.5 \tilde{\nabla} \times (\mathbf{v}_J \times \mathbf{B}_{14}). \quad (5.66)$$

We step the crust and the core sequentially, so that when we step the crust, the core is the boundary condition, ie. we set  $\Psi_{\text{crust}}(r_c) = \Psi_{\text{core}}(r_c)$ . Then, the crust provides the boundary condition when we step the core, so we set  $\Psi_{\text{core}}(r_c) = \Psi_{\text{crust}}(r_c)$ . For more details of the numerical method we refer the reader to Appendix B.

## 5.4 Results

Jones drift allows flux tubes to straighten by slipping with some viscous dissipation through the core electron fluid. As the flux tubes straighten, free energy stored in the curvature of the flux tubes is dissipated. The characteristic timescale of this straightening is

$$\tau_{\text{diss}} \sim \frac{s}{v_J} \quad (5.67)$$

with  $s$  the deviation from straight flux tubes. We approximate a curved flux tube as a circular arc, with  $s \approx r_c^2/2R_c$ , and radius of curvature  $R_c$ . The Jones drift velocity is approximated

$$v_J \sim \frac{\tilde{\sigma}}{4\pi n_e^2 e^2} \frac{BH_{c1}}{R_c}. \quad (5.68)$$

The timescale for flux tubes to straighten is then

$$\tau_{\text{diss}} \sim \frac{2\pi n_e^2 e^2}{\tilde{\sigma}} \frac{r_c^2}{BH_{c1}} = 450 \left( \frac{n_e}{3.5 \times 10^{37} \text{ cm}^{-3}} \right)^2 \left( \frac{10^{29} \text{ s}^{-1}}{\tilde{\sigma}} \right) \text{ kyr}, \quad (5.69)$$

where we have taken the estimate of J2006  $\tilde{\sigma} = 10^{29} B_{12}^{-1} \text{ s}^{-1}$ . Note that the timescale is independent of the field strength  $B$ . The timescale for straightening can also be significantly

shorter than the above estimate, depending on  $\tilde{\sigma}$ , which can be larger for cores with high muon densities J2006.

The Jones drift velocity acts perpendicular to poloidal field lines, in order to minimize the curvature. Thus, Jones' effect becomes inactive when the flux tubes are straightened. However, when the field is straightened in the core, a sharp cusp forms on the crust-core interface, supported by strong toroidal currents at the base of the crust. This cusp will therefore be site to rapid Ohmic diffusion, which smooths the cusp, generating curvature in the field lines, and reactivating Jones' effect in the core, which proceeds to straighten them again. So we see that the coupled crust-core system continuously evolves under the combined effects of Jones' flux tube drift in the core, and Ohmic diffusion in the crust. In this section we explore the evolution in two scenarios.

Firstly, we consider the drift of flux tubes in a strongly magnetized neutron star, with Hall drift and Ohmic diffusion active in the crust. Secondly, we study the long timescale evolution of a pulsar strength magnetic field, in order to determine the decay timescale.

#### 5.4.1 Flux tube drift and Hall drift (strong B)

For strong magnetic fields, Hall drift can interfere with the flux tube drift in the core (when  $t_{\text{Hall}}$  is comparable to  $\tau_{\text{diss}}$ ). Figure 5.3 shows the evolution of a highly magnetized neutron star (model B) with an initially poloidal field, evolving by Jones' flux tube drift in the core, coupled to a crust evolving with Hall drift and Ohmic diffusion. For this simulation we use  $\tilde{\sigma} = 10^{29} B_{12}^{-1} \text{s}^{-1}$ . The field has maximum strength  $B \approx 3 \times 10^{14}$  G in the core. The initial field displays equatorial symmetry, and thus Hall drift will not inject any magnetic twist into the core, meaning that the toroidal field remains zero there.

There are two main stages to the evolution of the core magnetic field in model B. The first stage lasts for  $\tau_{\text{diss}}$ , and involves a rapid straightening of the flux tubes in order to relieve magnetic stresses. During this stage the core field dissipates its initial free energy, on viscous slippage through the fluid. The straightening of flux tubes in the core is associated with the formation of a sharp cusp in the poloidal field at the crust-core interface, supported by a toroidal current sheet at the base of the crust. This current sheet generates toroidal field deep in the crust through the Hall effect. The current sheet is also site to enhanced ohmic dissipation. The regions of toroidal field in the crust are advected toward the equator, and much weaker higher order multipole structure forms in the toroidal field which is efficiently damped. The toroidal field is sufficiently weak, that it does not cause any large scale rearrangement of the poloidal

field. Eventually activity due to Hall drift declines, as the Hall attractor drives the poloidal field in the crust to a state of rigid rotation of the electron fluid.

The second stage begins at  $t \sim 1$  Myr. During this stage, Ohmic diffusion controls the evolution, which becomes a self-similar decay of the global magnetic field. Jones drift allows the core magnetic field to adjust on a timescale which is faster than Ohmic diffusion at the base of the crust, so that they effectively remain straight for the remainder of the evolution. Flux tubes in the core gradually drift outward, consistent with the rate of Ohmic diffusion at the base of crust. Flux in the core converges toward the null point in the field, which is located at the equator, on the crust-core interface, for this particular configuration. At the null point, the field lines close and annihilate, through a combination of Jones drift in the core, and Ohmic diffusion in the crust. The evolution of the field into this state of self similar decay is not unique to these initial conditions, and we observe the same final state for a number of approximately dipole initial magnetic fields. We note that the Jones drift timescale does not scale with field strength, and likewise with Ohmic diffusion. This implies that timescales relating to the evolution of poloidal fields in model B could be applied to initial fields with a variety of strengths.

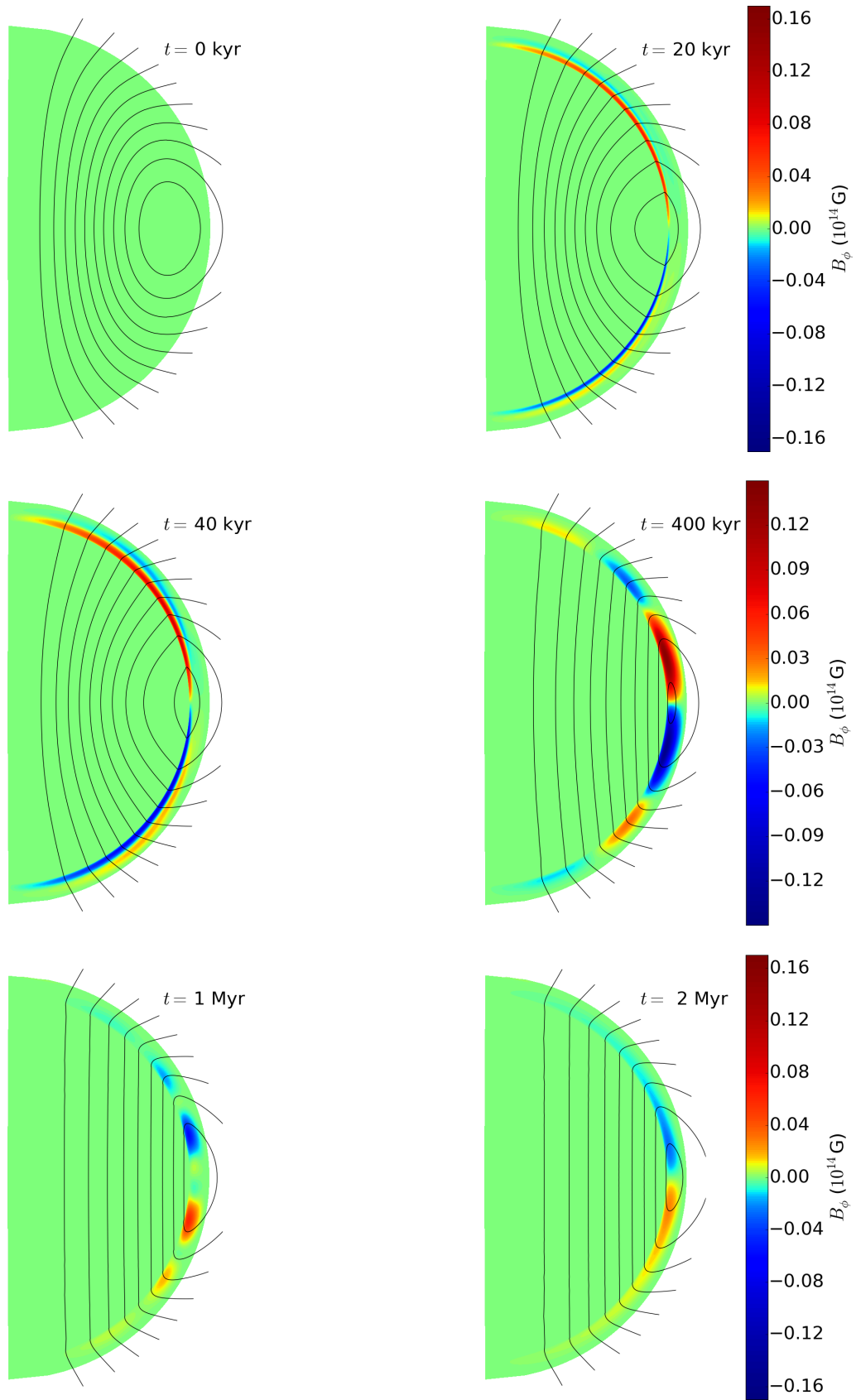


Figure 5.3: Snapshots of the magnetic field evolution for Model B (Table 1.1), shown at  $t = 0$  kyr, 20 kyr, 40 kyr, 400 kyr, 1 Myr, and 2 Myr. The plotting scheme is the same as Figure 4.5.

### 5.4.2 Flux tube drift and no Hall drift (moderate $B$ )

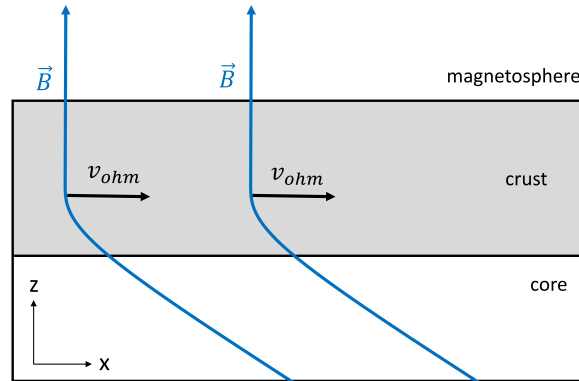


Figure 5.4: Plane parallel slab (black), with length  $l$ . Field lines (blue) move to the right consistent with the rate set by Ohmic diffusion.

The second scenario of interest is the evolution of pulsar strength magnetic fields due to Jones flux tube drift in the core. As seen in Figure 5.3, Hall drift plays a minor role in the long term distribution of magnetic flux in the star. For fields  $B \approx 10^{12}$  G, is slower than Ohmic diffusion [Equation (3.14)], and will have even less of an effect. With this in mind, in Model C [Table 1.1] we consider the crust evolving under Ohmic diffusion only so that long timescale simulations are less computationally expensive. We also avoid evolving the flux tubes in the core directly [Equation (5.59)], and instead enforce the boundary condition at the base of the crust that field lines remain vertical in the core ( $B_\theta = B_r \tan \theta$  at  $r = r_c$ ) as a consequence of Jones drift. This is a good approximation because the flux tubes can always straighten faster than Ohmic diffusion at the base of the crust, as seen in Figure 5.3.

The timescale for magnetic flux to diffuse through the crust in the above scenario is very different from the Ohmic timescale of [Goldreich & Reisenegger \(1992\)](#). As an approximation, consider the cartesian configuration shown in Figure 5.4, and assume a constant diffusivity  $\eta$  throughout the crust. The curvature of the field lines at the base of the crust generates a current sheet of thickness  $h$ , given by Ampere's law as

$$j \sim -\frac{c}{4\pi} \frac{B_x}{h}, \quad (5.70)$$

using Ohm's law this gives the electric field

$$E \sim -\frac{c}{4\pi\sigma} \frac{B_x}{h}. \quad (5.71)$$

The electric field determines  $\partial \mathbf{B} / \partial t = -c \nabla \times \mathbf{E}$ . Using the fact that  $\mathbf{E} = E_y \hat{\mathbf{e}}_y$  is perpendicular to  $\mathbf{B}$ , one may rewrite the evolution equation as  $\partial \mathbf{B} / \partial t = \nabla \times (\mathbf{v} \times \mathbf{B})$  with  $\mathbf{v}$  defined by

$\mathbf{E} = -\mathbf{v} \times \mathbf{B}/c$ . In this form, the equation describes the motion of magnetic field lines with velocity  $\mathbf{v}$ , which we call  $\mathbf{v}_{\text{Ohm}}$ . The resulting velocity of field lines in the x-direction is

$$v_{\text{Ohm}} \sim \frac{\eta B_x}{h B_z}, \quad (5.72)$$

with  $B_z$  and  $B_x$  the vertical and horizontal components of the field. A quasi-steady drift is established with the current sheet occupying the region of the crust with highest conductivity, i.e. the deep crust. Its thickness  $h$  is a few hundred meters. The quasi-steady drift is established on the timescale  $h^2/\eta$ , and the drift is associated with the transport of magnetic field lines with characteristic time

$$\begin{aligned} \tau_{\text{Ohm}} &\sim \frac{hl B_z}{\eta B_x} \\ &= 150 \left( \frac{h}{3 \times 10^4 \text{ cm}} \right) \left( \frac{l}{\pi r_*} \right) \left( \frac{\sigma}{3.6 \times 10^{24} \text{ s}^{-1}} \right) \text{Myr}, \end{aligned} \quad (5.73)$$

where we have assumed  $B_z \approx B_x$ , and the current sheet thickness  $h \approx 3 \times 10^4$  cm corresponding to the highly conducting region of the deep crust. We have used  $\sigma = 3.6 \times 10^{24} \text{ s}^{-1}$ , corresponding to phonon scattering at  $T \approx 2 \times 10^8$  K (Gourgouliatos & Cumming, 2014). This timescale can be greater by an order of magnitude compared to the Ohmic timescale of Goldreich & Reisenegger (1992), depending on the thickness of the crust and the geometric factor  $B_z/B_x$ .

Figure 5.5 shows the long timescale evolution of Model C, with Jones flux tube drift in the core, coupled to a crust with Ohmic diffusion. The field in the core is pure  $B_z$  (In particular  $\Psi \propto r_{\perp}^2$ ), and the initial crustal field is a dipole potential field matched on to the core. The field has typical strength  $B \approx 10^{12}$  G. In the first  $h^2/\eta \sim 1$  Myr, diffusion at the base of the crust smooths the kink in the poloidal field, and the crustal field relaxes into an Ohmic eigenmode. From this point on the evolution of the global field can be described by self similar decay. Tension in the magnetosphere ensures that poloidal field lines in the crust converge toward the null point at the equator. The field lines in the core are pulled along at the rate set by Ohmic diffusion, also toward the null point at the base of the crust, where they close and annihilate. For the remainder of the evolution the structure of the magnetic field remains unchanged, as it gradually grows weaker. The evolution of the dipole field strength is plotted in Figure 5.6. After  $\sim 150$  Myr, the dipole field strength has decreased from  $B \approx 10^{12}$  G to  $B \approx 10^9$  G. We can see that our timescale Equation (5.73) corresponds to the time taken for the dipole field strength to decay by approximately 3 orders of magnitude for the numerical simulation seen in Figure 5.5.

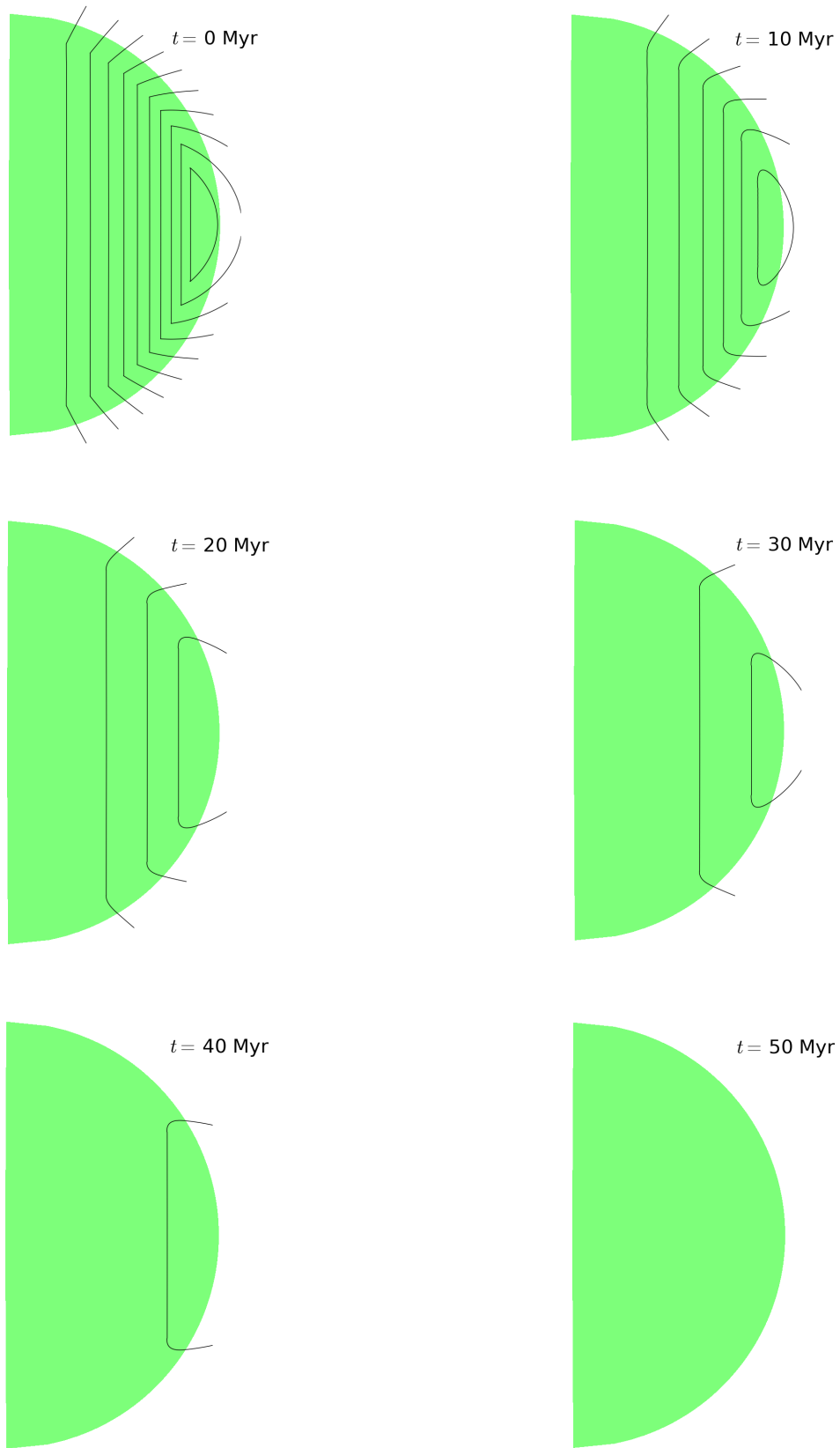


Figure 5.5: Snapshots of the magnetic field evolution for Model C (Table 1.1), shown at  $t = 0$  Myr, 10 Myr, 20 Myr, 30 Myr, 40 Myr, and 45 Myr. The plotting scheme is the same as Figure 4.5. The toroidal field is everywhere zero.

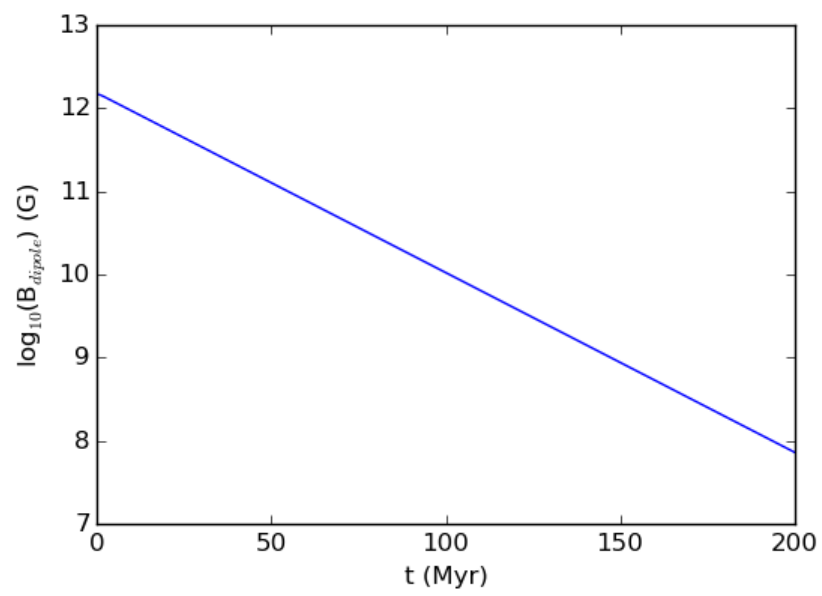


Figure 5.6: Decay of the dipole field for the magnetic field evolution shown in Figure 5.5.

## Monash University Declaration Chapter 6

### Declaration by candidate:

I declare that my contribution to the work in Chapter 6 that is submitted to the Monthly Notices of the Royal Astronomical Society as [Bransgrove et al. \(2017\)](#), involved the following:

The writing of the publication, formulating the vortex-flux tube cut-through criterion, formulating the flux tube drift velocity, development of numerical methods including boundary conditions, development of the numerical code, running simulations, and all other work contained therein (that is not referenced otherwise).

Extent of contribution by candidate: 85%

Co-author names: Yuri Levin, Andrei Beloborodov

Nature of co-author's contribution: Formulating the vortex-flux tube cut-through criterion, formulating the flux tube drift velocity, development of numerical methods, and feedback during writing of the paper.

I have renumbered sections, equations and figures of the published paper in order to generate a consistent presentation within the thesis. The undersigned hereby certify that the above declaration correctly reflects the nature and extent of the student's and co-authors' contributions to this work.

Candidate Signature:

Date: June 29, 2017

Main Supervisor signature:



Date: June 29, 2017

# Chapter 6

## Spin-down of Superfluid Cores

Partially adapted from:

*Magnetic Field Evolution of Neutron Stars I: Basic formalism, numerical techniques, and first results*, Ashley Bransgrove, Yuri Levin, and Andrei Beloborodov, 2017, submitted for publication in MNRAS.

## 6.1 Rotating Neutron Superfluid

In conventional neutron star models, neutrons in the core form cooper pairs, and exist in a  ${}^3P_2$  superfluid state (Baym & Pethick, 1975). The vorticity of the bulk fluid must be zero, and circulation is quantized on microscopic scales with the formation of superfluid vortices, with the quantum of circulation  $\kappa = h/2m_n$  where  $h$  is the Planck constant, and  $2m_n$  is the effective mass of a cooper pair. The mean number density of vortices is

$$n_v = \frac{2\Omega_n}{\kappa}, \quad (6.1)$$

where  $\Omega_n$  is the superfluid rotational frequency. The neutron vortices are not necessarily straight, though the absence of a firm detection of precession in all but one pulsar (Stairs et al., 2000), seems to indicate that the vortex configuration is not radically different from a linear array.

To determine the motion of neutron vortices during stellar spin-down, we consider the balance of forces on a neutron vortex in the co-rotating frame of reference. We consider an axisymmetric incompressible neutron fluid, rotating with angular velocity  $\mathbf{\Omega}_n = \Omega_n \hat{\mathbf{e}}_z$ . It is a well known result that the total conservative force acting on a neutron vortex is the magnus force. Jones (1991) gives the magnus force per unit length as

$$\tilde{\mathbf{f}}_M^n = \rho_n(\mathbf{v}_{n0} - \mathbf{v}_L) \times \boldsymbol{\kappa}, \quad (6.2)$$

with  $\rho_n$  the mass density of superfluid neutrons,  $\mathbf{v}_{n0}$  a large scale background flow of the neutron liquid,  $\mathbf{v}_L$  the velocity of the neutron vortex, and  $\boldsymbol{\kappa} = \kappa \hat{\mathbf{e}}_n$ . We use  $\hat{\mathbf{e}}_n$  as a unit vector to indicate the local direction along a neutron vortex. Here we assume a uniform array of neutron vortices with  $\hat{\mathbf{e}}_n = \hat{\mathbf{e}}_z$ , so that the vortices are aligned with the axis of rotation. We will discuss the validity of this assumption in more detail later. Now we calculate the magnus force per unit volume as,

$$\mathbf{f}_M^n = n_v \tilde{\mathbf{f}}_M^n = 2\rho_n(\mathbf{v}_{n0} - \mathbf{v}_L) \times \mathbf{\Omega}_n. \quad (6.3)$$

In the co-rotating frame, the vortices feel a tangential force in the azimuthal direction from the spin-down of the fluid. The force per unit volume is

$$\mathbf{f}_E^n = -\rho_n \dot{\mathbf{\Omega}}_n \times \mathbf{r}_\perp, \quad (6.4)$$

which is the Euler force. Since the magnus force is the total conservative force experienced by the neutron vortex, it must balance the Euler force ( $\mathbf{f}_M^n = \mathbf{f}_E^n$ ). This gives the equality

$$-\rho_n \dot{\mathbf{\Omega}}_n \times \mathbf{r}_\perp = 2\rho_n(\mathbf{v}_{n0} - \mathbf{v}_L) \times \mathbf{\Omega}_n. \quad (6.5)$$

In order to solve this equation for  $\mathbf{v}_L$ , we take the cross product of both sides with  $\boldsymbol{\Omega}_n$ . We also assume that  $\mathbf{v}_L \cdot \boldsymbol{\Omega}_n = 0$  and  $\mathbf{v}_{n0} \cdot \boldsymbol{\Omega}_n = 0$ , since any velocity in the  $\hat{\mathbf{e}}_z$  direction will not change the density of vortices  $n_v$ , in this cylindrical geometry. Solving for  $\mathbf{v}_L$  yields the expression

$$\mathbf{v}_L = \mathbf{v}_{n0} - \frac{r_\perp \dot{\Omega}_n}{2\Omega_n} \hat{\mathbf{e}}_{r_\perp} \quad (6.6)$$

Stellar spin-down must be accompanied by motion of these vortices outward, and likewise spinning up the star must be accompanied by motion of the neutron vortices inward, as shown by [Ruderman & Sutherland \(1974\)](#). The neutron vortices move in the radial direction with velocity

$$\mathbf{v}_\perp = -\frac{r_\perp \dot{\Omega}_n}{2\Omega_n} \hat{\mathbf{e}}_{r_\perp}, \quad (6.7)$$

due to the spin-down or the liquid core.

## 6.2 Vortex - Flux Tube Interactions

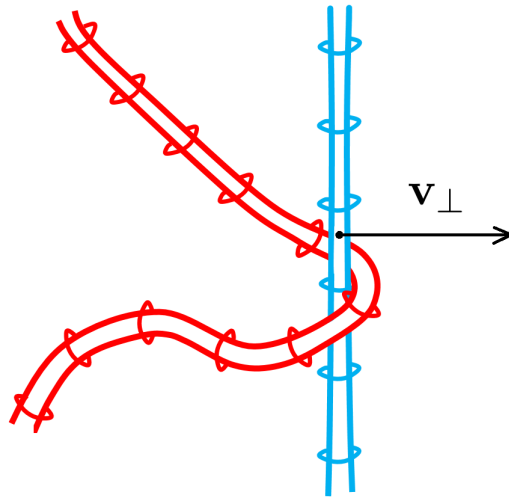


Figure 6.1: Vortex - flux tube interactions: A magnetized superfluid neutron vortex (blue) moving at velocity  $\mathbf{v}_\perp$  pulls along a flux tube (red).

As a consequence of the neutron superfluid coupling to the proton superfluid, protons also circulate around the neutron vortices, which produces magnetization localized within the penetration depth  $\lambda \lesssim 10^{-11}$  cm of the neutron vortex core [see eg. [Jones \(1991\)](#)]. Outward moving neutron vortices interact strongly with flux tubes, and thus the spin-down of neutron stars can result in the transport of magnetic flux ([Srinivasan et al., 1990](#)). According to [Ruderman et al. \(1998\)](#), force builds up on the flux tubes, which are either carried along with the neutron vortices, or are cut through by them. We now estimate the maximum force flux tubes can exert

on an array of neutron vortices before cut-through occurs. We denote the microscopic magnetic field of a flux tube as

$$\mathbf{B}_\Phi = \frac{\phi_0}{\pi\lambda^2} \ln\left(\frac{\lambda}{\xi_p}\right), \quad (6.8)$$

and the microscopic flux density of a neutron vortex as

$$\mathbf{B}_v = \frac{\phi_0^*}{\pi\lambda^2}. \quad (6.9)$$

Here  $\phi_0^*$  is the non-quantized magnetic flux possessed by a neutron vortex, due to the circulation of entrained superfluid protons. When a flux tube intersects a neutron vortex, the magnetic energy density is

$$\frac{(\mathbf{B}_\Phi + \mathbf{B}_v) \cdot (\mathbf{B}_\Phi + \mathbf{B}_v)}{8\pi}. \quad (6.10)$$

Expanding this expression, we identify the cross terms as the interaction energy,

$$E_{\text{int}} = 2 \frac{\mathbf{B}_\Phi \cdot \mathbf{B}_v}{8\pi}, \quad (6.11)$$

which is in agreement with the pinning energy of [Gügercinoğlu & Alpar \(2016\)](#). We then estimate the maximum force per unit length before cut-through as

$$\tilde{f}_v = E_{\text{int}} \left( \frac{\pi\lambda^2}{l} \right), \quad (6.12)$$

with  $\pi\lambda^2$  the area of intersection, and  $l$  the distance between intersections along the neutron vortex. [Jones \(1991\)](#) and J2006 set  $l = d$ , the average flux tube separation. However, since there are many more flux tubes than neutron vortices, as a neutron vortex moves along and collects flux tubes, eventually the flux tubes will cover the length of neutron vortex. In this regime, the separation between flux tubes along the vortex approaches  $l = 2\lambda$ , which is also supported by [Ruderman et al. \(1998\)](#)<sup>1</sup>, and [Gügercinoğlu & Alpar \(2016\)](#). This gives the maximum force per unit length as

$$\tilde{f}_v = \frac{\phi_0\phi_0^*}{8\pi^2\lambda^3} \ln\left(\frac{\lambda}{\xi_p}\right) \approx 3.8 \times 10^{17} \text{ dyne/cm}. \quad (6.13)$$

### 6.3 Flux Transport by Superfluid Neutron Vortices

In this section we outline our treatment of large scale flux tube transport by interactions with superfluid vortices. We envisage an array of flux tubes threading through an array of superfluid vortices, similar to the picture of [Ruderman et al. \(1998\)](#) [see Figure 6.2]. J2006 provides a

---

<sup>1</sup>These authors have corrected a typo in the interaction energy of [Ruderman et al. \(1998\)](#) which erroneously leads to a factor of  $\pi^2$  larger pinning energies.

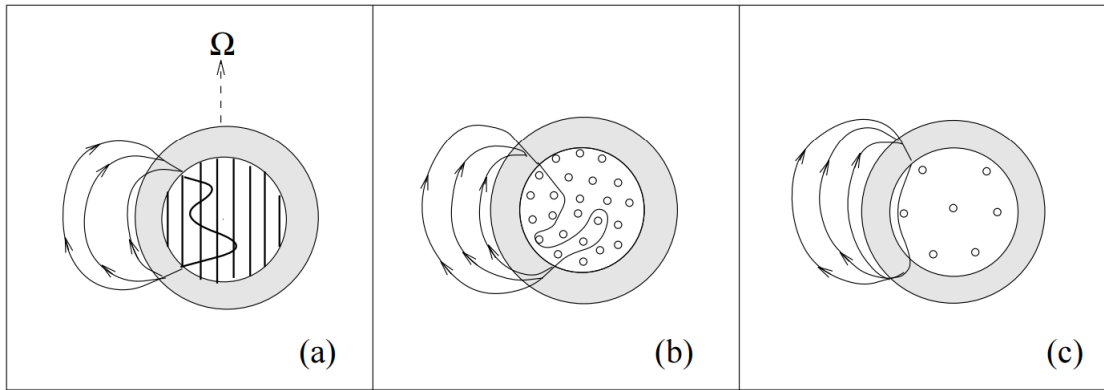


Figure 6.2: Ruderman's model of flux tube transport. (a) Side view of a flux tube (thicker line), threading through vortices in the core. (b) Top view of (a) from along the spin-axis. (c) Top view of flux tubes in the equatorial region after spin-down. Image credit: [Ruderman et al. \(1998\)](#).

treatment for flux tube transport for the case of straight flux tubes ( $\mathbf{f}_B = 0$ ). J2006 argues that the terminal velocity of a flux tube array being pulled along by neutron vortices is given by

$$\mathbf{v}_F = \alpha n_v \tilde{f}_v \hat{\mathbf{e}}_{r_\perp}, \quad (6.14)$$

where  $\alpha$  is the drag coefficient defined in Equation (5.58), and  $\tilde{f}_v$  is the maximum force per unit length a neutron vortex can exert on a flux tube without cutting through. J2006 states that in order for the flux tubes to be pushed along by neutron vortices with velocity

$$\mathbf{v}_\perp = -\frac{r_\perp \dot{\Omega}_n}{2\Omega_n} \hat{\mathbf{e}}_{r_\perp}, \quad (6.15)$$

the following inequality must be satisfied,

$$|\mathbf{v}_F| \geq |\mathbf{v}_\perp|, \quad (6.16)$$

which is in agreement with [Ruderman et al. \(1998\)](#). If this inequality is not satisfied, the neutron vortices will cut through the flux tubes.

We extend the treatment of J2006 and [Ruderman et al. \(1998\)](#) to include the vortex self-tension force  $\mathbf{f}_B$ , and also discuss the transport of flux tubes in the cut-through regime. We begin by specifying a modified cut-through criterion. That is, if the sum of the drag force, and self tension force flux tubes exerted on the neutron vortices exceeds the the maximum possible force, cut-through will occur. We say that cut-through occurs when

$$\left| -\frac{\mathbf{v}_\perp}{\alpha} \cdot \hat{\mathbf{e}}_{r_\perp} + \mathbf{f}_B \cdot \hat{\mathbf{e}}_{r_\perp} \right| \geq n_v \tilde{f}_v, \quad (6.17)$$

with  $-\mathbf{v}_\perp \cdot \hat{\mathbf{e}}_{r_\perp}/\alpha$  the drag force the flux tubes exert on the neutron vortices (assuming a stationary background fluid),  $\mathbf{f}_\mathbf{B} \cdot \hat{\mathbf{e}}_{r_\perp}$  the tension force flux tubes exert on the vertical vortices, and  $n_v \tilde{f}_v$  the maximum force per unit volume the neutron vortices can exert on the flux tubes. We call satisfaction of the above inequality “cut-through”, and dissatisfaction of the inequality “vortex-transport”.

In the transport regime, the flux tubes are carried along with velocity  $\mathbf{v}_\perp$ . But the flux tubes also have the freedom to slide along the neutron vortices, with the projected Jones drift velocity  $(\mathbf{v}_\mathbf{J} \cdot \hat{\mathbf{e}}_n)\hat{\mathbf{e}}_n$ .

In the cut-through regime, we assume that the flux tubes are still carried along by the neutron vortices, but only at the terminal velocity  $\mathbf{v}_F$ . Since the vortices cannot prevent the motion of flux tubes in the cut-through regime, the flux tubes can also drift in accordance with their own self tension (the Jones drift velocity  $\mathbf{v}_\mathbf{J}$ ). To summarize the flux tubes are advected with the velocity field

$$\mathbf{v}_{\text{sd}} = \begin{cases} \mathbf{v}_\perp + (\mathbf{v}_\mathbf{J} \cdot \hat{\mathbf{e}}_n)\hat{\mathbf{e}}_n, & \text{(vortex-transport)} \\ \mathbf{v}_F + \mathbf{v}_\mathbf{J}, & \text{(cut-through)} \end{cases} \quad (6.18)$$

while the neutron vortices move with velocity  $\mathbf{v}_\perp$ . We assume that the neutron vortex array is not significantly deformed by the flux tubes. This is true when for high spin frequencies. Specifically, when

$$|\rho_n(\mathbf{v}_{n0} - \mathbf{v}_L) \times \boldsymbol{\kappa}| > \frac{\mathbf{B}_\Phi \cdot \mathbf{B}_v}{8\pi} \lambda, \quad (6.19)$$

the force of flux tubes pushing on the vortices is small, and the flux tubes cannot significantly alter the structure of the vortex array. The relative velocity of the vortex array and the background neutrons cannot exceed the spin-down velocity of the fluid,

$$\|\mathbf{v}_{n0} - \mathbf{v}_L\| \leq r_\perp \Omega_n, \quad (6.20)$$

so that

$$\rho_n r_\perp \Omega_n \kappa \geq \frac{\mathbf{B}_\Phi \cdot \mathbf{B}_v}{8\pi} \lambda. \quad (6.21)$$

Assuming  $\Omega = \Omega_n$ , gives the following constraint on the stellar spin frequencies

$$\Omega \geq \lambda \frac{\mathbf{B}_\Phi \cdot \mathbf{B}_v}{8\pi r_\perp \rho_n \kappa} \quad (6.22)$$

For typical values this gives  $P \leq 6.3$  s, with  $P = 2\pi/\Omega$  the spin period. We find this is satisfied in our simulations.

The evolution of the magnetic field due to motion of neutron vortices is given by

$$\frac{\partial \mathbf{B}_p}{\partial t} = \nabla \times (\mathbf{v}_{sd} \times \mathbf{B}_p). \quad (6.23)$$

In terms of the scalar function  $\Psi$ , the evolution is

$$\frac{\partial \Psi}{\partial t} + \mathbf{v}_{sd} \cdot \nabla \Psi = 0, \quad (6.24)$$

while the toroidal field evolves according to hydromagnetic equilibrium.

## 6.4 Numerical Details

In this section we give a summary of our numerical implementation of our model for flux tube transport described in the previous section. We model the spin evolution of the star self-consistently according to  $\dot{\Omega} = -\beta\Omega^3$ , where  $\beta = 2a_1^2/3c^3I$ . Here  $a_1$  is the dipole moment of the surface magnetic field which we evaluate at each time step. We take  $I = 10^{45}$  g cm<sup>2</sup> as a typical moment of inertia. In our code we evaluate the velocity fields

$$\mathbf{v}_\perp = 5 \times 10^5 \frac{r_6 \sin \theta \dot{P}}{P} \hat{\mathbf{e}}_{r_\perp}, \quad (6.25)$$

$$\mathbf{v}_F = \frac{8.45 \times 10^{-9}}{B_{14} P} \hat{\mathbf{e}}_{r_\perp}, \quad (6.26)$$

$$\mathbf{v}_J = \frac{2.9 \times 10^{-8}}{B_{14}} (\mathbf{B}_{14} \cdot \tilde{\nabla}) \mathbf{H}_{cl}^{15}, \quad (6.27)$$

throughout the core, using the finite difference formula Equation (3.41). We have used  $\alpha = 3.54 \times 10^{-30}/B_{14}$ ,  $\mathbf{B}_{14} = \mathbf{B}/10^{14}$  G,  $\mathbf{H}_{cl}^{15} = \mathbf{H}_{cl}/10^{15}$ , and  $\tilde{\nabla}$  is the del operator with lengths normalized to  $10^6$  cm.  $P$  and  $\dot{P}$  are the spin period and period derivative. In spherical coordinates,

$$\hat{\mathbf{e}}_{r_\perp} = \sin \theta \hat{\mathbf{e}}_r + \cos \theta \hat{\mathbf{e}}_\theta. \quad (6.28)$$

We find that it is convenient to multiply both sides of the cut-through criterion Equation (6.16) by  $\alpha$ , so that it may be written in terms of velocity fields only,

$$|-\mathbf{v}_\perp \cdot \hat{\mathbf{e}}_{r_\perp} + \mathbf{v}_J \cdot \hat{\mathbf{e}}_{r_\perp}| \geq \mathbf{v}_F, \quad (6.29)$$

We then set the velocity field depending on local satisfaction of the inequality [Equation (6.29)], according to

$$\mathbf{v}_{sd} = \begin{cases} \mathbf{v}_\perp + (\mathbf{v}_J \cdot \hat{\mathbf{e}}_n) \hat{\mathbf{e}}_n, & \text{(vortex-transport)} \\ \mathbf{v}_F + \mathbf{v}_J, & \text{(cut-through)} \end{cases} \quad (6.30)$$

The vector  $\hat{\mathbf{e}}_n = \hat{\mathbf{e}}_z$  is written in spherical coordinates as

$$\hat{\mathbf{e}}_n = \cos \theta \hat{\mathbf{e}}_r - \sin \theta \hat{\mathbf{e}}_\theta. \quad (6.31)$$

In regions of cut-through, we can then write the projected Jones velocity as

$$(\mathbf{v}_J \cdot \hat{\mathbf{e}}_n) \hat{\mathbf{e}}_n = (v_J^r \cos^2 \theta - v_J^\theta \cos \theta \sin \theta) \hat{\mathbf{e}}_r + (v_J^\theta \sin^2 \theta - v_J^r \cos \theta \sin \theta) \hat{\mathbf{e}}_\theta. \quad (6.32)$$

We can then evaluate the evolution of the magnetic field through the equation

$$\frac{\partial \mathbf{B}_{14}}{\partial t_{\text{yr}}} = 31.5 \tilde{\nabla} \times (\mathbf{v}_J \times \mathbf{B}_{14}), \quad (6.33)$$

with  $t_{\text{yr}} = t/3.15 \times 10^7$  s. We step the crust and the core sequentially, so that when we step the crust, the core is the boundary condition, ie. we set  $\Psi_{\text{crust}}(r_c) = \Psi_{\text{core}}(r_c)$ . Then, the crust provides the boundary condition when we step the core, so we set  $\Psi_{\text{core}}(r_c) = \Psi_{\text{crust}}(r_c)$ . We add a small amount of artificial diffusion in order to achieve numerical stability. The artificial diffusion does not effect our results since we ensure it occurs on timescales much longer than we are simulating. For more details of the numerical method we refer the reader to Appendix B.

## 6.5 Results

The origin of strong magnetic fields in neutron stars is not well understood. Some models suggest a fossil field, left behind by the progenitor (Ferrario & Wickramasinghe, 2006), while others invoke dynamo mechanisms requiring the neutron star to be born with millisecond spin periods (Thompson & Duncan, 1993). Here we assume that a highly magnetized neutron star can be born with a 1 millisecond spin period, and consider the implications for the evolution of the magnetic field. In particular, we are interested in the interaction of superfluid neutron vortices with flux tubes, as a means for the rotational energy of the star to rearrange the core magnetic field. Importantly the cooling curves of the Cas A remnant suggest that the transition to superfluidity in the core takes place after  $t \sim 300$  years [Shternin et al. (2011), Page et al. (2011)]. As was pointed out by Thompson et al. (2017), by this time a typical magnetar ( $B \sim 10^{15}$  G) will have a spin period  $> 1$  s. It is simple to show that the ratio of rotational to magnetic energy is very small, and it is difficult to envisage how the core field could be significantly rearranged by a transfer of rotational energy. However, for neutron stars born with weaker magnetic fields, this is not the case. Specifically, if a neutron star is born with initial spin period 1 ms, and  $B \sim 10^{13}$  G, then after 300 years, the spin period will be  $> 20$  ms. It is then simple to show that the ratio of rotational to magnetic energy is large, and will remain so for an extended period after the transition to neutron superfluidity.

In our axisymmetric model, we are limited to the case with the magnetic axis aligned with the spin axis. In general this will not be true, however a 3D code is required to solve this problem, since a spin axis misaligned from the magnetic axis violates axisymmetry. In our axisymmetric models we assume that the flux tubes are weakly tangled around the neutron vortices, so that even though both the flux tubes and vortices exist in the  $\phi = \text{const}$  plane, the flux tubes are still constrained to move with the vortices in accordance with the velocity given by Equation (6.18).

In Models D1, D2, and D3, we model a neutron star assuming a birth spin period of 1 ms, and a range of magnetic fields strengths [see Table 1.1]. Specifically, we assume that the star spins down through dipole braking for 300 years, before the transition to superfluidity, which is when we begin our simulations. The spin period at 300 years is set depending on the strength of the magnetic field in the particular model. We model the spin evolution of the star self consistently according to  $\dot{\Omega} = -\beta\Omega^3$ , where  $\beta = 2a_1^2/3c^3I$ . Here  $a_1$  is the dipole moment of the surface magnetic field, and we take  $I = 10^{45}$  g cm<sup>2</sup> as a typical moment of inertia. The spin evolution of the star determines the velocity of the neutron vortices, according to

$$\mathbf{v}_\perp = -\frac{r_\perp \dot{\Omega}_n}{2\Omega_n} \hat{\mathbf{e}}_{r_\perp}. \quad (6.34)$$

Our code self consistently models the transport of flux tubes according to the velocity field in Equation (6.18), and the cut-through criterion in Equation (6.17).

In Model D1 we use an initial field of strength  $\sim 5 \times 10^{12}$  G at the surface, and  $6.9 \times 10^{12}$  G in the core. We set the initial spin period accordingly to 10.9 ms. We show the results of this simulation in Figure 6.3. In the first 100 kyr the flux is rapidly pushed out of the core at the velocity  $\mathbf{v}_\perp$ . In the outer core the flux tubes are severely deformed, and the tension force  $\mathbf{f}_B$  becomes large enough to cause cut-through in a thin layer beneath the crust. The sharp curvature of poloidal field lines at the base of the crust is site to a strong toroidal current sheet, which generates a quadrupolar toroidal field ( $l = 2$ ) through Hall drift, and rapid Ohmic dissipation of the poloidal field. The expulsion of flux tubes can result in an order of magnitude increase in the poloidal field strength in the outer core.

From this point on, the flux tubes slide vertically along the neutron vortices toward the equator (away from the crust-core interface) with the projected Jones velocity  $(\mathbf{v}_J \cdot \hat{\mathbf{e}}_n) \hat{\mathbf{e}}_n$ . The flux tubes form a “>” shape, with the cusp located along the equator in the outer core. The cusp becomes sharper, until the tension force  $\mathbf{f}_B$  becomes large enough to cut through the vortices, and begins to minimize it at  $\sim 880$  kyr. After  $\sim 1$  Myr, the core operates in the transport regime,

except for a small region around the cusp where the tension force  $\mathbf{f}_B$  is large. The toroidal field oscillates into an octupole configuration ( $l = 3$ ), which is severely damped by Ohmic diffusion. After 2 Myr the crustal poloidal field begins to develop an octupole component, due to the magnetic pressures and tensions communicated from the base of the crust through Ohmic diffusion. This is clearly evident at 4 Myr in Figure 6.3. Throughout this simulation Hall drift does not play a major role in the redistribution of the magnetic field, because the field strength is weak, and Ohmic diffusion is the dominant effect ( $t_{\text{hall}} < t_{\text{ohm}}$ ). The spin period after 4 Myr in this simulation is 0.85 s.

In Model D2 the initial field has strength  $\sim 10^{13}$  G at the surface, and  $1.4 \times 10^{13}$  G in the core. We set the initial spin period accordingly to 21.8 ms, and show the results of this simulation in Figure 6.4. In the first 5 kyr the most of the core operates in the cut-through regime, except for a thin cylinder around the axis of rotation where the vortices move slowly. In the cut-through regime the flux tubes are allowed to bend, and as a result they curve away from the axis of rotation due to the collective drag of vortices cutting through them. After 10 kyr the vortices are moving slowly enough that the core operates in the transport regime, except for a thin layer beneath the crust where the flux tube tension is large. In this thin layer the vortices cut through, and the terminal velocity of flux tubes gets very small due to the high density of flux tubes. The sharp curvature of flux tubes at the crust-core interface results in the development of a strong current sheet in the deep crust, which is site to enhanced Ohmic dissipation, and the development of a quadrupole toroidal field ( $l = 2$ ) through Hall drift.

As the star spins down the number density of vortices decreases along with the critical force  $n_v \tilde{f}_v$ . As a result, after  $\sim 100$  kyr the region of cut-through in the outer core begins to grow, allowing the flux tubes to drift once again back into the core, with the Jones drift velocity  $\mathbf{v}_J$ . The thickness of the cut-through layer increases as the star continues to spin down. After 3 Myr the toroidal field is significantly damped by Ohmic diffusion, and the flux tubes in the core remain curved outward in the outer regions of the core, a result of the collective cut-through by neutron vortices. The spin period after 3 Myr in this simulation is 1.87 s.

In Model D3 we use an initial field of strength  $\sim 2 \times 10^{13}$  G at the surface, and  $\sim 2.7 \times 10^{13}$  G in the core. This field is stronger than previous models, so the star spins down faster, and we set the initial spin period accordingly to 43.5 ms. The results of this simulation are shown in Figure 6.5. In the beginning the vortices cut through in the entire core, except for a thin cylinder around the spin-axis where they are slowly moving. As a result of the vortices cutting through, the flux tubes bend away from the axis of rotation, and bunch in the outer core.

The sharp curvature of poloidal field lines at the crust-core interface is supported by a strong toroidal current sheet. This results in the development on a quadrupole ( $l = 2$ ) toroidal field in the deep crust, and enhanced Ohmic dissipation. As the star spins down the force of vortices pushing on flux tubes becomes smaller while the tension force grows larger. This continues until  $\sim 250$  kyr, when the flux tubes stop moving away from the spin-axis, and begin moving back toward. From this point on, the core mostly operates in the cut-through regime, and the combination of the slow spin period, and strong magnetic field means that the flux cannot be expelled from the core. The flux tubes remain bent away from the spin-axis due to the cut-through of vortices for the remainder of the simulation, while the crustal field decays primarily due to Ohmic diffusion. The spin period after 3 Myr is 4.01 s. The spin periods we observe in this simulations are not unlike the spin periods of known low-B magnetars. However, it seems unlikely that the toroidal field in these models is strong enough to break the crust and power classical magnetar activity.

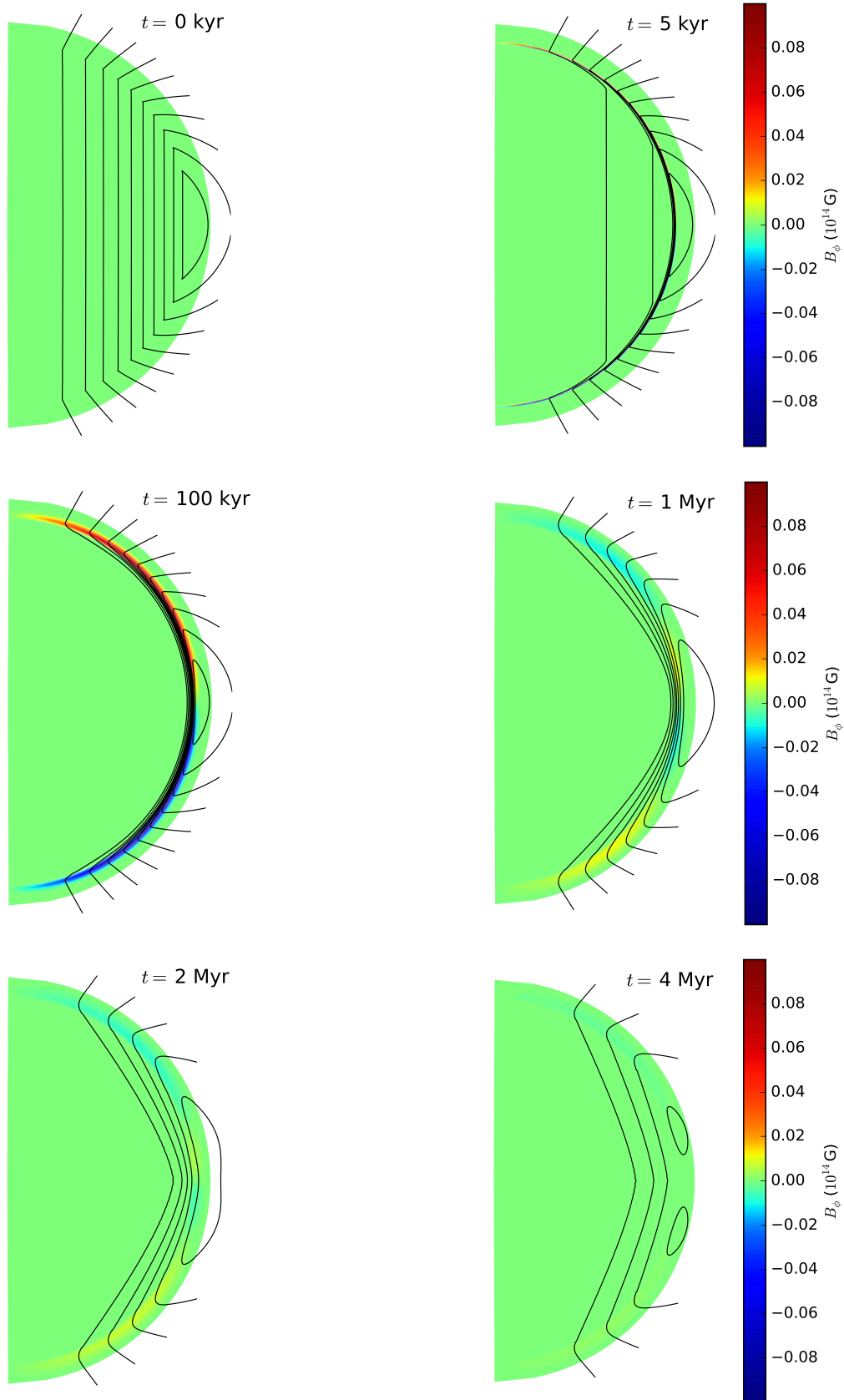


Figure 6.3: Snapshots of the magnetic field evolution for Model D1 (Table 1.1), shown at  $t = 0$  kyr,  $5$  kyr,  $100$  kyr,  $1$  Myr,  $2$  Myr, and  $4$  Myr. The plotting scheme is the same as Figure 4.5.

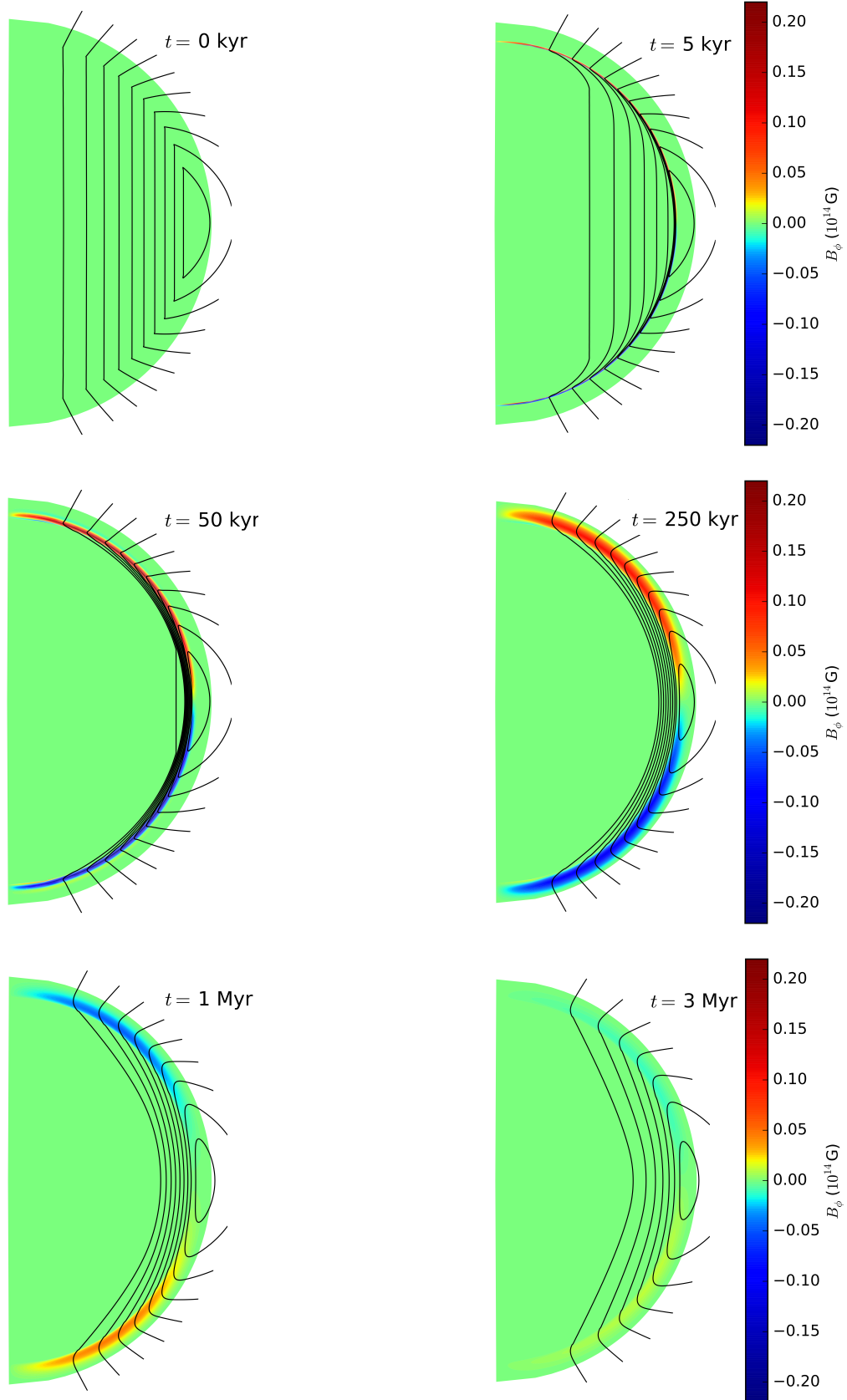


Figure 6.4: Snapshots of the magnetic field evolution for Model D2 (Table 1.1), shown at  $t = 0$  kyr, 5 kyr, 50 kyr, 250 kyr, 1 Myr, and 3 Myr. The plotting scheme is the same as Figure 4.5.

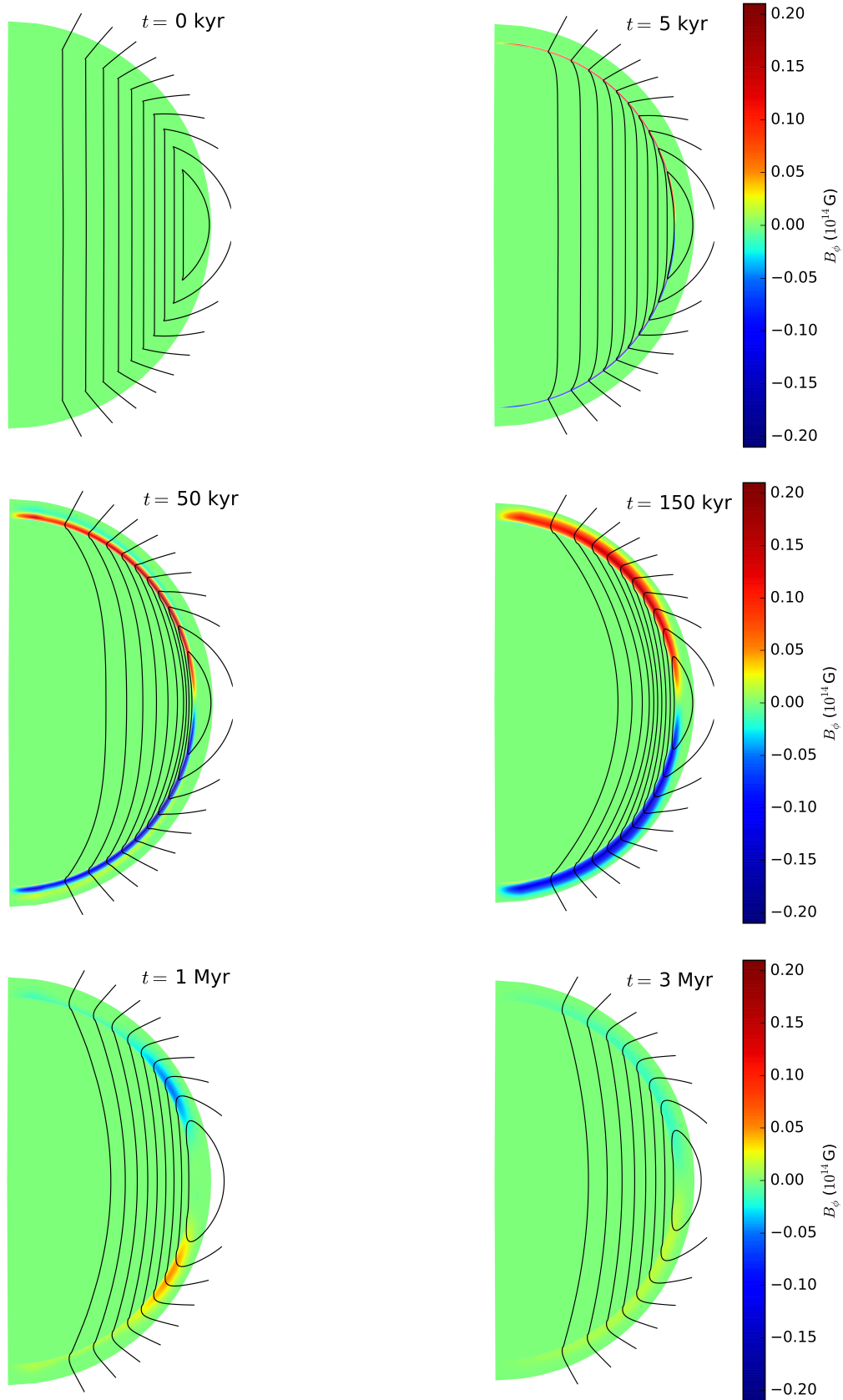


Figure 6.5: Snapshots of the magnetic field evolution for Model D3 (Table 1.1), shown at  $t = 0$  kyr,  $5$  kyr,  $50$  kyr,  $150$  kyr,  $1$  Myr, and  $3$  Myr. The plotting scheme is the same as Figure 4.5.

# Monash University Declaration Chapter 7

## Declaration by candidate:

I declare that my contribution to the work in Chapter 7 that is submitted to the Monthly Notices of the Royal Astronomical Society as [Bransgrove et al. (2017)], involved the following:

The writing of the publication, development of numerical methods including boundary conditions, development of the numerical code, running simulations, and all other work contained therein (that is not referenced otherwise).

Extent of contribution by candidate: 85%

Co-author names: Yuri Levin, Andrei Beloborodov

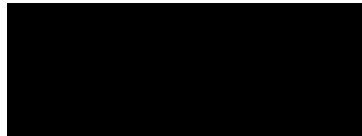
Nature of co-author's contribution: Development of numerical methods including boundary conditions, and feedback during writing of the paper.

I have renumbered sections, equations and figures of the published paper in order to generate a consistent presentation within the thesis. The undersigned hereby certify that the above declaration correctly reflects the nature and extent of the student's and co-authors' contributions to this work.

Candidate Signature:

Date: June 29, 2017

Main Supervisor signature:



Date: June 29, 2017



# Chapter 7

## Magneto-Elastic Evolution of Neutron Star Crusts

Partially adapted from:

*Magnetic Field Evolution of Neutron Stars I: Basic formalism, numerical techniques, and first results*, Ashley Bransgrove, Yuri Levin, and Andrei Beloborodov, 2017, submitted for publication in MNRAS.

## 7.1 Magneto-Elastic Evolution

Lorentz forces generated by Hall drift can deform the neutron star crust, which in turn feeds back into the magnetic field evolution. These crustal deformations consist of an elastic part (thermodynamically reversible), and a plastic part (thermodynamically irreversible). While plastic deformations of the crust are expected to play an important role in strongly magnetized neutron stars (Beloborodov & Levin, 2014), we content ourselves for now with only elastic deformations. In this section we lay out the theory which governs the dynamics of the system, and conclude by presenting the set of coupled magneto-elastic evolution equations. We begin by defining the Lagrangian displacement field of the neutron star crust as

$$\xi(\mathbf{r}, t) \equiv \mathbf{r}' - \mathbf{r}, \quad (7.1)$$

where  $\mathbf{r}$  is the position of a point in the crust before deformation, and  $\mathbf{r}'$  is the position of that point after the deformation. There are two contributions to  $\xi$ ,

$$\xi = \xi_{\text{el}} + \xi_{\text{pl}}. \quad (7.2)$$

Here  $\xi_{\text{el}}$  is the elastic deformation, and  $\xi_{\text{pl}}$  is the plastic deformation. For now we neglect the plastic response of the crust, and content ourselves with the elastic deformation. The equation of motion of the solid crust is then easily derived using Newton's second Law,

$$\rho \frac{\partial^2 \xi_i}{\partial t^2} = \frac{\partial \sigma_{ij}}{\partial x_j} + f_i, \quad (7.3)$$

where  $\rho$  is the mass density,  $\sigma_{ij}$  is the elastic stress tensor, and  $f_i$  is the magnetic part of the Lorentz force which acts on the crust. We restrict ourselves to the regime of linear elastodynamics and only consider small, reversible deformations of the crust. In this framework the stress depends linearly on the displacement, and we may express the elastic stress tensor using Hooke's Law as

$$\sigma_{ij} = c_{ijkl} \epsilon_{kl}, \quad (7.4)$$

with  $c_{ijkl}$  the components of the stiffness tensor, and  $\epsilon_{kl}$  the components of the strain tensor. It has been shown that the speed at which shear waves propagate in a neutron star crust is remarkably constant over its depth Ruderman (1968). We assume  $v_{\text{sh}}$  is constant throughout the crust in our model, so that

$$\mu = \rho v_{\text{sh}}^2 \approx 10^{28} \rho_{12} \text{ erg cm}^{-3}, \quad (7.5)$$

with  $\rho_{12}$  the mass density in units of  $10^{12} \text{ g cm}^{-3}$ . Following the equations of state shown in Chamel & Haensel (2008), we approximate for our convenience  $\log_{10} \rho \propto 8 \log_{10} z$ , which gives the

density scaling in the deep crust as  $\rho \propto z^8$ . Specifically, we choose  $\rho_{12} = 0.5[(1.1r_* - r)/(0.1r_*)]^8$ , which varies from  $1.3 \times 10^{14}$  g cm<sup>-3</sup> at the base of the crust to  $5 \times 10^{11}$  g cm<sup>-3</sup> at the surface, our chosen density cutoff. The corresponding shear modulus profile varies from  $5 \times 10^{27}$  erg cm<sup>-3</sup> at the base of the crust, to  $1.3 \times 10^{30}$  erg cm<sup>-3</sup> at our chosen surface cutoff. We also work in the approximation that the crust is isotropic. The stiffness tensor for an isotropic medium may be written as

$$c_{ijkl} = \lambda \delta_{ij} \delta_{kl} + \mu (\delta_{ik} \delta_{jl} + \delta_{il} \delta_{jk}), \quad (7.6)$$

where  $\lambda$  and  $\mu$  are referred to as the Lamé coefficients. The first term gives rise to compressive deformations which are very difficult to excite with slowly evolving magnetic stresses. We work in the limit of an incompressible crust ( $\lambda \rightarrow 0$  and  $\nabla \cdot \xi = 0$ ). The coefficient of the second term,  $\mu$ , is the shear modulus of the crust. This term leads to transverse elastic modes. The strain tensor is

$$\epsilon_{kl} = \frac{1}{2} (\xi_{k,l} + \xi_{l,k}). \quad (7.7)$$

These definitions of the stiffness and strain tensors may be substituted into the evolution equation (7.3),

$$\rho \frac{\partial^2 \xi_i}{\partial t^2} = \frac{\partial}{\partial x_l} (\mu \xi_{l,i}) + \frac{\partial}{\partial x_l} (\mu \xi_{i,l}) + f_i. \quad (7.8)$$

Upon expansion of these derivatives we obtain

$$\rho \frac{\partial^2 \xi_i}{\partial t^2} = \frac{\partial \mu}{\partial x_l} \frac{\partial \xi_l}{\partial x_i} + \mu \frac{\partial^2 \xi_l}{\partial x_l \partial x_i} + \frac{\partial \mu}{\partial x_l} \frac{\partial \xi_i}{\partial x_l} + \mu \frac{\partial^2 \xi_i}{\partial x_l^2} + f_i. \quad (7.9)$$

Our aim is to recover a vector equation from the above expression. This vector equation will then be studied in the spherical geometry of a neutron star crust. The terms on the right hand side of (7.9) will be considered one at a time. The first term may be expressed more conveniently in vector form if we write it as

$$\frac{\partial \mu}{\partial x_l} \frac{\partial \xi_l}{\partial x_i} = \frac{\partial}{\partial x_i} \left( \xi_l \frac{\partial \mu}{\partial x_l} \right) - \xi_l \frac{\partial}{\partial x_i} \left( \frac{\partial \mu}{\partial x_l} \right), \quad (7.10)$$

by using the product rule in reverse. We now identify this as

$$\frac{\partial \mu}{\partial x_l} \frac{\partial \xi_l}{\partial x_i} = [\nabla(\xi \cdot \nabla \mu) - (\xi \cdot \nabla) \nabla \mu]_i. \quad (7.11)$$

We may change the order of the derivatives in the second term of (7.9), so that

$$\mu \frac{\partial^2 \xi_l}{\partial x_l \partial x_i} = \mu \frac{\partial}{\partial x_i} \left( \frac{\partial \xi_l}{\partial x_l} \right) = [\mu \nabla(\nabla \cdot \xi)]_i = 0. \quad (7.12)$$

This term vanishes because we are working in the limit of an incompressible crust. The third term is expressed as

$$\frac{\partial \mu}{\partial x_l} \frac{\partial \xi_i}{\partial x_l} = [(\nabla \mu \cdot \nabla) \xi]_i. \quad (7.13)$$

The last term is easily written in terms of the vector laplacian,

$$\mu \frac{\partial^2 \xi_i}{\partial x_l^2} = [\mu \nabla^2 \xi]_i. \quad (7.14)$$

So the vector elastodynamic wave equation for an incompressible medium is

$$\rho \frac{\partial^2 \xi}{\partial t^2} = \nabla(\xi \cdot \nabla \mu) - (\xi \cdot \nabla) \nabla \mu + (\nabla \mu \cdot \nabla) \xi + \mu \nabla^2 \xi + \frac{1}{4\pi} (\nabla \times \mathbf{B}) \times \mathbf{B}. \quad (7.15)$$

Assuming a spherically symmetric shear modulus profile yields the elastodynamic wave equation

$$\rho \frac{\partial^2 \xi}{\partial t^2} = (\nabla \mu \cdot \nabla) \xi - (\xi \cdot \nabla) \nabla \mu + \mu \nabla^2 \xi + \frac{1}{4\pi} (\nabla \times \mathbf{B}) \times \mathbf{B}. \quad (7.16)$$

The first three terms on the rhs of (7.16) are due to the elastic restoring forces of the solid crust, and the last term is due to the applied Maxwell stress of the magnetic field. Since in models of Hall drift, the Hall evolution timescale is much longer than the elastic wave crossing time, the inertial term on the lhs of (7.16) may be safely neglected. With the neglect of the inertial terms, magneto-elastic equilibrium is given by

$$\frac{1}{4\pi} (\nabla \times \mathbf{B}) \times \mathbf{B} = -(\nabla \mu \cdot \nabla) \xi + (\xi \cdot \nabla) \nabla \mu - \mu \nabla^2 \xi, \quad (7.17)$$

which is a constraint that must be satisfied throughout the evolution. In the following section we show our own method for ensuring that this equilibrium is satisfied at all times.

## 7.2 A Relaxation Method for Magneto-Elastic Evolution

With the neglect of the inertial term, magneto-elastic equilibrium is given by

$$\frac{1}{4\pi} (\nabla \times \mathbf{B}) \times \mathbf{B} = -(\nabla \mu \cdot \nabla) \xi + (\xi \cdot \nabla) \nabla \mu - \mu \nabla^2 \xi. \quad (7.18)$$

We, however, prefer to deal with an evolution (rather than the above constraint) equation for  $\xi$  and therefore introduce a small non-zero velocity

$$\mathbf{v}_{\text{el}} \equiv \frac{\partial \xi}{\partial t}. \quad (7.19)$$

It corresponds to a small deviation from the force balance that we write in a relaxation/damping form  $\mathbf{f}_{\text{damp}} = -\gamma \rho \mathbf{v}_{\text{el}}$ . The value of  $\gamma$  is not important as long as it is small enough, so that the system evolves while staying very close to the force balance. Effectively, this is a dynamic way of implementing the constraint on  $\xi$  required by the force balance. This yields the evolution equation,

$$\frac{\partial \xi}{\partial t} = \frac{1}{\gamma \rho} [(\nabla \mu \cdot \nabla) \xi - (\xi \cdot \nabla) \nabla \mu + \mu \nabla^2 \xi] + \frac{1}{4\pi \gamma \rho} (\nabla \times \mathbf{B}) \times \mathbf{B}, \quad (7.20)$$

which when evolved in the limit of small  $\gamma$  will tend toward the adiabatic solution. This relaxation method is equivalent to solving a matrix problem to find  $\xi$ , but avoids the difficulty of equations which are implicit in the evolution of  $\mathbf{B}$ . The challenge in choosing the value of  $\gamma$  is on the one hand to ensure the relaxation is fast enough so that the crust is in equilibrium between the magnetic and elastic forces, but on the other hand is slow enough so that the numerical computations do not become too costly. It is helpful to consider the characteristic relaxation timescale

$$\tau_{\text{re}} = \gamma \frac{L^2}{v_{\text{sh}}^2}, \quad (7.21)$$

and require  $\tau_{\text{re}} \ll \tau_{\text{hall}}$ . This gives the criterion

$$\gamma \ll \frac{4\pi n_e e}{B} v_{\text{sh}}^2. \quad (7.22)$$

The back reaction of the crustal motion on the evolution of the magnetic field occurs through the equation

$$\frac{\partial \mathbf{B}}{\partial t} = \nabla \times [(\mathbf{v}_{\text{hall}} + \mathbf{v}_{\text{el}}) \times \mathbf{B}] + \nabla \times (\eta \nabla \times \mathbf{B}). \quad (7.23)$$

### 7.3 Axisymmetric Equations

In axisymmetry the magneto-elastic evolution equations are given as

$$\frac{\partial \Psi}{\partial t} - r^2 \sin^2 \theta \chi (\nabla I \times \nabla \phi) \cdot \nabla \Psi = \frac{c^2}{4\pi \sigma} \Delta^* \Psi, \quad (7.24)$$

$$\frac{\partial I}{\partial t} + r^2 \sin^2 \theta [(\nabla \Omega_e \times \nabla \phi) \cdot \nabla \Psi + I (\nabla \chi \times \nabla \phi) \cdot \nabla I] = \frac{c^2}{4\pi \sigma} \left( \Delta^* I - \frac{1}{\sigma} \nabla I \cdot \nabla \sigma \right), \quad (7.25)$$

with the electron angular velocity

$$\Omega_e = \Omega_{\text{hall}} + \Omega_{\text{el}} = -\frac{j_T}{n_e e r \sin \theta} + \frac{v_{\text{el}}^\phi}{r_\perp} = \chi \Delta^* \Psi + \frac{v_{\text{el}}^\phi}{r_\perp}. \quad (7.26)$$

The elastic evolution of the crust is written in terms of the scalar functions  $\Psi$  and  $I$  as

$$\frac{\partial \xi}{\partial t} = \frac{1}{\gamma \rho} [(\nabla \mu \cdot \nabla) \xi - (\xi \cdot \nabla) \nabla \mu + \mu \nabla^2 \xi] + \frac{1}{4\pi \gamma \rho} \nabla I \cdot (\nabla \Psi \times \nabla \phi) \nabla \phi. \quad (7.27)$$

### 7.4 Numerical Details

In this section we outline the numerical techniques we use to model the magneto-elastic evolution of a neutron star crust. We compute the elastic evolution of the crust through the equation

$$\frac{\partial \xi}{\partial t_{\text{yr}}} = \frac{3.15}{\gamma_{11} \rho_{12}} \left[ (\tilde{\nabla} \mu \cdot \tilde{\nabla}) \xi - (\xi \cdot \tilde{\nabla}) \tilde{\nabla} \mu + \mu \tilde{\nabla}^2 \xi \right] + \frac{10^6}{\gamma_{11} \rho_{12}} (\tilde{\nabla} \times \mathbf{B}_{14}) \times \mathbf{B}_{14}, \quad (7.28)$$

where we have normalized  $t_{\text{yr}} = t/3.15 \times 10^7$  s,  $\gamma_{11} = \gamma/10^{11}$  s<sup>-1</sup>,  $\rho_{12} = \rho/10^{12}$  g cm<sup>-3</sup>,  $\mathbf{B}_{14} = \mathbf{B}/10^{14}$  G,  $\tilde{\nabla}$  is the del operator with lengths normalized to  $10^6$  cm, and  $\xi$  is in cm. The derivatives are evaluate using the difference formula in Equations (3.39), (3.40), (3.41), and (3.42). In Model E the toroidal field is zero at the surface of the crust and at the base, so the shear stress must be zero there. That is, the traction component of the stress tensor must be zero. In spherical coordinates this is

$$\sigma_{r\phi} = \frac{1}{2} \left( \frac{\partial \xi_\phi}{\partial r} - \frac{\xi_\phi}{r} \right) = 0, \quad (7.29)$$

[e.g. Landau & Lifshitz (1970)]. This gives a boundary condition for the gradient of  $\xi_\phi$  at the base and surface of the crust,

$$\left. \frac{\partial \xi_\phi}{\partial r} \right|_{r=r_c} = \frac{\xi_\phi(r_c)}{r}, \quad (7.30)$$

$$\left. \frac{\partial \xi_\phi}{\partial r} \right|_{r=r_*} = \frac{\xi_\phi(r_*)}{r}. \quad (7.31)$$

We set ghost cells accordingly. For cases when the toroidal field is non-zero it is trivial to include the relevant component of the Maxwell tensor in the boundary condition. The boundary conditions on  $\xi_\phi$  at the poles are set according to axisymmetry,

$$\xi_\phi^{j1-1} = -\xi_\phi^{j1+1} \quad (7.32)$$

$$\xi_\phi^{j2+1} = -\xi_\phi^{j2-1}. \quad (7.33)$$

We identify the elastic deformation velocity as

$$\mathbf{v}_{\text{el}}^\phi = \frac{1}{3.15 \times 10^7} \frac{\partial \xi_\phi}{\partial t_{\text{yr}}}. \quad (7.34)$$

We evaluate the angular velocity of the crustal deformation as

$$\Omega_{\text{el}} = \frac{\mathbf{v}_{\text{el}}^\phi}{r \sin \theta}. \quad (7.35)$$

In order to advance the toroidal field evolution Equation (7.25), we must set ghost cells for  $\Omega_{\text{el}}$ , so that we can evaluate its derivatives. The gradient of  $\Omega_{\text{el}}$  is fixed at the surface and the base of the crust by the boundary condition on  $\xi_\phi$ . We can see this by rewriting the traction in the form

$$\sigma_{r\phi} = \frac{r \sin \theta}{2} \frac{\partial}{\partial r} \left( \frac{\xi_\phi}{r \sin \theta} \right) = 0, \quad (7.36)$$

then taking a time derivative of both sides yields the gradient conditions

$$\left. \frac{\partial \Omega_{\text{el}}}{\partial r} \right|_{r=r_c} = 0, \quad (7.37)$$

$$\left. \frac{\partial \Omega_{\text{el}}}{\partial r} \right|_{r=r_*} = 0. \quad (7.38)$$

Derivatives of  $\Omega_{\text{el}}$  can then be taken using the formula in Equations (3.39) and (3.41), and used to advance the Equation (7.25). The crustal deformation enters the magnetic field evolution through

$$\frac{\partial \mathbf{B}_{14}}{\partial t_{\text{yr}}} = -6.25 \times 10^{-7} \tilde{\nabla} \times \left( \frac{\tilde{\nabla} \times \mathbf{B}_{14}}{n_{e,0}} \times \mathbf{B}_{14} \right) - 1.25 \times 10^{-8} \tilde{\nabla} \times \left( \frac{\tilde{\nabla} \times \mathbf{B}_{14}}{\sigma_0} \right) + 31.5 \tilde{\nabla} \times (\mathbf{v}_{\text{el}} \times \mathbf{B}_{14}), \quad (7.39)$$

with the usual normalizations. In Model E we fix all components of the magnetic field at the base of the crust. The azimuthal component is fixed by hydromagnetic equilibrium to be

$$B_\phi(r_c) = \frac{I(r_c)}{r_c \sin \theta} = 0. \quad (7.40)$$

The radial component  $B_r$  is fixed at the crust-core interface by setting

$$\Psi_{\text{crust}}(r_c) = \Psi_{\text{core}}(r_c), \quad (7.41)$$

which fixes  $\partial \Psi / \partial \theta$ , and hence  $B_r$ . The component  $B_\theta$  is fixed at  $r_c$  by setting

$$\left. \frac{\partial \Psi}{\partial r} \right|_{r=r_c}(t) = \left. \frac{\partial \Psi}{\partial r} \right|_{r=r_c}(t=0), \quad (7.42)$$

which we enforce by setting the appropriate ghost cells. For more details of the numerical method we refer the reader to Appendix B.

## 7.5 Results

In this section we present the coupled evolution of the elastic crustal deformation, and the magnetic field under Hall drift and Ohmic diffusion. The initial magnetic field is chosen such that there is a sharp cusp in the field on the crust-core interface. [Goldreich & Reisenegger \(1992\)](#) showed that such a disturbance will launch circularly polarized ‘‘Hall waves’’, which can propagate from the crust-core interface, and transport magnetic energy toward the surface of a neutron star. [Beloborodov & Levin \(2014\)](#) showed that Hall waves in strong magnetic fields can trigger a thermoplastic instability in the crust, which can generate X-ray activity associated with magnetars. The elastic deformation of the crust can be significant in the upper layers, where the magnetic energy density  $\mu_B = B_z^2 / 8\pi$  is comparable to the crustal shear modulus  $\mu$ . Here the crust cannot balance arbitrary stresses generated by Hall drift, so it yields, thus nullifying the Hall effect. In their 1D plane parallel model, [Cumming et al. \(2004\)](#) show that the Hall term in the Hall-elastic evolution equation is suppressed by a factor  $(1 + \mu_B / \mu)^{-1}$ , so that

when  $\mu_B \gg \mu$ , Hall drift is significantly suppressed. Unfortunately in this regime ( $\mu_B \gg \mu$ ), we encounter severe numerical instabilities due to our explicit time integrator. Thus, for now we are restricted to work in the limit  $\mu_B \leq \mu$ , where we may still demonstrate the effectiveness of the relaxation method outlined in this Chapter. In this regime the Equations (7.20) and (7.23) are weakly coupled.

In Model E we chose the initial field to be purely poloidal, with vertical field lines (pure  $B_z$ ) in the core (in particular  $\Psi \propto r_\perp^2$ ), with a dipole potential field in the crust. The initial field has strength  $B \approx 2 \times 10^{14}$  G. There are several physical processes which could cause such a cusp at the crust-core interface in a highly magnetized neutron star, and these motivate our choice of initial field. As demonstrated in Chapter 6, if the magnetic field is sufficiently weak, superfluid neutron vortices will be present for a significant period during the spin down of a rapidly rotating neutron star, while the ratio of rotational to magnetic energy is high. Transport of flux tubes by outward moving vortices can result in a cusp in the field at the base of the crust, though this will not result in vertical field lines in the core as shown above. Jones flux tube drift in a young magnetar can result in a cusp in the field, and could launch Hall waves, depending on the composition of the core and the subsequent value of the drag coefficient  $\alpha$ . The launching of short wavelength Hall waves depends on Jones drift being significantly faster than the Hall timescale. There may be other effects which could drive a fast change of the core magnetic field, and thus launch the Hall waves. [Beloborodov & Li \(2016\)](#) found that in young magnetars with hot cores ( $T_{\text{core}} \approx 10^9$  K) and ultra-strong magnetic fields ( $B \gtrsim 10^{16}$  G), ambipolar diffusion operates in the friction dominated regime, and may cause a fast rearrangement of the core magnetic field. Additionally there may be hydromagnetic instabilities in young magnetars which can result in a rapid rearrangement of the core magnetic field.

The magneto-elastic evolution is seen in Figure 7.1. Initially, the cusp in the poloidal field generates strong toroidal currents which in turn generate toroidal field. The result is a burst of Hall waves which propagate away from the core. These waves are the 2D analogue of the Hall waves shown in [Li et al. \(2016a\)](#). At 3 kyr the small amplitude, short wavelength Hall waves, have traveled the furthest toward the stellar surface. The long wavelength Hall waves near the core evolve much more slowly. This can be understood if we consider our system as a constant background field, with an oscillating perturbation which is linear in the field. This is valid because the Hall waves are sufficiently weak that evolution equation for the poloidal field is weakly coupled to the toroidal field, meaning that the structure of the poloidal field is effectively constant. Here we understand the background field to be poloidal, and the perturbation is the Hall waves, early in the evolution before non-linearity becomes significant. The dispersion

relation is

$$\omega = \frac{ck|\mathbf{k} \cdot \mathbf{B}_0|}{4\pi n_e}, \quad (7.43)$$

(Goldreich & Reisenegger, 1992) where  $\mathbf{k}$  is the wave vector,  $k := |\mathbf{k}|$ , and  $B_0$  a uniform background magnetic field. The waves are seen to fan out from the crust-core interface over the next few kyr, traveling furthest near the poles. This is due to the geometry of the existing background field. The group velocity of Hall waves in the linear regime follows from the dispersion relation (Goldreich & Reisenegger, 1992) as

$$v_{\text{gp}} = \pm \frac{ck(\mathbf{B}_0 + (\hat{\mathbf{k}} \cdot \mathbf{B}_0)\hat{\mathbf{k}})}{4\pi n_e e}, \quad (7.44)$$

where  $\hat{\mathbf{k}} := \mathbf{k}/k$ . Near the poles, the background field is almost pure  $B_r$ , so the waves travel radially there. However, near the equator, the background field is almost entirely  $B_\theta$ , so there is less radial propagation. After the first 6 kyr the waves begin to evolve non-linearly. Hall drift sets in and advects the wave fronts toward the equator of the star. But due to the gradient in electron density, and the fanning of the wave fronts, they are advected non-uniformly, and start to break apart. Diffusion also smears the wave fronts, and decreases the amplitude. The evolution of the crustal displacement is shown in Figure 7.2. The displacement is largest near the surface, where the shear modulus is smallest and the crust yields easily. The crustal displacement reaches a maximum amplitude of  $\sim 2$  m.

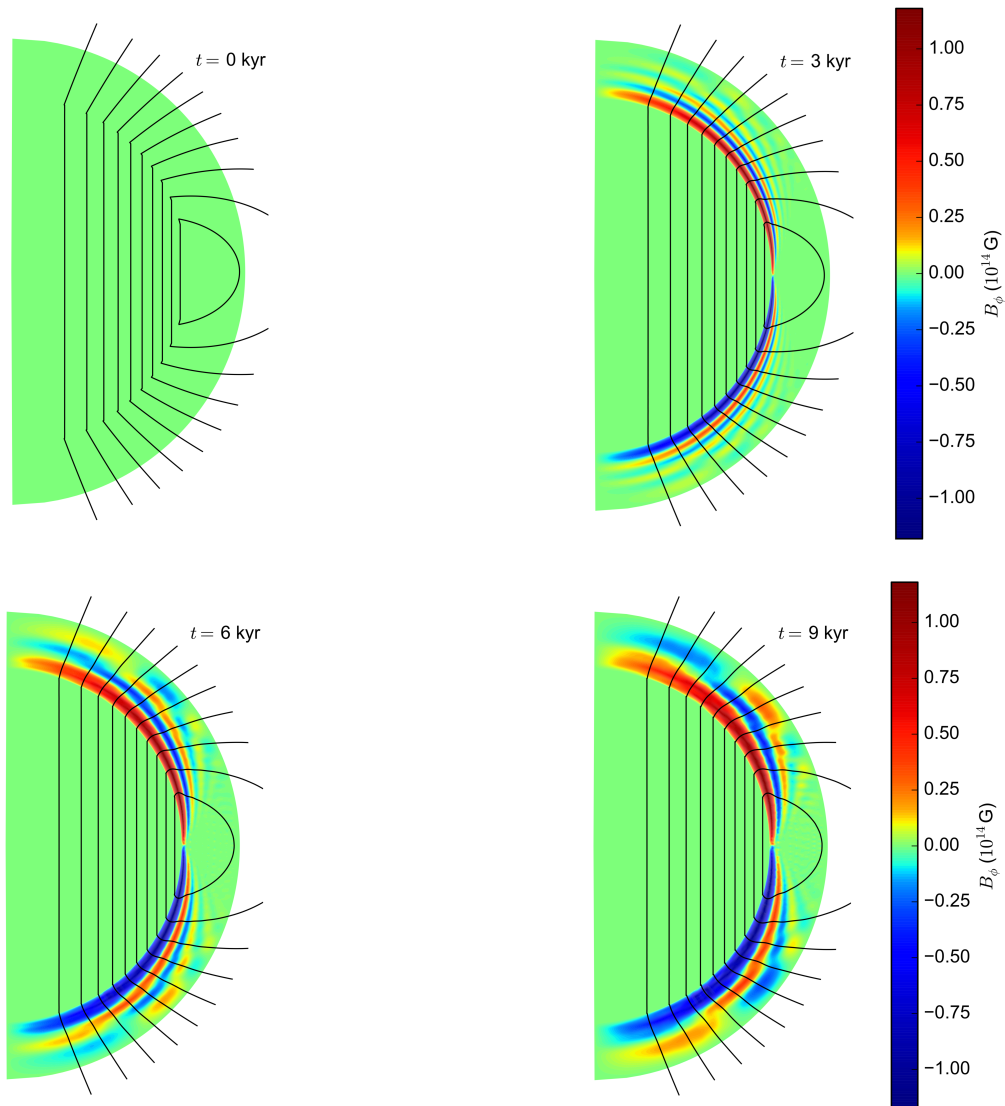


Figure 7.1: Snapshots of the magnetic field evolution for Model E (Table 1.1), shown at  $t = 0$  kyr, 3 kyr, 6 kyr, and 9 kyr. The plotting scheme is the same as Figure 4.5. The thickness of the crust has been magnified by a factor of 2.5.

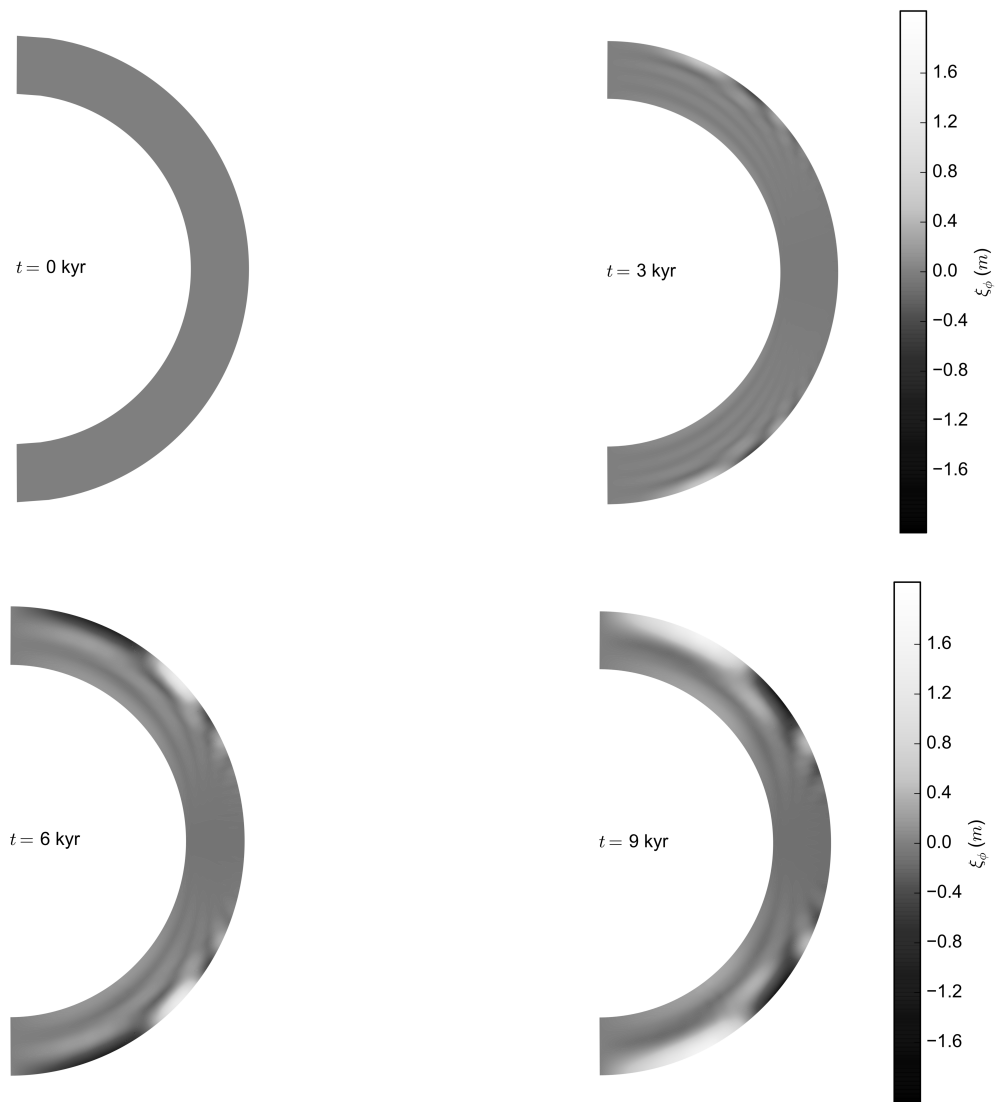


Figure 7.2: Snapshots of the Lagrangian displacement of the crust ( $\xi_\phi$ ) for Model E (Table 1.1), shown at  $t = 0$  kyr, 3 kyr, 6 kyr, and 9 kyr. The color scale varies logarithmically, with a linear region around zero. The thickness of the crust has been magnified by a factor of 2.5.

## Monash University Declaration Chapter 8

### Declaration by candidate:

I declare that my contribution to the work in Chapter 8 that is submitted to the Monthly Notices of the Royal Astronomical Society as [Bransgrove et al. \(2017\)](#), involved the following:

The writing of the publication, and all other work contained therein (that is not referenced otherwise).

Extent of contribution by candidate: 85%

Co-author names: Yuri Levin, Andrei Beloborodov

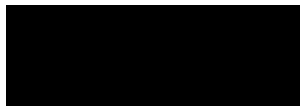
Nature of co-author's contribution: Feedback during writing of the paper.

I have renumbered sections, equations and figures of the published paper in order to generate a consistent presentation within the thesis. The undersigned hereby certify that the above declaration correctly reflects the nature and extent of the student's and co-authors' contributions to this work.

Candidate Signature:

Date: June 29, 2017

Main Supervisor signature:



Date: June 29, 2017

# Chapter 8

## Discussion

Partially adapted from:

*Magnetic Field Evolution of Neutron Stars I: Basic formalism, numerical techniques, and first results*, Ashley Bransgrove, Yuri Levin, and Andrei Beloborodov, 2017, submitted for publication in MNRAS.

In this thesis we have modeled the coupled magnetic field evolution of neutron stars in the crust and the core. In the crust we include evolution due to Hall drift and Ohmic diffusion (Goldreich & Reisenegger, 1992), as well as the elastic response of the solid crust. We enforce the correct hydromagnetic equilibrium in the fluid core. We also explore the effects of the Jones flux tube drift (Jones, 2006), and expulsion by superfluid neutron vortices during spin-down [Ruderman & Sutherland (1974), Srinivasan et al. (1990), Ruderman et al. (1998)]. In this section we discuss the implications of these results, in the context of the galactic population of neutron stars, and their observable behavior.

In Chapter 4 we modeled the evolution of an initial poloidal field with broken equatorial symmetry. We evolved the crustal magnetic field through Hall drift and Ohmic diffusion, while the core field evolved according to the hydromagnetic equilibrium we formulate in Chapter 4. We confirm the Hall attractor of Gourgouliatos & Cumming (2014) for B-fields which penetrate the core, while satisfying the correct hydromagnetic equilibrium.

In Chapter 5, we present simulations of Jones flux tube drift, which show that the B-field in the core can straighten under the enhanced self tension possessed by the quantized flux tubes. The straightening of flux tubes is associated with the dissipation of free energy stored in the curvature of the field. This straightening occurs on a timescale

$$\tau_{\text{diss}} \sim 450 \left( \frac{n_e}{3.5 \times 10^{37} \text{ cm}^{-3}} \right)^2 \left( \frac{10^{29} \text{ s}^{-1}}{\tilde{\sigma}} \right) \text{ kyr}, \quad (8.1)$$

but can occur significantly faster depending on the value of  $\tilde{\sigma}$ . Interestingly this can generate a burst of activity in highly magnetized neutron stars which were previously in the Hall attractor state. Importantly, we show that for the range of values of  $\tilde{\sigma}$  estimated by Jones (2006),  $\tau_{\text{diss}}$  is always much smaller than the modified Ohmic timescale [Equation (5.73)], so that the Ohmic timescale governs the rate of depletion of the global magnetic field. However this timescale is very different to the Ohmic timescale of Goldreich & Reisenegger (1992).

The timescale for depleting the pulsar magnetic fields in these simulations is very sensitive to the choice of electrical conductivity, and it is worth while to discuss the implications of this. Phonon scattering, and impurity scattering are the main ways currents can be diffused in a neutron star crust. Phonon scattering is exponentially suppressed when  $T < T_U = 8.7 \times 10^7$  K  $\rho_{14}(Y_e/0.05)(Z/30)^{1/3}$  [Gnedin et al. (2001), Cumming et al. (2004)], and the Umklapp processes freeze out. Impurity scattering is dominant at low temperatures ( $T < T_U$ ), or high impurity levels. Estimates of the impurity levels in the deep crust range from  $Q_{\text{imp}} \approx 10^{-3}$  (Flowers & Ruderman, 1977), to  $Q_{\text{imp}} \approx 10$  (Jones, 2001). For young or accreting pulsars,

with temperatures  $T \gtrsim 10^8$  K (Brown & Bildsten, 1998),  $T > T_U$ , and typical impurity levels, phonon scattering will be dominant in the deep crust. The timescale for flux to diffuse through the crust, using the electrical conductivity in Chapter 3 (phonon scattering at  $T \approx 2 \times 10^8$  K), our modified Ohmic timescale Equation (5.73) yields  $\tau_{\text{Ohm}} \sim 150$  Myr. A full treatment would include the effects of accretion onto the neutron star surface, and burial of the magnetic field. The consequences of this are not clear, but it should be noted that burial of the field [see eg. Choudhuri & Konar (2002) and the field configurations therein] could result in suppression of the factor  $B_z/B_x$  in the modified ohmic timescale [Equation (5.73)], and an even shorter timescale for the depletion of the global field. Pons et al. (2009) found that Ohmic dissipation proceeds faster when thermal feedback on the crustal conductivity is included. This could further shorten the timescale of 150 Myr we observe in our simulations.

After a young pulsar has cooled, or accretion has subsided, the neutron star crust will cool. For  $T \sim 10^6$  K,  $T < T_U$ , and impurity scattering will dominate. When impurity scattering is dominant, the electrical conductivity in the deep crust is

$$\sigma_Q = 4.4 \times 10^{25} \text{ s}^{-1} (\rho_{14}^{1/3}/Q_{\text{imp}})(Y_e/0.05)^{1/3}(Z/30). \quad (8.2)$$

[Baiko & Yakovlev (1995), Baiko & Yakovlev (1996), Cumming et al. (2004)]. In the impurity dominated regime, the timescale for flux to diffuse through the crust is

$$\tau_{\text{ohm}} \sim hl \frac{4\pi\sigma_Q}{c^2} \frac{B_z}{B_x} = \frac{1.8 \text{ Gyr}}{Q_{\text{imp}}}, \quad (8.3)$$

meaning that flux is effectively frozen into the crust, and the dipole surface field of the pulsar will no longer decay. For any impurity parameter which yields a decay time comparable to the Hubble time ( $Q_{\text{imp}} \lesssim 0.13$ ), the field will be approximately stable. This could explain the persistence of magnetic fields in millisecond pulsars, after periods of rapid depletion at higher temperatures. Alternatively, if impurity levels are much higher, as suggested by Jones (2001), then Ohmic diffusion can proceed rapidly in pulsars even after cooling, so that the crust cannot prevent decay of the dipole field. This would suggest that something elsewhere, in the core was inhibiting the motion of flux.

In the core flux tubes may get caught on magnetized neutron vortices, and be forced to move outward at the same rate. The vortices move outward at a timescale equal to the spin down time of the star, which is very long for millisecond pulsars. Jones (2006) also found that while the outer core is likely be a type-II superconductor, protons in the inner core may be type-I. In type-I superconductors magnetic flux is confined to macroscopic filaments of normal matter. Due to the presence of muons in the inner core in some equations of state, motion of

the filaments would be accompanied by the formation of large gradients in chemical potential, limiting the motion of flux to the rate set by weak nuclear interactions (Jones, 2006). Additionally our simulations do not include a smooth transition from the solid crust to the liquid core. It is possible that some flux tubes get pinned in the pasta phases at the crust core interface, thus causing a remnant field to be left behind. Any of these could provide an explanation for the persistence of a magnetic field in millisecond pulsars despite the decay time we calculate.

In Chapter 6 we modeled the expulsion of flux from the core by the outward motion of neutron vortices during spin-down. We chose the initial spin period for our models by assuming the star was born with a 1 ms spin period, and allowed to spin down for 300 years before the phase transition to superfluidity, as suggested by the Cas A remnant [Shternin et al. (2011), Page et al. (2011)]. Models D1, D2, and D3 have typical magnetic field strengths of  $5 \times 10^{12}$  G,  $10^{13}$  G, and  $2 \times 10^{13}$  G respectively.

While Ruderman et al. (1998) argues that flux tube tension is small compared to the critical force  $n_v f_v$ , we find that it plays a crucial role in rearranging flux tubes in the core — even for weaker magnetic fields  $\lesssim 5 \times 10^{12}$  G. This is because the transport of flux tubes by vortices results in the formation of sharp magnetic features, which possess enormous tension, particularly in the outer core, where flux tubes are anchored to the crust. Even in regions where the tension force  $\mathbf{f}_B$  is small, it causes the flux tubes to slide along neutron vortices, and plays an important role in the large scale distribution of flux. We found that when  $B \gtrsim 2 \times 10^{13}$  G, the combination of the strong magnetic field and the slower spin period, means that the magnetic field could not be expelled from the core. On the other hand, we found that for  $B \lesssim 10^{13}$  G, the outward motion of vortices resulted in a partial expulsion of the core magnetic field, into the outer core and deep crust. We find that in all simulations, as the field is pushed away from the spin-axis a toroidal field grows in the deep crust.

When the flux is expelled into the outer core regions, a strong toroidal current sheet develops in the deep crust. These currents drive Ohmic dissipation at an enhanced rate, as compared to core-penetrating fields which vary on larger spatial scales. Additionally, the bunching of flux tubes in the outer core means the poloidal field can be an order of magnitude stronger there, compared to the spin-down inferred dipole field strength. At some stages in our simulations the field configurations loosely resemble the crust-confined fields of Pons & Geppert (2007), so we may expect thermal emission similar to that in their crust-confined models. The crucial difference is that in our simulations the field penetrates the core. It seems unlikely that flux expulsion could power the magnetar activity of weak-field magnetars or high-B pulsars since

the toroidal field is always  $< 10^{14}$  G. However, it is possible that flux expulsion could power thermal emission in isolated neutron stars, due to enhanced Ohmic dissipation in the deep crust.

A shortcoming is that we have not resolved the controversy in the literature between the timescales of [Jones \(2006\)](#) and [Glampedakis et al. \(2011\)](#), and this is left for future work. This thesis is using the drift timescales derived by Jones, as they lead to interesting dynamical effects at the crust-core interface that are well-modeled in our numerical experiments. A full treatment would include other effects, such as thermal creep. We also point out that a dipole which is misaligned from the axis of rotation violates axisymmetry, so a full 3D treatment is required for this problem, and could lead to very different field configurations in the core.

In this thesis we have numerically modeled the effects of Hall drift, Ohmic diffusion, and the magnetically induced elastic back-reaction on the crustal magnetic field of a neutron star. We formulate the correct hydromagnetic equilibrium to ensure dynamical stability of the core field on long timescales. We use this to magnetically couple the crust and the core in all of our simulations. We confirm the Hall attractor of [Gourgouliatos & Cumming \(2014\)](#) for B-fields which penetrate the core. We model a core evolving in accordance with Jones flux tube drift ([Jones, 2006](#)). The combination of Jones flux tube drift in the core, and Ohmic diffusion in a hot crust ( $T \sim 2 \times 10^8$  K), can deplete pulsar magnetic fields on a timescale of 150 Myr. We model the expulsion of flux from the core by superfluid neutron vortices during the spin-down of a newborn rapidly rotating pulsar. This can result in the partial expulsion of flux from the core when  $B \lesssim 10^{13}$  G, and could power thermal emission in isolated neutron stars. Future work will include the effects of field burial by accretion, and a detailed study of the galactic population of pulsars.



# Appendix A

## Twist Evolution of the Core.

The Hall evolution of  $B_\phi$  in the crust can be written as

$$\frac{\partial B_\phi}{\partial t} = -\nabla_p \cdot (B_\phi \mathbf{v}_p) + (r_\perp \mathbf{B}_p \cdot \nabla_p) \left( \frac{v_\phi}{r_\perp} \right), \quad (\text{A.1})$$

with  $\mathbf{v}_p$  and  $v_\phi$  the poloidal and toroidal parts of the Hall drift velocity, and we have defined the poloidal differential operator

$$\nabla_p \equiv \left( \frac{\partial}{\partial r_\perp}, \frac{\partial}{\partial z} \right), \quad (\text{A.2})$$

using cylindrical coordinates  $(r_\perp, z)$ . The first term on the rhs of (A.1) represents advection of  $B_\phi$  by poloidal velocities, and the second term represents shearing of poloidal field lines in the azimuthal direction. By using a combination of the product rule and the divergence constraint, (A.1) can be written in conservative form as

$$\frac{\partial B_\phi}{\partial t} + \nabla_p \cdot \mathbf{F}_{\text{hall}} = 0, \quad (\text{A.3})$$

where we identify the Hall advection flux

$$\mathbf{F}_{\text{hall}} = B_\phi \mathbf{v}_p - v_\phi \mathbf{B}_p. \quad (\text{A.4})$$

It is convenient to work in the so-called flux-coordinates  $(\Psi, \lambda, \phi)$ , where  $\Psi$  labels surfaces of constant poloidal flux, and  $\lambda$  is the length along a given poloidal field line in the  $\phi = \text{const}$  plane [e.g. [Goedbloed et al. \(2010\)](#)]. At the base of the crust the boundary condition is  $f_\phi = \mathbf{j}_p \times \mathbf{B}_p / c = 0$ , which implies  $\mathbf{v}_p \parallel \mathbf{B}_p$ . So the Hall flux can be written in flux coordinates as

$$\mathbf{F}_{\text{Hall}} = B_\phi |\mathbf{v}_p| \hat{e}_\lambda - v_\phi |\mathbf{B}_p| \hat{e}_\lambda = (B_\phi v_\lambda - v_\phi B_\lambda) \hat{e}_\lambda = F_\lambda \hat{e}_\lambda, \quad (\text{A.5})$$

where  $\mathbf{B}_p = B_\lambda \hat{e}_\lambda$ , and  $\mathbf{v}_p = v_\lambda \hat{e}_\lambda$  at the base of the crust. Then, using the scale factors for flux-coordinates

$$h_\Psi = \frac{1}{r_\perp B_\lambda}, \quad h_\lambda = 1, \quad (\text{A.6})$$

we may write the conservation equation for  $B_\phi$  in flux coordinates as,

$$\frac{\partial B_\phi}{\partial t} = -r_\perp B_\lambda \frac{\partial}{\partial \lambda} \left( \frac{F_\lambda}{r_\perp B_\lambda} \right). \quad (\text{A.7})$$

Rearranging and integrating both sides with respect to  $\lambda$  yields an evolution equation for the twist of the core magnetic field

$$\frac{\partial \zeta(\Psi)}{\partial t} = -[J(\Psi, \lambda_2) - J(\Psi, \lambda_1)], \quad (\text{A.8})$$

where we have identified the twist angle

$$\zeta(\Psi) = \int_{\lambda_1}^{\lambda_2} d\lambda \left( \frac{B_\phi}{r_\perp B_\lambda} \right), \quad (\text{A.9})$$

and the “flux of twist” into/out of the core as

$$J = \frac{F_\lambda}{r_\perp B_\lambda} = \frac{v_\lambda B_\phi}{r_\perp B_\lambda} - \frac{v_\phi}{r_\perp}. \quad (\text{A.10})$$

# Appendix B

## The Code

We evolve the poloidal and toroidal scalar functions on a discrete grid, which is linear in  $r$  and  $u \equiv \cos\theta$ , in the crust and the core. The variable  $u$  varies from -1 at the south pole, to 1 at the north pole, and the radius of the star is  $r_* = 1$  in units of  $10^6\text{cm}$ . The crust core interface is at  $r_c = 0.9r_*$ . We use the indices  $i$  and  $j$  to specify grid points in the  $r$  and  $u$  directions respectively. In most simulations the index  $j$  varies from  $j_1 = -50$  corresponding to the south pole, to  $j_2 = 50$  corresponding to the north pole, with  $j = 0$  defining the equator. We choose the difference in  $u$  such that  $\delta u = 2/(j_2 - j_1)$ . The index  $i$  varies from  $i_0 = 0$  at the center ( $r = 0$ ), to typical values of  $i_c = 400$  at the crust core interface ( $r = r_c$ ) depending on the simulation. Throughout the crust and the last few rows of the core (ghost points for the crust) the radial grid spacing is  $\delta r_{\text{crust}} = 1/i_s$ . The radial grid spacing in the outer few rows of the core grid matches the radial grid spacing of the crust, for ease of implementing boundary

Table B.1: The grid resolution used in the crust and core for each of the Models A-E.

| Model | Crust ( $N_r \times N_u$ ) | Core ( $N_r \times N_u$ ) |
|-------|----------------------------|---------------------------|
| A     | (100 × 133)                | (400 × 133)               |
| B     | (100 × 101)                | (400 × 101)               |
| C     | (100 × 201)                | —                         |
| D1    | (100 × 101)                | (700 × 101)               |
| D2    | (100 × 101)                | (700 × 101)               |
| D3    | (100 × 101)                | (700 × 101)               |
| E     | (500 × 201)                | —                         |

conditions on the crustal field. In order to avoid numerical instabilities near the poles in some simulations, we added adjustable patches of increased resolution in the  $u$  direction. Depending on the magnetic field structure, angular resolution was some times set to 3 times the original resolution near the poles in order to obtain convergence. This resolved the issue, and added little expense to the computations.

We use a variable time step, which shrinks in order to avoid instability in the evolution. Because we are evolving magnetic fields and crustal displacements with a variety of evolution equations, we calculate a stable time step for each evolution equation. For the Hall effect [Equations (3.20) and (3.21)], we use the fastest electron velocity in the grid to limit the maximum time step, using

$$\delta t_{\text{hall}} = k_c \frac{4\pi n_e e}{c} \frac{\delta r \delta \mu}{|\nabla \times \mathbf{B}_T|}, \quad (\text{B.1})$$

with  $k_c$  a Courant parameter. For Ohmic diffusion [rhs of Equations (3.20) and (3.21)], we use

$$\delta t_{\text{ohm}} = k_c \frac{\delta r^2}{\eta} = k_c \frac{4\pi \sigma \delta r^2}{c}, \quad (\text{B.2})$$

which is minimized by choosing the smallest conductivity. For the elastic relaxation [Equation (7.20)] we use the time step

$$\delta t_{\text{el}} = k_c \gamma \frac{\delta r^2}{v_{\text{sh}}^2}. \quad (\text{B.3})$$

For the hydromagnetic relaxation Equation (4.14) we choose the diffusion time step

$$\delta t_{\text{hme}} = k_c \frac{\delta r^2}{k}. \quad (\text{B.4})$$

The stable time step for Jones drift [Equation (5.59)] is chosen using the maximum flux tube velocity on the computational grid,

$$\delta t_{\text{Jones}} = k_c \frac{\delta r \delta \mu}{\max|\mathbf{v}_J|}, \quad (\text{B.5})$$

and similarly with the spin-down transport of flux [Equation (6.24)]

$$\delta t_{\text{sd}} = k_c \frac{\delta r \delta \mu}{\max|\mathbf{v}_{\text{sd}}|}. \quad (\text{B.6})$$

In all of the above, the Courant parameter  $0 < k_c < 1$  is chosen so that such that we observe convergence and stability. At each time step, we evaluate the rhs of the evolution equations using the difference formulae above, then use Euler integration with the smallest time step

$$\delta t = \min\{\delta t_{\text{hall}}, \delta t_{\text{ohm}}, \delta t_{\text{el}}, \delta t_{\text{hme}}, \delta t_{\text{Jones}}, \delta t_{\text{sd}}\}, \quad (\text{B.7})$$

to advance the functions  $\Psi$  and  $I$  to  $t + \delta t$ .

In Model A we choose the relaxation parameter  $k = 2 \times 10^{-6} \text{ cms}^{-1}$  In Model E we choose the parameter  $\gamma = 1 \times 10^{16} \text{ s}^{-1}$ .

In the core we treat coordinate singularities along the pole, and at the origin by freezing in the magnetic field beyond some flux surface  $\Psi_0$ , so that the magnetic field is unevolving very close to the pole. This is done by multiplying the velocity fields in Equations (4.14) (5.59) and (6.24) by the function

$$s(\Psi) = \frac{1}{\exp[-a(\Psi - \Psi_0)] + 1}, \quad (\text{B.8})$$

which behaves like a smoothed step function. The parameter  $c$  is chosen to make the step as steep as possible while still being resolved by the grid mesh. In Model A we also add a term to the rhs of Equation (4.14),

$$-\frac{1}{\tau} \frac{I(r, \theta)}{\exp[b(\Psi - \Psi_0)] + 1}, \quad (\text{B.9})$$

to ensure that any toroidal field beyond  $\Psi_0$  is exponentially reduced on the timescale  $\tau$ . Our results are not sensitive to these methods, so long as  $\Psi_0$  is close to the pole.

We have tested the Ohmic evolution of our code by comparing with the analytic Ohmic eigenmodes, and observe excellent agreement. We also study the agreement of our code with the grid based code of [Gourgouliatos & Cumming \(2014\)](#), (data files provided by the authors), and observe excellent agreement. We have also carried out resolution studies of all simulations presented, and summarize the grid sizes for which each simulation had converged in Table B.1.



# Bibliography

- Alpar M. A., Langer S. A., Sauls J. A., 1984, *The Astrophysical Journal*, 282, 533
- Archibald R. F., Kaspi V. M., Tendulkar S. P., Scholz P., 2016, *The Astrophysical Journal Letters*, 829, L21
- Baade W., Zwicky F., 1934, *Physical Review*, 46, 76
- Backer D. C., Kulkarni S. R., Heiles C., Davis M. M., Goss W. M., 1982, *Nature*, 300, 615
- Baiko D. A., Yakovlev D. G., 1995, *Astronomy Letters*, 21, 702
- Baiko D. A., Yakovlev D. G., 1996, *Astronomy Letters*, 22, 708
- Baym G., Pethick C., 1975, *Annual Review of Nuclear and Particle Science*, 25, 27
- Baym G., Pethick C., Pines D., 1969, *Nature*, 224, 673
- Beloborodov A. M., 2009, *The Astrophysical Journal*, 703, 1044
- Beloborodov A. M., 2017, *The Astrophysical Journal Letters* (in press), 1702
- Beloborodov A. M., Levin Y., 2014, *The Astrophysical Journal*, 794, L24
- Beloborodov A. M., Li X., 2016, *The Astrophysical Journal*, 833, 261
- Bhattacharya D., Wijers R. A. M. J., Hartman J. W., Verbunt F., 1992, *Astronomy and Astrophysics*, 254, 198
- Borghese A., Rea N., Zelati F. C., Tiengo A., Turolla R., Zane S., 2017, *Monthly Notices of the Royal Astronomical Society*, 468, 2975

- Bowen M. K., Smith R., 2005, *Proceedings of the Royal Society of London A: Mathematical, Physical and Engineering Sciences*, 461, 1975
- Braithwaite J., Spruit H. C., 2006, *Astronomy & Astrophysics*, 450, 1097
- Bransgrove A., Levin Y., Beloborodov A., 2017, *Monthly Notices of the Royal Astronomical Society* (submitted for publication)
- Brown E. F., Bildsten L., 1998, *The Astrophysical Journal*, 496, 915
- Camilo F., Ransom S. M., Halpern J. P., Reynolds J., Helfand D. J., Zimmerman N., Sarkissian J., 2006, *Nature*, 442, 892
- Castillo F., Reisenegger A., Valdivia J. A., 2017, arXiv:1705.10020 [astro-ph]
- Chamel N., Haensel P., 2008, *Living Reviews in Relativity*, 11
- Chandrasekhar S., 1961, *Hydrodynamic and hydromagnetic stability. International Series of Monographs on Physics*, Oxford: Clarendon
- Choudhuri A. R., Konar S., 2002, *Monthly Notices of the Royal Astronomical Society*, 332, 933
- Comella J. M., Craft H. D., Lovelace R. V. E., Sutton J. M., Tyler G. L., 1969, *Nature*, 221, 453
- Cumming A., Zweibel E. G., Bildsten L., 2001, *The Astrophysical Journal*, 557, 958
- Cumming A., Arras P., Zweibel E., 2004, *The Astrophysical Journal*, 609, 999
- Dommes V. A., Gusakov M. E., 2017, *Monthly Notices of the Royal Astronomical Society: Letters* (accepted for publication)
- Duncan R. C., Thompson C., 1992, *The Astrophysical Journal Letters*, 392, L9
- Easson I., Pethick C. J., 1977, *Physical Review D*, 16, 275
- Elfritz J. G., Pons J. A., Rea N., Glampedakis K., Viganò D., 2016, *Monthly Notices of the Royal Astronomical Society*, 456, 4461
- Fahlman G. G., Gregory P. C., 1981, *Nature*, 293, 202
- Faucher-Giguere C.-A., Kaspi V. M., 2006, *The Astrophysical Journal*, 643, 332
- Ferrario L., Wickramasinghe D., 2006, *Monthly Notices of the Royal Astronomical Society*, 367, 1323

- Ferraro V. C. A., 1937, *Monthly Notices of the Royal Astronomical Society*, 97, 458
- Flowers E., Ruderman M. A., 1977, *The Astrophysical Journal*, 215, 302
- Gavriil F. P., Kaspi V. M., Woods P. M., 2002, *Nature*, 419, 142
- Glampedakis K., Andersson N., Samuelsson L., 2011, *Monthly Notices of the Royal Astronomical Society*, 410, 805
- Gnedin O. Y., Yakovlev D. G., Potekhin A. Y., 2001, *Monthly Notices of the Royal Astronomical Society*, 324, 725
- Goedbloed J. P., Keppens R., Poedts S., 2010, *Advanced Magnetohydrodynamics: With Applications to Laboratory and Astrophysical Plasmas*. Cambridge University Press, Cambridge
- Gold T., 1968, *Nature*, 218, 731
- Goldreich P., Reisenegger A., 1992, *The Astrophysical Journal*, 395, 250
- Gourgouliatos K. N., Cumming A., 2014, *Monthly Notices of the Royal Astronomical Society*, 438, 1618
- Gourgouliatos K. N., Wood T., Hollerbach R., 2016, *Proceedings of the National Academy of Sciences*, 113, 3944
- Graber V., Andersson N., Glampedakis K., Lander S. K., 2015, *Monthly Notices of the Royal Astronomical Society*, 453, 671
- Gügercinoğlu E., Alpar M. A., 2016, *Monthly Notices of the Royal Astronomical Society*, 462, 1453
- Gullón M., Miralles J. A., Viganò D., Pons J. A., 2014, *Monthly Notices of the Royal Astronomical Society*, 443, 1891
- Gullón M., Pons J. A., Miralles J. A., Viganò D., Rea N., Perna R., 2015, *Monthly Notices of the Royal Astronomical Society*, 454, 615
- Hessels J. W. T., Ransom S. M., Stairs I. H., Freire P. C. C., Kaspi V. M., Camilo F., 2006. p. 209.07
- Hewish A., Bell S. J., Pilkington J. D. H., Scott P. F., Collins R. A., 1968, *Nature*, 217, 709
- Ho W. C. G., Heinke C. O., 2009, *Nature*, 462, 71

- Hollerbach R., Rüdiger G., 2002, *Monthly Notices of the Royal Astronomical Society*, 337, 216
- Ibrahim A. I., et al., 2004, *The Astrophysical Journal Letters*, 609, L21
- Itoh N., Kohyama Y., 1993, *The Astrophysical Journal*, 404, 268
- Jones P. B., 1987, *Monthly Notices of the Royal Astronomical Society*, 228, 513
- Jones P. B., 1988, *Monthly Notices of the Royal Astronomical Society*, 233, 875
- Jones P. B., 1991, *Monthly Notices of the Royal Astronomical Society*, 253, 279
- Jones P. B., 2001, *Monthly Notices of the Royal Astronomical Society*, 321, 167
- Jones P. B., 2006, *Monthly Notices of the Royal Astronomical Society*, 365, 339
- Kaspi V. M., Beloborodov A., 2017, *Annual Review of Astronomy and Astrophysics* (in press)
- Kaspi V. M., Kramer M., 2016, *International Journal of Modern Physics D*
- Kaspi V. M., Gavriil F. P., Woods P. M., Jensen J. B., Roberts M. S. E., Chakrabarty D., 2003, *The Astrophysical Journal Letters*, 588, L93
- Konenkov D. Y., Geppert U., 2001, *Astronomy Letters*, 27, 163
- Kouveliotou C., et al., 1998, *Nature*, 393, 235
- Landau L., 1965, *Collected papers of L.D. Landau*, 1st ed. edn. Pergamon Press, Oxford ; New York
- Landau L., Lifshitz E., 1970, *Theory of Elasticity*. Pergamon Press
- Lasky P. D., Melatos A., 2013, *Physical Review D*, 88
- Levin Y., Lyutikov M., 2012, *Monthly Notices of the Royal Astronomical Society*, 427, 1574
- Li X., Levin Y., Beloborodov A. M., 2016a, arXiv:1606.04895 [astro-ph]
- Li X. H., Gao Z. F., Li X. D., Xu Y., Wang P., Wang N., Yuan J., 2016b, *International Journal of Modern Physics D*, 25, 1650002
- Lifshitz E. M., Pitaevskii L. P., 1980, *Statistical Physics: Theory of the Condensed State*. Butterworth-Heinemann, Oxford
- Manchester R. N., Hobbs G. B., Teoh A., Hobbs M., 2005, *The Astronomical Journal*, 129, 1993

- Marchant P., Reisenegger A., Valdivia J. A., Hoyos J. H., 2014, *The Astrophysical Journal*, 796, 94
- Mazets E. P., Golenetskij S. V., Guryan Y. A., 1979a, *Soviet Astronomy Letters*, 5, 641
- Mazets E. P., Golenetskii S. V., Il'inskii V. N., Aptekar' R. L., Guryan Y. A., 1979b, *Nature*, 282, 587
- Migdal A. B., 1959, *Nuclear Physics*, 13, 655
- Mukherjee S., Kembhavi A., 1997, *The Astrophysical Journal*, 489, 928
- Nozières P., Vinen W. F., 1966, *Philosophical Magazine*, 14, 667
- Ozel F., Freire P., 2016, *Annual Review of Astronomy and Astrophysics*, 54, 401
- Pacini F., 1968, *Nature*, 219, 145
- Page D., Prakash M., Lattimer J. M., Steiner A. W., 2011, *Physical Review Letters*, 106
- Parks R. D., 1969, *Superconductivity: Part 2 (In Two Parts)*. CRC Press
- Passamonti A., Akgün T., Pons J., Miralles J. A., 2017, arXiv:1704.02016 [astro-ph]
- Payne D. J. B., Melatos A., 2004, *Monthly Notices of the Royal Astronomical Society*, 351, 569
- Perna R., Pons J. A., 2011, *The Astrophysical Journal*, 727, L51
- Pons J. A., Geppert U., 2007, *Astronomy and Astrophysics*, 470, 303
- Pons J. A., Miralles J. A., Geppert U., 2009, *Astronomy and Astrophysics*, 496, 207
- Popov S. B., Pons J. A., Miralles J. A., Boldin P. A., Posselt B., 2010, *Monthly Notices of the Royal Astronomical Society*, 401, 2675
- Potekhin A. Y., Chabrier G., 2000, *Physical Review E*, 62, 8554
- Potekhin A. Y., Pons J. A., Page D., 2015, *Space Science Reviews*, 191, 239
- Rea N., et al., 2010, *Science*, 330, 944
- Rodríguez Castillo G. A., et al., 2016, *Mon.Not.Roy.Astron.Soc.*, 456, 4145
- Romani R. W., 1990, *Nature*, 347, 741
- Ruderman M. A., 1968, *Nature*, 218, 1128

- Ruderman M. A., Sutherland P. G., 1974, *The Astrophysical Journal*, 190, 137
- Ruderman M., Zhu T., Chen K., 1998, *The Astrophysical Journal*, 492, 267
- Shternin P. S., Yakovlev D. G., Heinke C. O., Ho W. C. G., Patnaude D. J., 2011, *Monthly Notices of the Royal Astronomical Society*, 412, L108
- Spitkovsky A., 2006, *The Astrophysical Journal*, 648, L51
- Srinivasan G., Bhattacharya D., Muslimov A. G., Tsygan A. J., 1990, *Current Science*, 59, 31
- Staelin D. H., Reifstein E. C., 1968, *Science*, 162, 1481
- Stairs I. H., Lyne A. G., Shemar S. L., 2000, *Nature*, 406, 484
- Suvorov A. G., Mastrano A., Geppert U., 2016, *Monthly Notices of the Royal Astronomical Society*, 459, 3407
- Tauris T. M., et al., 2014, *Proceedings of Science* (submitted for publication)
- Thompson C., Duncan R. C., 1993, *The Astrophysical Journal*, 408, 194
- Thompson C., Duncan R. C., 1996, *The Astrophysical Journal*, 473, 322
- Thompson C., Yang H., Ortiz N., 2017, *The Astrophysical Journal*, 841, 54
- Tiengo A., et al., 2013, *Nature*, 500, 312
- Turolla R., Zane S., Watts A. L., 2015, *Reports on Progress in Physics*, 78, 116901
- Viganò D., Rea N., Pons J. A., Perna R., Aguilera D. N., Miralles J. A., 2013, *Monthly Notices of the Royal Astronomical Society*, 434, 123
- Wood T. S., Hollerbach R., 2015, *Physical Review Letters*, 114, 191101
- Yakovlev D. G., Haensel P., Baym G., Pethick C. J., 2013, *Physics-Uspekhi*, 56, 289
- Yang W. H., Sturrock P. A., Antiochos S. K., 1986, *The Astrophysical Journal*, 309, 383